Université de Franche-Comté

École Doctorale Carnot-Pasteur
(ED CP n° 554)

PhD Thesis

Specialization: Astrophysics

presented by

RAJPUROHIT Arvind Singh

Low-mass stars as tracers of Milky Way populations : investigating the effect of metallicity in cool atmospheres

Directed by Céline Reylé and Co-directed by Mathias Schultheis

Jury :

Président :	France Allard
Rapporteurs :	France, Allard
	Rob Jeffries
Examinateurs :	Xavier Bonfils
	Alejandra Recio-Blanco
	Céline Reylé
	Mathias Schultheis

Acknowledgements

First and foremost, I would like to thank to my PhD supervisor Dr. Céline Reylé and co-supervisor Dr. Mathias Schultheis, for supporting me during these past three years. Céline is someone you will never forget once you meet her. She is the funniest, cool and calm advisor. I hope that I could be as lively, enthusiastic, and energetic as Céline. It has been an honor to be her first Ph.D student. Both Céline and Mathias has taught me, consciously and unconsciously, how good astronomy and astrophysics is done. I appreciate all their contributions of time, ideas, and funding to make my Ph.D experience productive and stimulating. The joy and enthusiasm both Céline and Mathias has for their research was contagious and motivational for me, even during tough times in the Ph.D pursuit. I am also thankful for the excellent example Céline has provided as a successful woman astrophysicist.

Besides my advisors I would like to thank prof. France Allard. This thesis would not have been possible without the advice and encouragement of Prof. Allard. She taught me how to be a scientist, from proposals to observations to publications. She was always encouraging, understanding, and, perhaps most importantly, available for discussions. She is my primary resource for getting my science questions answered. I would also like to thank Dr. John P Killingbeck for reading this thesis and helping me in english corrections.

A good support staff is important to surviving and staying sane during PhD. I would like to thank all the members of the Observatoire de Besancon in particular Annie, F. Gazelle, Kevin, Sékou, Martin, Edith, and Andre which has contributed immensely to my personal and professional time at Besancon. The group has been a source of friendships as well as good advice. In addition, I would like to thank Derek Homeier, ENS Lyon, who provided me the model atmosphere as a first priority. I am also grateful to Prof. Ch. Leinert for providing me the data for LHS1070 triple system. Finally, I must thank the person who meant the most to me these past three years. Ashok Verma's friendship, love, and support have meant so much to me. I hope that I can be as helpful as he finishes his own dissertation.

Lastly, I would like to thank my family for all their love and encouragement. For my parents who raised me with a love of science and supported me in all my pursuits. I would also like to thank my sisters Kamlesh and Sangeeta for their love and support have made everything possible.

Abstract

Very Low-Mass stars (M dwarfs) are an important source of information for probing the low mass end of the main sequence, down to the hydrogen burning limit. They are the dominant stellar component of the Galaxy and make up the majority of baryonic matter in the Galaxy. Moreover, an increasing number of M dwarfs are now known to host exoplanets, including super-Earth exoplanets. The determination of accurate fundamental parameters for M dwarfs has therefore relevant implications for both stellar and Galactic astronomy as well as planetology. Despite their large number in the Galaxy, M dwarfs remain elusive objects and the modelling of their photosphere has long remained a challenge (molecular opacities, dust cloud formation). The description of these stars therefore need a strong empirical basis, or validation. In particular, the effect of metallicity on the physics of cool atmospheres are still poorly known, even for early-type M-dwarfs.

The goal of this thesis is to determine the fundamental stellar parameters of these low-mass dwarfs (M dwarfs) and to test recent model atmospheres. In particular this works aims to validate the BT-Settl model atmospheres, to understand the onset of dust formation in cool stellar atmospheres and to update the current knowledge about the relationship between spectral type and effective temperature ($T_{\rm eff}$) of M dwarfs.

The first part of this study sets out to improve the understanding of onset of the dust formation in cool stellar atmospheres. We perform a χ^2 minimization by comparing well calibrated optical and infrared (IR) spectra with recent cool star model synthetic spectra, leading to the determination of the physical stellar parameters $T_{\rm eff}$, radius and log g for each of the component of the triple sysytem LHS 1070 (Rajpurohit et al. 2012b,a). This study is then extended by validating BT-Settl model atmospheres, updating the M-dwarf $T_{\rm eff}$ - spectral type relation, and finding the atmospheric parameters of a sample of M-dwarfs. We also present the relationship between effective temperature, spectral type and colours for the M-dwarfs (Rajpurohit et al. 2013).

The second part of this study deals with the analysis of high resolution spectroscopy for M subdwarfs. This study shows that the observational and modelling efforts are required to fully understand the physics in the cool subdwarf atmosphere and to investigate the effect of metallicity in particular for the lower metallicity. This study presents the UVES/VLT high resolution spectra of 21 M subdwarfs. Our atlas covers the optical region from 6400 Å up to the near infrared at 8900 Å. We show spectral details of cool atmospheres at very high resolution (R$\backsim$ 40 000) and compare the observed with synthetic spectra computed from the recent BT-Settl atmosphere models, to disentangle their stellar parameters and to determine their precise metallicity.

This work should initiate further research: in particular we want to verify that the near-IR spectral energy distribution will yield results that are consistent with the optical. The exten-

sion of this study to the near-IR will generate the first complete atlas of overall M-dwarfs and subdwarfs spectra for which parameters ($T_{\rm eff}$, log g and Fe/H) have been determined from this work.

Contents

List of Figures

List of Tables

Chapter 1

Motivation

M dwarfs are an important part of the low mass stars, which are the most numerous and dominant stellar component of the Galaxy and make up the majority of baryonic matter in the Galaxy (Gould et al. 1996; Mera et al. 1996; Henry 1998). These low-mass objects are found to dominate the solar neighborhood, as well as more distant field samples and open clusters, with the peak in their luminosity function occurring around $M_V \backsim 12$ and $M_K \backsim 7$ (e.g., Dahn et al. 1986; Luyten 1968; Leggett & Hawkins 1988). Their main-sequence lifetimes are much greater than the current estimated age of the Universe (Laughlin et al. 1997). Therefore, the observation and the study of M dwarfs can be used to trace the structure and evolution of the Milky Way. Our understanding of the Galaxy relies upon the description of the stars composing this faint component, including the determination of their chemical composition. Indeed M-dwarfs have been employed in several Galactic studies, dealing with Galactic disk kinematics (Hawley et al. 1996; Gizis et al. 2002; Lépine et al. 2003a; Bochanski et al. 2005, 2007b, 2010), the structure and the component of the Galaxy (Reid & Gizis 1997; Kerber et al. 2001; Woolf & West 2012) and the initial stellar mass function (Covey et al. 2008; Bochanski et al. 2010). Moreover, an increasing number of M dwarfs are now known to host exoplanets, including super-Earth exoplanets (Butler et al. 2004; Bonfils et al. 2012). There are some fundamental and preliminary studies which have been done on M dwarfs, including classifying their spectral type (Kirkpatrick et al. 1991; Reid et al. 1995; Kirkpatrick et al. 1999; Martín et al. 1999; Cruz & Reid 2002), measuring radial velocity (Bochanski et al. 2007a), estimating metallicity (Gizis 1997; Lépine et al. 2003a; Woolf & Wallerstein 2006; Lépine et al. 2007; Bean et al. 2006a; Rojas-Ayala et al. 2010; Bonfils et al. 2005) and studying magnetic activity (Reid et al. 1995; Hawley et al. 1996; Gizis 1997; West et al. 2004, 2011). The low mass M dwarfs display a wide range of internal and atmospheric stellar characteristics, including the onset of complete convection in the stellar interior, and the formation of dust, with the subsequent depletion of metals onto dust grains in the stellar atmosphere(Allard et al. 2012a). As progressively cooler stellar and substellar objects are being discovered by various photometric and spectroscopic surveys, the presence of first molecules and then condensed particulates greatly complicates the understanding of their physical properties. In M dwarfs later than M6 the outermost temperatures fall below the condensation temperatures of silicate grains, which leads to the formation of dust clouds (see e.g.,

Tsuji et al. 1996b,a; Allard et al. 1997; Ruiz 1997; Allard et al. 1998). The presence of a wide variety of molecular absorber and numerous condensates greatly complicates the accurate modeling of these cool stellar atmospheres.

Despite the large number of very low mass stars in the Galaxy, little is known about them, because it is difficult (i) to get a homogeneous sample with respect to the age and metallicity, owing to their intrinsic faintness, (ii) to disentangle the parameter space ($T_{\rm eff}$, $\log g$ and metallicity). Indeed, a number of studies have shown that when using broad band photometry or low resolution spectra a change in temperature or gravity can compensate for a change in metallicity. Thus high and low-resolution spectroscopic observations of M dwarfs stars are crucial for understanding stellar astrophysics for stars at the bottom end of the main sequence. They are also very important to study the process of planet formation across the H-R diagram as M dwarfs are the most favorable stars for planet detection. An atlas of high-resolution spectra both in the optical and in the near-IR range for very low mass stars will also be critical for the modeling of chemical abundances and for probing the physical processes that occur in the complex atmospheres of M dwarfs.

In order to identify and quantify the low mass dwarf stars, transition objects and brown dwarfs we need to determine accurately their stellar parameters such as mass, luminosity, surface gravity, radius, effective temperature and atmospheric chemical composition. At present the physical properties of these low mass M dwarfs are not particularly well understood. For example the effective temperature scale of the M dwarfs is controversial, yet it is crucial for a proper understanding of their locus in the Hertzsprung-Russel (H-R) diagram. In particular, the temperature scale is needed to identify the long-sought "brown-dwarfs". The controversy has arisen because the complex spectra are difficult to model reliably. The construction of an effective temperature scale for the M dwarfs has been attempted in recent years by comparing the spectra of these objects with synthetic spectra generated by atmospheric models. It is found that the models fit the observed spectral energy distribution (SEDs) and colours fairly well overall, and an effective temperature sequence is indeed derivable from the data fits (Rajpurohit et al. 2012b, 2013). However, as $T_{\rm eff}$ decreases from early to late spectral types, some molecular bands that comprise most of the low-resolution spectral features of these cool objects first increase and then decrease in strength owing to dust formation (both through depletion from the gas phase and from green house effects). The molecular line lists used in the models are not fully satisfactory, which could effect the predicted temperature scale. The measurement of the chemical compositions of M dwarfs is still limited, despite the ease of obtaining very high quality spectra for them. Today, the factor limiting the determination of accurate chemical compositions for M dwarfs is the lack of a technique reliable enough to interpret the complex spectra of these stars. Modern techniques of analysis applied to high resolution and high signal-to-noise ratio spectra of solar-type stars consistently yield chemical abundances with internal precisions of 10%. The application of these methods to M dwarfs is complicated by the effects of significant molecule formation and the resulting opacity produced in the photospheres of these stars.

Over the last decade, stellar models for very low mass (VLM) stars have made great progress. Indeed, the PHOENIX model atmospheres synthetic energy distribution improved greatly on that from earlier studies (Allard & Hauschildt 1995a; Hauschildt et al. 1999), as do more recent models by Allard et al. (2001, 2011, 2012a); Witte et al. (2011); Rajpurohit et al. (2012b). However, they still have to use some incomplete or approximate input physical parameters such as uncertain collisional damping constants for some atomic lines, molecular bands and for missing line list of opacity source. The comparison between M-dwarf spectra and atmospheric model spectra will bring constraints on the physics of these cool objects. The scientific aim of this study is to investigate the effects of the physical parameters (effective temperature, mass, luminosity, gravity, metallicity, radius) on the spectra and on the behavior of the molecular structures. In particular, chemical abundance is a poorly known parameter, yet is essential in order to understand the physics at different ages of the Galaxy. One approach to studying the physics at the low end of the main sequence is to compare observed spectra with synthetic spectra from various authors and modeling techniques. The appropriate physical parameters can be determined by using spectral synthesis, including χ^2 minimization and other "best fit" criteria.

This thesis describes the results of several projects aimed at characterizing the properties of the very low mass stars, with particular emphasis on M dwarfs and subdwarfs. The layout of this thesis is as follows:

In Chapter 2, we give a general introduction to M dwarfs and subdwarfs. This chapter makes it clear why the study of very low mass stars is important. In chapter 3, we describe in detail the model atmospheres used for the current study. In chapter 4, we confront different model atmospheres described in chapter 3 by directly comparing their predictions with observation on the triple system LHS1070 (Rajpurohit et al. 2012b). In chapter 5, we estimate the effective temperature scale of M dwarfs by comparing a sample of M dwarf spectra (at both medium and low resolution) and broad band photometry with the spectra computed by the recent BT-Settl model atmosphere. We compare the new $T_{\rm eff}$ scale with those which we have found in the literature and thus establish a revised $T_{\rm eff}$ scale for M dwarfs (Rajpurohit et al. 2013). In Chapter 6, we compare the high resolution optical spectra of subdwarfs with the predictions of the BT-Settl model atmosphere. We estimate the $T_{\rm eff}$ for M subdwarfs using the results of high resolution optical spectroscopy. Because of the high resolution of our spectra, we can perform a detailed comparison of lines profile of individual elements such as Fe I, Ca II, Ti I, Na I, K I and are able to determine accurate metallicities for the entire M subdwarf spectral sequence, which can later be linked to their kinematical properties. Chapter 7 gives the conclusion of this study, together with future prospectives.

Chapter 2

The Basics Properties of M-dwarfs

2.1 Introduction to M-dwarfs

Within less than two decades the study of low-mass stars and brown dwarfs has bloomed into one of the most active fields in astronomy. The low-mass end of the main sequence from M, L, T and Y dwarfs includes objects spanning several orders of magnitude in temperature, from 4000 K down to room temperature, and nearly fills the entire temperature gap between the coolest stars and our Solar System's giant planets. Stars known as red-dwarfs and red subdwarfs are main sequence stars, a classification typically meant to include all main sequence objects of spectral subtype K5 to M9. Their masses range from $0.08M_{\odot} \leq M_{\odot} \leq 0.8M_{\odot}$, based on their estimated metallicity (Chabrier et al. 2000). Despite their intrinsic faintness, M-dwarfs constitute a large fraction of the detectable baryonic matter in the Galaxy. They are the dominant stellar component in the Galaxy, comprising $\backsim$ 70% of all stars (Chabrier 2003) and nearly half the stellar mass of the Galaxy which make the lower end of the Hertzsprung-Russel diagram very important. These stars are found in any population, from young metal-rich M-dwarfs in open clusters (Reid 1993; Leggett et al. 1994) to the several billion years old metal-poor dwarfs in the galactic halo (Green & Margon 1994) as well as in globular clusters (Cool et al. 1996; Renzini et al. 1996). Such low mass stars are an important probe for our Galaxy; as they carry fundamental information regarding stellar physics and about the structure, formation and dynamics of the Galaxy. The M-dwarfs span very long life time in the universe. Some have lifetime much greater than the estimated age of the universe, which makes them an important fossil record of Galactic history of great value in probing the structure and evolution of the Milky Way.

Recent improvements in kinematic modelling and magnetic activity analysis have provided enhanced statistical age estimates for populations of low-mass dwarfs (West et al. 2006). When coupled with information about metallicity, these ages can provide valuable insight into the history of the chemical evolution of the Milky Way. Their huge number in the Galaxy makes M-dwarfs very important in the study of various process such as the formation and evolution

of stars. Because of their ubiquity, cool dwarfs may represent the largest population of stars which have orbiting planets, especially low-mass planets in their respective habitable zones, which with relatively tight orbits for a cool dwarf system. In addition, the fact that the existence of brown dwarfs or planets has been discovered and confirmed around M-dwarfs (Butler et al. 2004; Bonfils et al. 2012) plays an important role in understanding the formation of brown dwarfs and planets. M-dwarfs are also very important to derive various quantities such as Initial mass function (IMF), and the present day mass function. These frequently used functions are derived by using the luminosity. However, the historic deficiency of data for M-dwarfs was primarily due to their intrinsic faintness, a consequence of their low mass. The situation has been radically altered in the last decade, as deep surveys covering large areas of the sky have been carried out. Projects such as the Solan Digital Sky surveys (SDSS, York et al. 2000), the Two-Micron All Sky Surveys (2MASS, Skrutskie et al. 2006) and the Deep Near-Infrared Survey of the Southern Sky (DENIS, Epchtein et al. 1999) can trace their root back to photographic surveys. An important by-product of recent transit surveys has been the discovery of many eclipsing binaries with M-dwarf components (e.g., Coughlin et al. 2011; Harrison et al. 2012; Birkby et al. 2012). These systems have traditionally been the most favourable for determining the basic properties of late-type stars, including their masses, radius, temperature, and luminosity. Unfortunately, most newly discovered systems tend to be faint, so the problem for accurate determinations continues to be that of carrying out accurate spectroscopy.

In general, it is necessary to obtain the spectra of low mass M-dwarf candidates selected by using photometry or a study of proper motions in order to confirm their spectral types; this limits the temperature and mass of a suitable candidate. Low resolution spectra are normally preferred for the initial followup of candidates, since they are adequate for the measurement of broad molecular absorption bands of late-type M-dwarfs, while also providing the highest signal-to-noise ratios. Most of the well observed M-dwarfs are relatively nearby and their observed trigonometric parallaxes are therefore quite reliable, so that accurate absolute luminosities are known. Methods have been derived to find their mass, their location and density in the Galaxy, their age (involving effective temperature), bolometric corrections, absolute visual magnitude and several colour indices for them have been established. However, the measurement of the chemical compositions of M-dwarfs is still limited, as it require lot of telescope time to obtain very high quality spectra for them. The current factor limiting the determination of accurate chemical compositions for M-dwarfs is the lack of a accurate atmosphere models reliable enough to interpret the complex spectra of these stars.

2.2 A Survey of the Properties of M-dwarfs

Determining the fundamental properties of M-dwarfs, is a challenge from both observational and theoretical perspectives. Empirical values for M-dwarfs masses, luminosities, temperatures and radii can be extracted by studying the orbits of M-dwarf binaries (Leinert et al. 2000). How-

ever, the intrinsic faintness of these systems makes their observation challenging and analysis of known binaries reveals systematic variations in inferred temperatures or radii. Theoretical constraints on M-dwarf atmospheric parameters have similarly been difficult to obtain. Accurate modelling of the deep convective zones in M-dwarf interiors and of the formation of the molecules and grains that dominate M dwarf atmospheres (Tsuji et al. 1996b; Allard et al. 2000) requires significant computational resources as well as an extensive database of oscillator strengths and opacities obtained from laboratory experiments.

2.2.1 Physical properties

The theory of the evolution of low mass stars is mainly based on a detailed study of the variation with time of bolometric luminosity, effective temperature, radius and angular momentum, for a given stellar mass. Theoretical models of stellar interiors and atmospheres have made predictions for the temporal evolution of the first three parameters, while other structure (e.g., winds, disk) may produce loss of angular momentum. The thin radiative skin above the convective region in an M-dwarf determines the surface boundary conditions for the entire temperature structure of the fully convective photosphere and interior. The temperature of M-dwarfs ranges from 4000 to 2300 K and the surface gravity, ranging from $\backsim$ 4.5 - 5.5, allows the formation of various molecules. At these low temperature the structure of M-dwarfs is affected by atomic and molecular opacity and convection. The atmosphere thus become more sensitive to the strong opacity due to molecules such as TiO, H_2O, so that this molecular opacity eventually becomes the main source of absorption. With their complex description of atmospheric physics and chemistry the observations have now reached a high level of sophistication, while the theoretical model side has fallen behind. In particular, precise observational calibrations of the basics physical properties of M-dwarfs, such as their mass, age, radius, luminosity or surface gravity is still missing. Unfortunately the degeneracy in the age-temperature relation for M-dwarfs makes it difficult to make an unambiguous determination of their physical properties. Direct size measurements of low-mass stars represent vital tests of theoretical models of stellar evolution, structure, and atmospheres. As seen in the results of Berger (2006), notable disagreements exist between interferometrically determined radii and those calculated in low-mass stellar models such as those of Chabrier & Baraffe (1997) and Siess & Livio (1997) in the sense that interferometrically obtained values for the stellar diameters are systematically larger by more than 10% than those predicted from models. Developments on both the observational and theoretical fronts are thus essential in order to obtain meaningful and important estimates of the physical properties of M-dwarfs (see the review from Allard et al. 1997, 2012a; Chabrier et al. 2000).

2.2.2 Photometric Properties

SDSS, 2MASS and DENIS have had great success in discovering M-dwarfs. If the images are deep enough and an appropriate combination of filters is used, it is actually easier to iden-

tify cool M-dwarfs than many other classes of astronomical objects, because of the distinctive nature of their spectral energy distribution (SED), which is due to the presence of strong molecular absorption bands. The colours of M-dwarfs provide insight into the processes operating in their atmospheres. Because of their intrinsic faintness, moderate- to high-resolution spectroscopy may not be performed on all of the cool M-dwarfs which have been discovered by these surveys. Thus, analyses of cool M dwarf colours could be essential in providing information on their physical properties. As is well known, the chemical composition of the stellar photosphere (or its metallicity) affects the stellar energy distribution. Systematic trends have also been identified in colour-colour diagrams using the known correlation between kinematic population and metallicity. Alternatively, the location of a star in a colour-colour diagram can be used as a metallicity indicator: the metal-poor subdwarfs stars are usually sub-luminous in such a diagram (fig. 2.1).

The reason for this behaviour is that the decreased metallicity leads to a decreased atmospheric opacity. This effect means that a star of fixed mass 'moves' in the H-R diagram to a position of higher $T_{\rm eff}$ and higher luminosity. For very cool M-dwarfs, broadband photometry at near-IR wavelengths is primarily detecting the strong molecular bands of H_2O, CH_4, CO, and H_2. Broadband photometry at optical wavelengths ($\lambda \leq 1\mu$m) measures very different spectrophotometric features. Despite the faintness of cool dwarfs, the multicolour photometry of M-dwarfs has proven to be sufficient for the determination of the normal colours, bolometric corrections, and $T_{\rm eff}$ for them. Optical and near infrared photometry can be useful as a diagnostic tool for finding the potential candidate of very low mass stars, but it is not possible to disentangle the parameters when addressing different populations of very low mass stars..

2.2.3 Spectroscopic properties

The H-R diagram is the most important map in stellar astronomy. It provides a relatively straightforward method for separating different stellar luminosity classes. The theoretical study of stars is usually divided into separate parts dealing with stellar interiors and stellar atmospheres. Although they are interesting objects in their own right, M-dwarfs have a wider potential which at present is largely unrealized, because investigation of their properties is largely hampered by the complex lines and bands of diatomic and triatomic molecules which appear in their observed spectra. The effects of temperature and of reduced gravity modify the chemical and physical properties of their atmospheric layers, producing the peculiar spectroscopic features that have been identified in the optical spectra of M-dwarfs. In an M-dwarf atmosphere most of the hydrogen is locked into H_2 and most of the carbon into CO. With decreasing temperature, M dwarf spectra show an increase in abundances of diatomic and triatomic molecules which contributes to the optical and the near-infrared spectra (such as SiH, CaH, CaOH, TiO, VO, CrH, FeH, OH, H_2O, CO). The TiO bands in the optical region and the H_2O bands in the infrared have complex and extensive band structures, leaving no window for the true continuum and creating a pseudo-continuum which allows observation of only the strongest (often resonance) atomic lines such as those from Ca II, Na I and K I (Allard 1990a; Allard & Hauschildt 1995a).

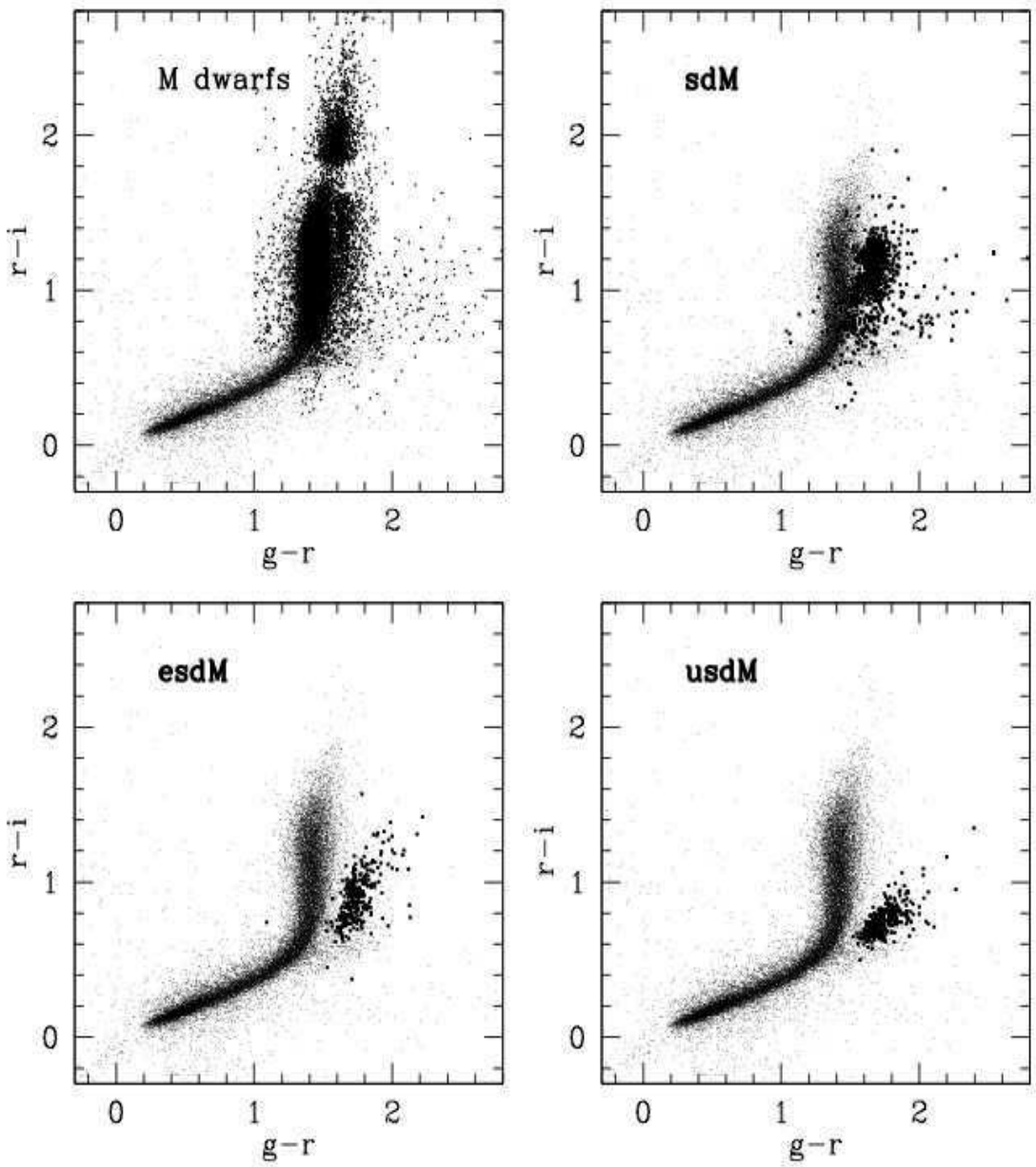

Figure 2.1 – Loci of cool stars classified as M dwarfs, subdwarfs (sdM), extreme subdwarfs (esdM) and ultrasubdwarfs (usdM) in the SDSS g-r/r-i colour-colour space by Lépine (2009).

The spectral transition from low-mass M dwarfs to the latest type brown dwarfs is noteworthy for demonstrating how a considerable transformation of the spectral features can be due to a small change in the effective temperature. The spectral transition is characterized by i) the condensation onto seeds of strong opacity-causing molecules such as CaH, TiO and VO, which govern the entire visual to near-infrared part (0.4-1.2 μm) of the spectral energy distribution (hereafter SED); ii) a 'veiling' due to Rayleigh and Mie scattering from sub-micron to micron-sized aerosols; iii) a weakening of the infrared water vapour bands owing to oxygen-rich grain

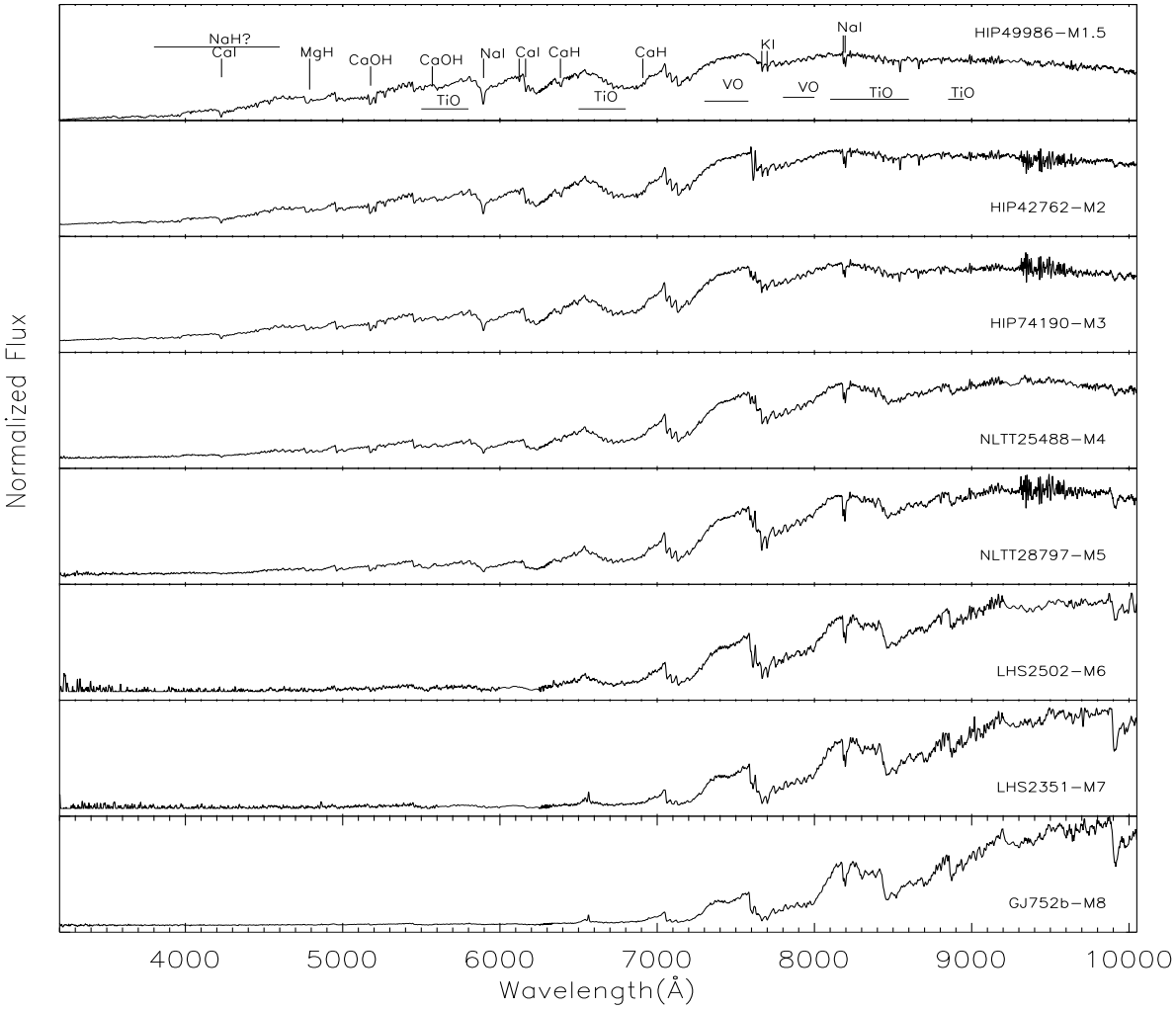

Figure 2.2 – The optical to red SED of M-dwarfs from M0 to M8, observed at Siding Spring Observatory (SSO) at a spectral resolution of 1.4 Å. The atomic and molecular features are clearly visible. The chromospheric emission fills the Na I D transition for the latest-type M-dwarfs displayed here, while M8 has a flatter spectrum because of dust scattering.

condensation and to the greenhouse (or blanketing effect) caused by silicate dust; iv) methane and ammonia band formation in T and Y dwarfs; v) water vapour condensation in Y dwarfs ($T_{\rm eff} \leq 500$ K). Condensation begins to occur in M dwarfs with $T_{\rm eff} \leq 3000$ K. In T dwarfs and brown dwarfs the visual to red part of the SED is dominated by the wings of the Na I D and 0.77 μm K I alkali doublets, which form out to as much as 2000 Å from the line centre (Allard et al. 2007a). The SED of those dwarfs is therefore dominated by molecular opacities and resonance atomic transitions under pressure ($\backsim$3 bars) broadening conditions, leaving no window for the continuum (Allard 1990a; Allard et al. 1997, 2012a).

Despite their extreme faintness ($10^{-2}-10^{-5}L_{\odot}$) in V bandpass, M-dwarfs yield spectroscopic features which can still provide us with information about basic atmospheric properties such as luminosity, metallicity and temperature. For example i) The CaOH bands around 0.54-0.556 μm in dwarfs later than M3 are a very good temperature indicator and a good discriminant between M-dwarfs and backgrounds red giant stars (Gizis 1997; Reid & Gizis 2005; Martin et al. 1996). ii) An atomic spectral feature such as that of Ca I (6162 Å) can possibly be used to distinguish subdwarfs from dwarfs. iii) Hydride bands such as those of CaH at 6380 Å and 6880 Å decreases in strength with decreasing temperature, whereas the NaI doublet at 8183 Å and 8195 Å is relatively strong for earlier type M-dwarfs but relatively weaker for later type. iv) The KI doublet at 7665 Å and 7699 Å is very strong and is useful for making gravity determination. v) The saturation of the TiO band strength in M-dwarfs later than M5 and the introduction of the VO to TiO band strength index is now used to classify M-dwarfs and substellar candidates later than M5 (Henry et al. 1994; Kirkpatrick et al. 1995; Martin et al. 1996). Figure 2.2 shows the optical to red SED of M-dwarfs from M0 to M9.5, observed at Siding Spring Observatory (SSO) at a spectral resolution of 1.4 Å (Rajpurohit et al. 2013). Molecular band spectra are much more complex than atomic spectra and dominate the spectral regions in which they are located. TiO has an especially distributed and complex spectrum and it dominates M dwarf spectra in the spectral regions traditionally used to determine the chemical compositions of solar-type stars. This can be seen in fig. 2.2, where the M dwarf spectra show a significant deviation, primarily due to TiO absorption, from the predominantly smooth continuum spectra of earlier type stars.

Figures 2.3 to 2.6 shows the IR spectra of M-dwarfs (Cushing et al. 2005). It can be seen that the dominant near infrared features are due to photospheric absorption by water vapour, FeH, neutral metals, carbon monoxide, and OH. The absorption lines of neutral metals, as well as the bands of water and CO, become stronger with decreasing temperature. In the optical region, metal-poor stars show strong features relative to the strength of the molecular TiO bands. However, in the infrared regime the dominant molecular features are due to water, and this single metal species will not show the same level of decrease as the double metal TiO. The atomic spectral lines such as those of Fe I, Ca I, Na I, K I, Si I, Mg I, Al II, along with some hydride bands such as those of FeH, can be seen in the J-band spectra with equivalent widths of 2-2.5 Å and 1.52 Å, respectively; but most of these features weaken in the spectra of mid-to late-type M-dwarfs. The H band is the most difficult wavelength range in which to identify features in the spectra of early M-dwarfs, because it contains many relatively weak absorption features which defy definite identification. Only a few doublets and triplets of Mg, Si, Al, and K are clearly evident, with the possible exception of OH (1.689 μm). H_2O bands define the shape of the J and H band peaks. Water absorption is most obvious in the J-band at 1.33 μm and strengthens through the later M-dwarf types. The K-band spectra of early M-dwarfs also exhibit atomic features due to Ca, Mg, Al, Si, Na, Ti, and Fe and also shows strong CO bands. These spectral features all weaken with decreasing temperature. H_2O absorption bands also appear on either side of the K-band at a spectral type of $\backsim$ M4 and strengthen through the M, L, and T sequences.

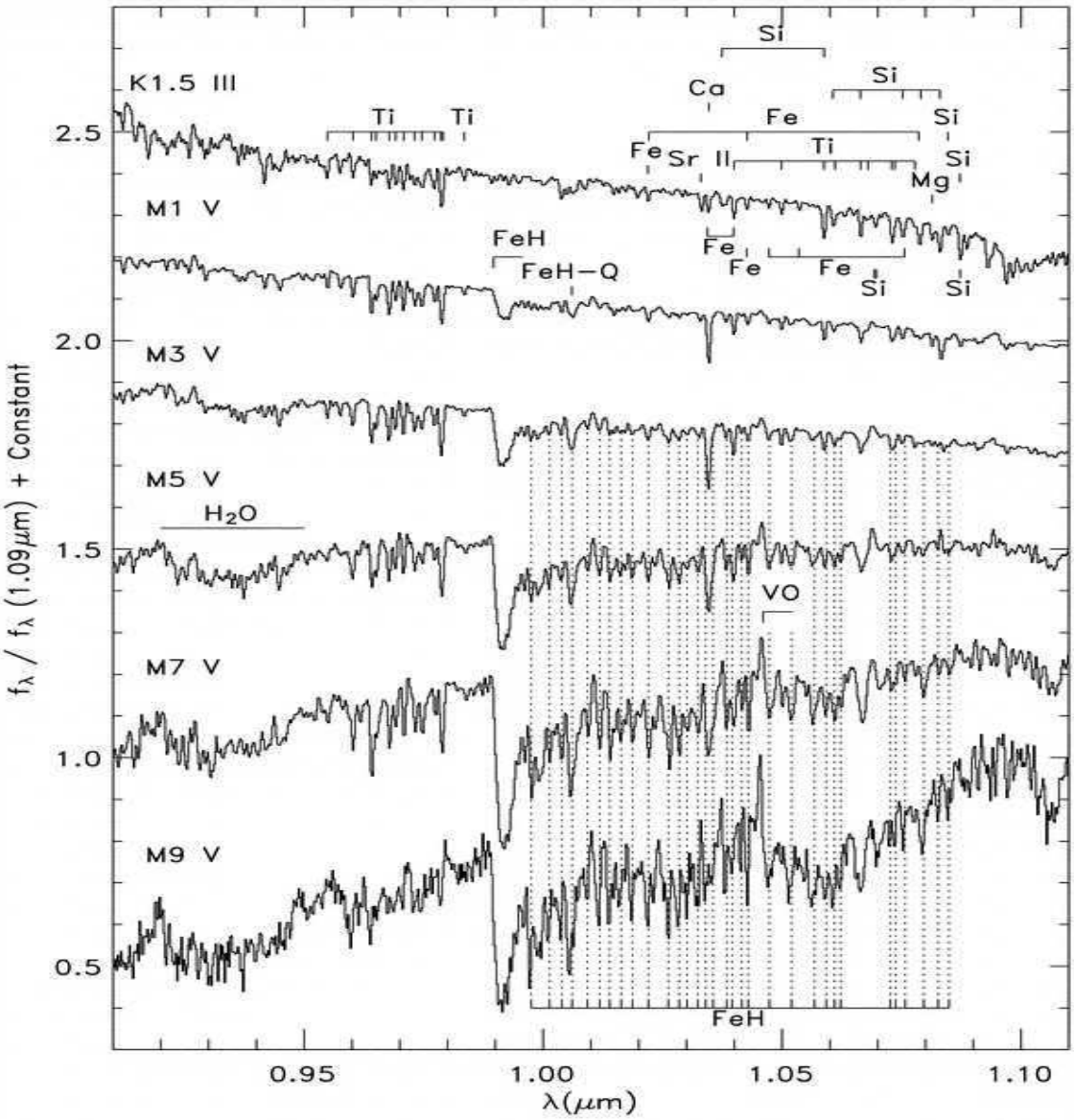

Figure 2.3 – z-band spectra sequence of M-dwarfs (Cushing et al. 2005). The most prominent molecular and atomic features are indicated.

2.3 Stellar Parameters of M-dwarfs

2.3.1 Effective Temperature

An effective temperature measurement for a low-mass star or brown dwarf is important to determine flux or luminosity which then can be used to confirm whether a given object is hot or cool. The empirical temperature scale for cool stars is generally well established and temperatures are now known with reasonable precision for stars covering the range of spectral type from A to M. The M dwarf temperature scale has been a subject of some interest for several decades now,

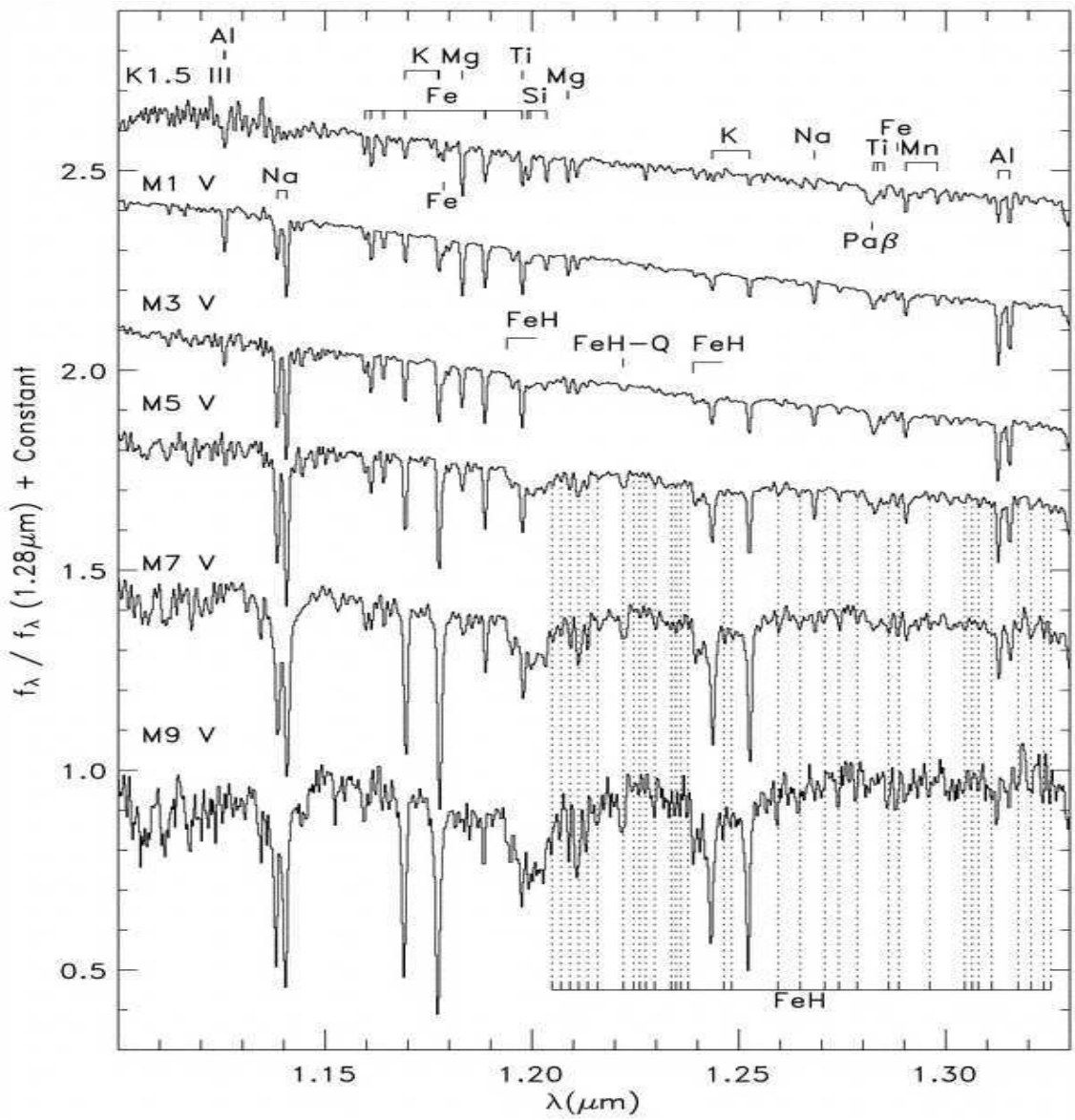

Figure 2.4 – J-band spectra sequence of M-dwarfs (Cushing et al. 2005). The most prominent molecular and atomic features are indicated.

especially since the development of detectors with suitable sensitivity in the infrared spectral region has made it possible to obtain the relevant observational data. Empirical temperatures for metal-deficient and metal rich stars had been virtually non-existent, but recently the infra-red flux method (IRFM) has been applied by Casagrande et al. (2008) to a sample of M-dwarfs, providing approximate $T_{\rm eff}$ values for them. Empirical measurement of M dwarf temperature can be obtained by the information extracted from the orbits of M dwarf binaries. As shown by the results of Irwin et al. (2011) and Kraus et al. (2011), radii and temperatures of low-mass stars obtained from eclipsing binaries are systematically larger and cooler (respectively) for given mass. This is mainly due to the intrinsic faintness of these low-luminosity systems, and the analyses of known binaries reveal systematic offsets in inferred temperatures and radii

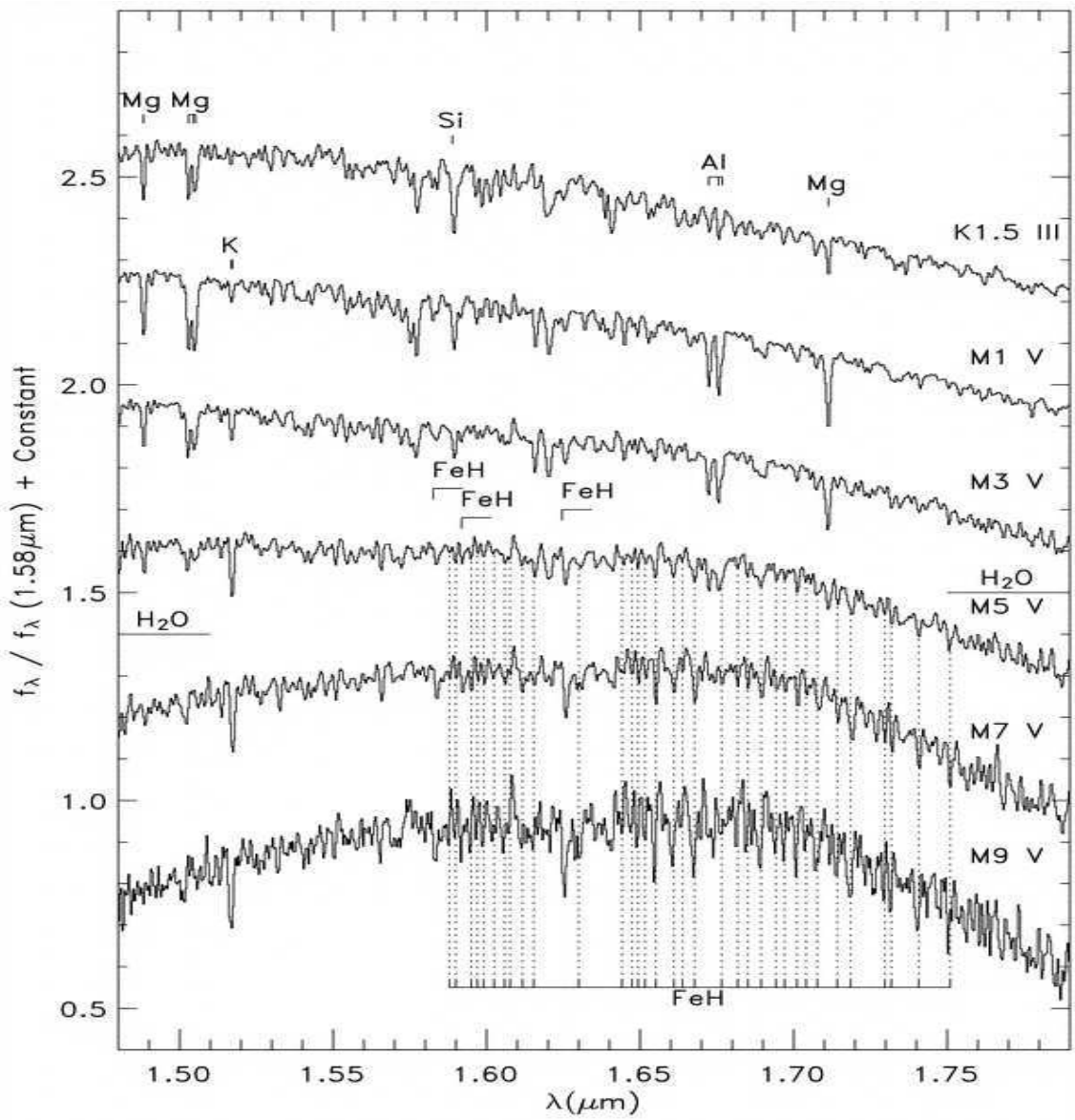

Figure 2.5 – H-band spectra sequence of M-dwarfs (Cushing et al. 2005). The most prominent molecular and atomic features are indicated.

that correlate with both orbital period and magnetic activity. Strong magnetic field can prevent convection, thus giving larger radii for a given $T_{\rm eff}$ or lower $T_{\rm eff}$ for a given radius (Casagrande et al. 2008). The presence of numerous large spots at the surface can thus lower the $T_{\rm eff}$ of the star.

Significant advances have also been made in atmospheric modelling for cool stars, by incorporating improved metal-line and molecular line source of opacity in the models. The effective temperature of cool M-dwarfs can be estimated from their spectral type and from the fitting of observed spectral lines to the synthetic spectra predicted using a model atmosphere. Synthetic photometry generated using the model atmosphere show good agreement with the empirical

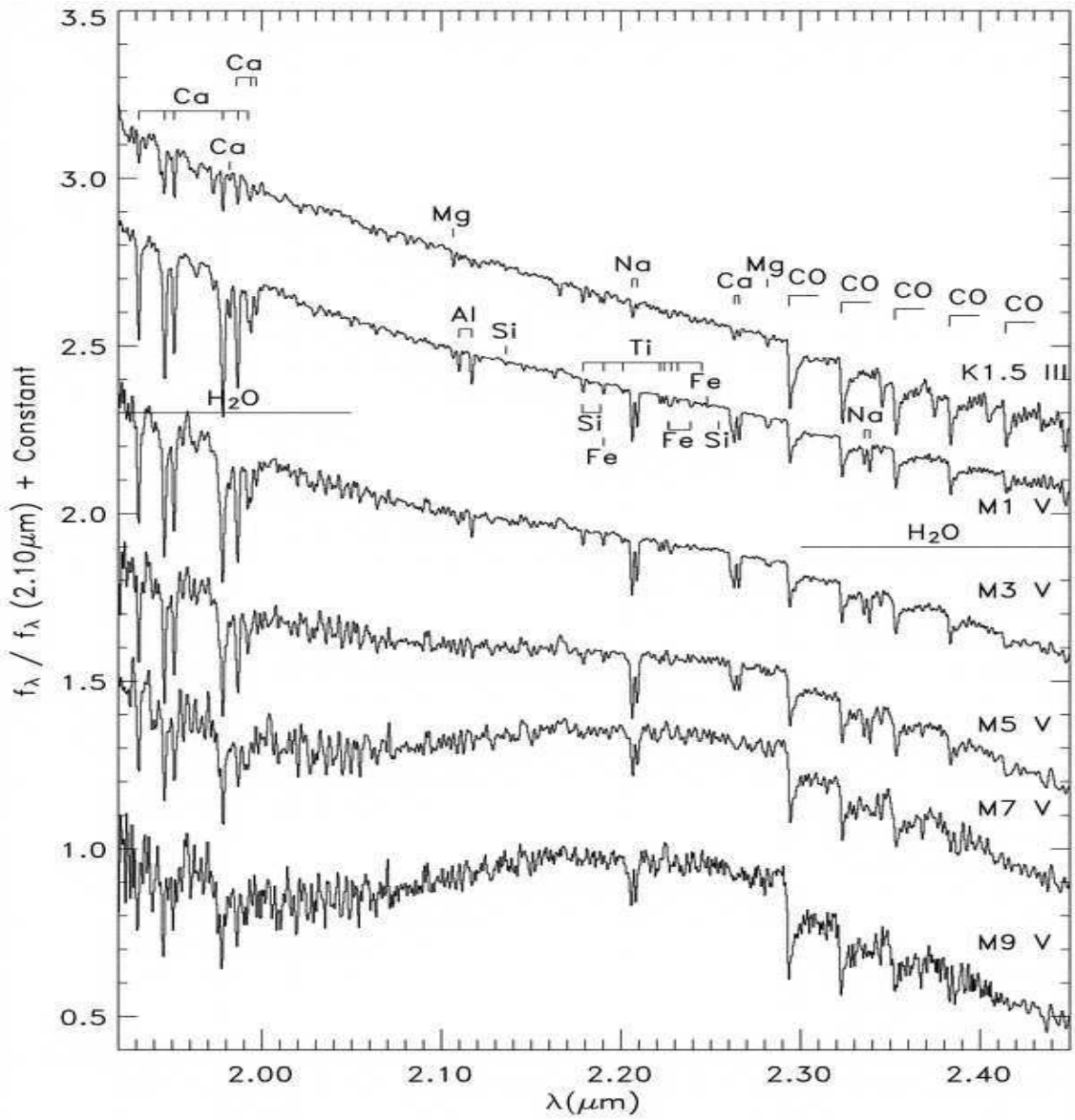

Figure 2.6 – K-band spectra sequence of M-dwarfs (Cushing et al. 2005). The most prominent molecular and atomic features are indicated.

temperature scales and now allows us to extend the temperature calibrations confidently to stars over the full range of parameter space. As an important first step, a conversion between spectral type and temperature is required.

The resulting scale may give results which differ significantly from an accurate conversion rule, but in the absence of a robust determination of the temperature scale at young star ages (e.g., from eclipsing binaries), this scale offers a reasonable way of interpreting spectral types and luminosities in terms of star masses and ages within current evolutionary models. The determination of M dwarf effective temperatures has been refined considerably since the work of

Veeder (1974); Pettersen (1980); Bessell (1991). They fitted blackbody curves through broad-band colours and the points of an assumed observed continuum. Tsuji et al. (1996b) provided, good $T_{\rm eff}$ values using IRFM. Casagrande et al. (2008) provided a modified IRFM $T_{\rm eff}$ for dwarfs, including M-dwarf. The $T_{\rm eff}$ scale of M-dwarfs can be developed by using a set of evolutionary models. Luhman (1999) initially adopted a $T_{\rm eff}$ which is based on the NextGen and AMES-Dusty evolutionary models of (Baraffe et al. 1998a) and (Chabrier et al. 2000), respectively. Luhman et al. (2003) then adjusted this $T_{\rm eff}$ scale further, so that the sequences of IC 348 and Taurus at $\leq$ M9 were parallel to those model isochrones on the Hertzsprung-Russell diagram. Their $T_{\rm eff}$ conversion is likely to be inaccurate at some level, as it falls between the scales for dwarfs and giants. However, even the current empirical methods (Berriman et al. 1992; Jones et al. 1994) still assume that nearly pure thermal radiation escapes from an M-dwarf atmospheres at some wavelength. Such an assumption is reliable only for optically thick layers of a non-convective atmosphere but models strongly suggest that M dwarf atmospheres are convective out to optical depths as low as $\tau \backsim 10^{-3}$. The photospheric structure of an M dwarf is much more sensitive to opacity caused by TiO and H_2O. Thanks to the large improvement in knowledge about the source of atomic and molecular line opacities, particularly for TiO (which dominate the optical spectral range) and for H_2O (which dominates in near-infrared range), as well as to revised estimates of solar abundances (Asplund et al. 2009; Caffau et al. 2011), there now appears to be much improvement in the $T_{\rm eff}$ scales obtain using a given model atmosphere over entire spectral sequence of M dwarfs (Rajpurohit et al. 2013).

2.3.2 Gravity

The problem of gravity is to be determined with sufficient precision since a small error in log g causes a large error is radius or age. Although the infrared spectra of late-type M-dwarfs are strongly affected by the presence of water bands, many atomic features can be resolved by careful observations. Some of the atomic features have proved to be fairly sensitive to changes in effective temperature and metallicity. We still lack, however, any direct measurements for the age of low mass stars, for which age becomes an important parameter. For example a $0.2M_{\odot}$ object takes 0.2 Gyr to reach the main sequence, a $0.1M_{\odot}$ object takes 1 Gyr whereas a $0.075M_{\odot}$ object takes 2.5 Gyrs (Burrows et al. 1997; Baraffe et al. 1997, 1998a). A reliable measure of age for low mass star is therefore vital for locating them on a Hertzsprung-Russell diagram. Not only $T_{\rm eff}$ and metallicity but also surface gravity is sensitive to age. If we can measure surface gravity accurately then in principle we can distinguish between young cooling brown dwarfs and old late-type M-dwarfs with similar colours (Viti & Jones 1999). Gravity-sensitive spectral features due to Na I, K I, H_2O complicate the measurement of spectral types but also provide valuable constraints on the ages of late-type dwarfs. In particular, these features offer a means of confirming the youth, of candidate low-mass members of young clusters and associations. The prominent CaH molecular absorption bands in M dwarf optical spectra are often used as gravity indicators. Typically, M dwarf spectra are collected with lower resolution because of their intrinsic faintness and so require broad 30-50Å-wide indices. Early surveys for M-dwarfs and young brown dwarfs used optical spectroscopy of Na I, K I, CaH, and VO for this purpose

(Luhman et al. 1997; Shkolnik et al. 2009); similar features were soon recognized at near-IR wavelengths as well (Luhman et al. 1998). Figure 2.7 show the effect of gravity and the pressure broadening of the Na I doublet. The variation of gravity sensitive lines with star age has been examined by Viti & Jones (1999).

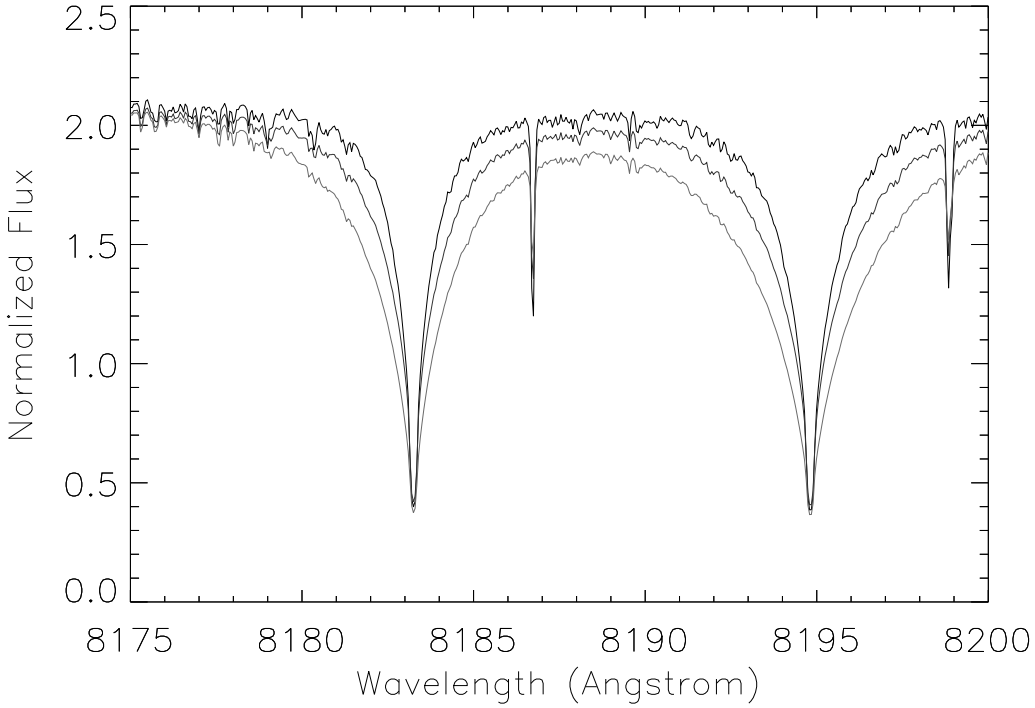

Figure 2.7 – BT-Settl models for an effective temperature of 3500 K and varying log g = 4.5 (black), 5.0 (blue), 5.5 (red). The effect of gravity and the pressure broadening of the Na I doublet is clearly visible.

2.3.3 Metallicity

The chemical analysis of M-dwarfs is notoriously difficult, owing to the complex molecular spectra of their cool atmospheres (Mould 1976a; Gustafsson 1989). Mould (1976a) was the first to explore systematically the strength of M dwarf spectral features as a function of metallicity, constructing a grid of synthetic model atmospheres that included molecular opacities and spanned a temperature of 4200-3000 K and a metallicities of [Fe/H]=-2.0 - 0.0 dex. This study gave rough estimates of metallicity for M-dwarfs and established several foundation for subsequent investigations of M-dwarfs dealing with, for example, the metallicity sensitivity of TiO absorption and the gravity sensitivity of CaH absorption. Substantial progress in metallicity estimation for M-dwarfs has been made recently, using both photometry and spectroscopy although, the faintness characterizing the M-dwarfs has limited the number of high-resolution, high signal-to-noise studies. Insufficient resolution and the presence of dominant molecular

features in the spectrum make it difficult to derive the accurate atomic line strengths needed to make reliable metallicity estimates. Metallicities have been derived via photometric calibrations. Photometric techniques are based on the higher optical opacity present in metal-rich stars, which shifts visible light into the infrared (e.g. Delfosse et al. 2000; Bonfils et al. 2005) analyzed V and K band photometry for 20 wide M-dwarf binary companion to FGK-dwarfs whose metallicities could be determined reliably via standard spectroscopic techniques. Assuming that both binary components inherit the same metallicity from their parent molecular cloud material, Bonfils et al. (2005) assigned the metallicity measurements for each primary stars to its M-dwarf secondary and so derived iso-metallicity contours in the M_V vs. V-K_s colour-magnitude plane.

Bonfils et al. (2005) first calibrated this relationship using spectroscopic metallicities derived for metal-poor early-M-type dwarfs by Woolf & Wallerstein (2005); later groups modified this work and addressed its limitations (Johnson & Apps 2009; Schlaufman & Laughlin 2010). Photometric techniques have generally been limited by the requirement for a sufficiently high absolute magnitudes of the targets, although the new technique presented in Johnson et al. (2011) depends on colour alone. Empirical spectroscopic techniques have also been developed, which rely on calibrations using the strength of specific optical (Woolf & Wallerstein 2006) or near-infrared K-band (Rojas-Ayala et al. 2010) features. Rojas-Ayala et al. (2010) used NaI, CaI, and H_2O spectral features to model metallicity, and calibrated their model using M dwarf companions to FGK stars, with an uncertainty of ±0.15 dex. Bean et al. (2006a) analyzed optical spectra with R ≥ 50 000 and signal-to-noise ratios between 200 and 400 of three stars. They used the methods developed in Bean et al. (2006b) making a fitting to their synthetic spectra for 16 atomic lines in the spectral intervals 8326 Å to 8427 Å and 8660 Å to 8693 Å, as well as for the TiO band-head at 7088 Å. They simultaneously determined $T_{\rm eff}$,metallicity, broadening parameters and continuum normalization factor from the spectral data. Bean et al. (2006b) used data from five wide binary stars with FGK primaries and M-dwarfs secondaries to evaluate their methods.

2.4 M-subdwarfs

The metal-poor stars of the thick disk and spheroid provide an invaluable record of Galactic history. The main-sequence FGK subdwarfs have proven to be an important source of information on these populations (e.g., Carney et al. 1994). The much cooler and fainter M subdwarfs offer an important alternative tracer group. Indeed, in addition to the possibility of observing the proper motion of nearby M subdwarfs, it is now feasible to obtain photometry for the M subdwarfs in globular clusters and also spectra for M-dwarfs and M subdwarfs at distances of a few kiloparsecs above the galactic plane with a telescope of 10-meter class (Reid & Gizis 1997). Using these M-dwarfs as probes of Galactic structure, however, requires a good understanding of their properties in order to derive accurate metallicities and luminosities for them.

Cool M-type subdwarfs (sdMs) appear less luminous than their solar-metallicity counter-

parts because their atmospheres are deficient in metals (Baraffe et al. 1997). The search for M subdwarfs is hampered not only by the fact that metal-poor stars are both rare and intrinsically faint but also because late-type M subdwarfs do not show exceptionally red colours typical of ultracool M dwarfs and brown dwarfs (Lépine et al. 2003a). They appear less luminous because their atmosphere is deficient in metals (Baraffe et al. 1997). Owing to their lower metallicity and intrinsic faintness, M subdwarfs lie below their solar-metallicity counterpart in the H-R diagram. Subdwarfs are typically very old (10 Gyr or more) and probably belong to the old Galactic populations: old disk, thick disk and spheroid, as shown by their spectroscopic features, their kinematic properties and their ages (Digby et al. 2003; Lépine et al. 2003a; Burgasser et al. 2003). They also exhibit high proper motions and high heliocentric velocities (Gizis 1997). As the low-mass subdwarfs, with their extremely long nuclear burning lifetimes, were presumably formed early in the Galaxy's history, they are important tracers of Galactic structure and of chemical enrichment history. In addition, detailed studies of their complex spectral energy distributions give new insights into the role of metallicity in the opacity structure, chemistry and evolution of cool atmospheres, and information about the fundamental issues of spectral classification and temperature vs luminosity scales. (Gizis 1997) proposed a first classification of M subdwarfs (sdM) and extreme subdwarfs (esdM), based on TiO and CaH band strengths in low resolution optical spectra. Lépine et al. (2007) has recently revised that classification and has proposed a new classification for the most metal-poor stars, the ultra subdwarfs (usdM). Jao et al. (2008) compared model grids with the optical spectra to characterize the spectral energy distribution of subdwarfs using the three parameters temperature, gravity, and metallicity. They thus gave an alternative classification scheme for subdwarfs. Despite the rather large number of them in the Galaxy, very little is known about them because their intrinsic faintness makes it difficult to get a homogeneous sample of unique age and metallicity. Moreover, the atmospheric parameters and the mass-luminosity relation for sdMs stars have long remained uncertain because of the lack of very low-mass stellar models. Despite the availability of low mass model atmosphere and synthetic spectra, it has still proven difficult to separate the effects of reduced metallicity from those of increased gravity or reduced effective temperature, since these factors all affects the pressure structure of the photosphere in similar way (Allard 1990a; Allard & Hauschildt 1995a).

Cool subdwarfs have low metallicity, and therefore their opacities are different from those of dwarfs. With decreasing temperature, sdMs spectra show an increase in the abundances of diatomic and triatomic molecules in the optical and in the near-infrared (e.g SiH, CaH, CaOH, TiO, VO, CrH, FeH, OH, H_2O, CO). TiO dominates the opacity sources in the optical region, while the H_2O bands in the infrared have complex and extensive band structures. This leaves no window for the true continuum and creates a pseudo-continuum that only permits observation of the strongest, often resonance, atomic lines (Allard 1990a; Allard & Hauschildt 1995a). However, owing to low metallicity, the TiO bands are less strong, and so the pseudo-continuum is brighter as a result (fig. 2.8) . This increases the contrast with the other opacity sources such as hydride bands and with atomic lines from atoms subjected the higher pressures of the deeper layers from which they emit their radiation.

Atmospheric models show that metallicity variations in cool and ultra-cool stars have dramatic effects on their optical spectra (Allard & Hauschildt 1995a). This is useful because low-

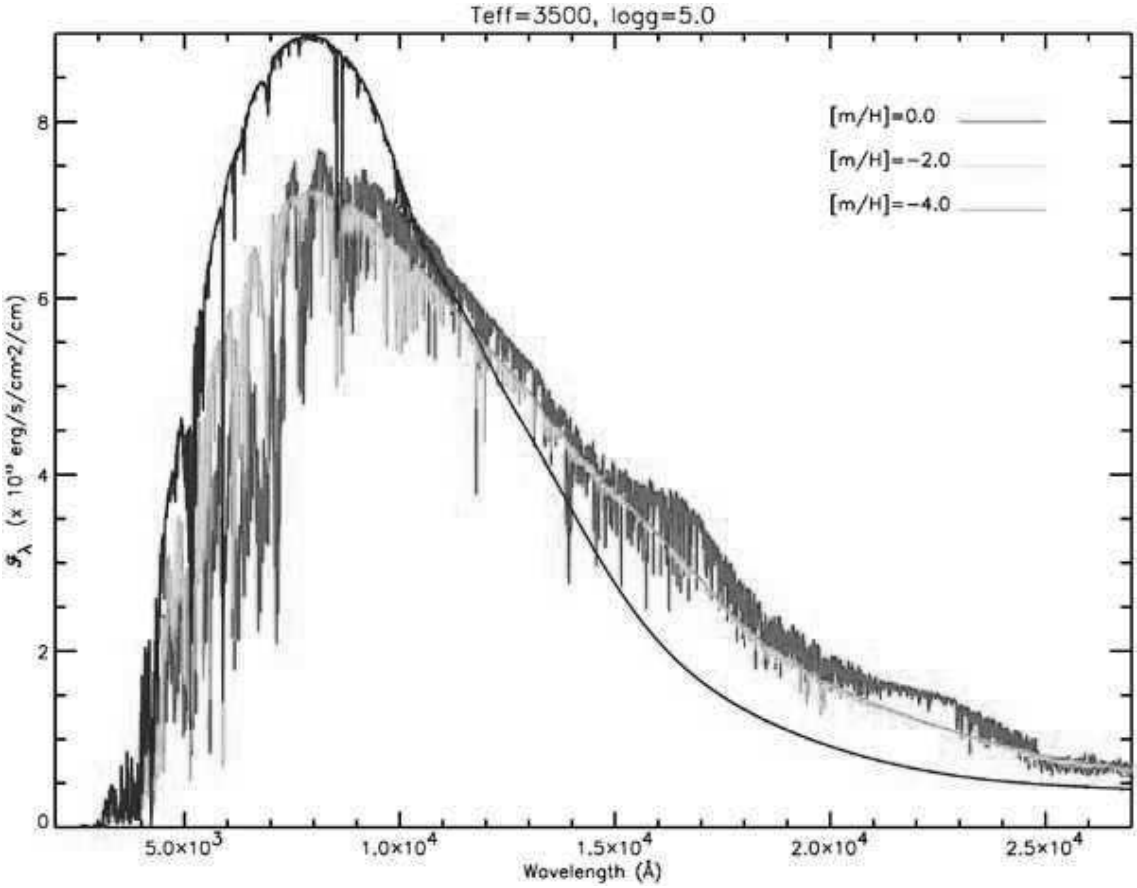

Figure 2.8 – Synthetic spectra for stars having $T_{\rm eff}$ = 3500 K and log g = 5.0 (Jao et al. 2008). The red, green, and blue lines represent different metallicities, 0.0, -2.0, and -4.0. Note that the relative amounts of blue and red fluxes tend toward bluer objects at lower metallicities.

resolution spectroscopy is sufficient for measuring both effective temperature and metallicity effects. Metallicity effects on the physics of cool atmospheres have been studied both from models and from SED (Allard 1990a; Leggett et al. 1996, 1998; Burgasser 2002). The M subdwarfs in binary and multiple systems for which the metallicity of the hotter primary is known as well as clusters with VLM stars of the same age and metallicity, both offer more promise as test of metal poor evolutionary and atmosphere models. The primary effects of metallicity are the strengthening of hydride bands (OH, FeH), the appearance of pressure induced absorptions by H_2 around 2 μm relative to double metal (TiO,VO) bands and the broadening of atomic lines. We therefore see these molecular bands in more details than for M-dwarfs and under more extreme gas pressure conditions. This can reveal the inaccuracy or incompleteness of the opacity sources used in the model. This difficulty, combined with a lack of accurate line lists for molecular hydride absorption bands, has hampered efforts to obtain the atmospheric parameters of observed M subdwarfs by using spectral synthesis. Subdwarfs were generally identified from optical and proper motion catalogues and from photographics plates at different epochs (Scholz et al. 2000; Lépine et al. 2003a; Lodieu et al. 2005). Several surveys have been conducted to search for subdwarfs over a wide temperature range, including hot, intermediate and cool components. The range of metallicity of subdwarfs, extreme-subdwarfs and ultra-subdwarfs span

approximately -0.5 and -1.0, -1.0 and -1.5 and below -1.5 dex, respectively (Gizis 1997; Woolf et al. 2009). M-type subdwarfs have typically $T_{\rm eff}$ below $\backsim$3500-4000 K (depending on the metallicity Baraffe et al. (1997); Woolf et al. (2009)) and should display high gravity ($\log g \backsim$ 5.5) although some variations is seen amongst low-metallicity spectra (Jao et al. 2008).

Chapter 3

A Model Atmosphere For Low Mass Stars

3.1 Introduction

When we examine the spectrum of a star we are measuring information about the frequency distribution of its radiation field. We observe the broad expanses of the spectrum in which the frequency distribution is relatively smooth, the continuum, and, in addition, many narrower features, spectral lines and/or bands, which give relatively sharp peaks superposed on the background continuum. The former regions arise from the emission and absorption of photons by atoms in various process involving transitions to free states, either from an initially bound state (photo-ionization) or free states (free-free transitions). The complete spectrum implicitly contains an enormous amount of information about the physical state of the atmosphere of the star. It will be our primary goal to recover this information, although drawing reliable inferences from all this physical information provided by observations is by no means an easy task. The relevant data are often difficult to acquire, since frequently the observed spectra are just the end product of the interactions within complicated physical structures. For example, in any given spectrum the radiation we observe originates from a wide range of levels in the atmosphere, deep layers contribute to the relatively transparent continua while higher layers contributes to the more opaque lines.

The rate of discovery of low-mass stars has accelerated in recent years. It is thus now possible to investigate the formation and early evolution of stars in a previously unexplored mass regime. Determining the physical properties of low-mass stars is important for our understanding not only of planet formation but also of circum-stellar disks, of dust formation in cool atmospheres, and of the initial mass function. The direct measurement of mass and/or radius for low-mass stars is possible only for certain rare binary systems. Determining other physical properties such as effective temperature and surface gravity from bolometric luminosity estimates requires a precise distance measurement and also assumptions about age (to determine effective temperature), mass and radius (to infer a value for the surface gravity from

evolutionary models) (Rice et al. 2010; Rajpurohit et al. 2012b). Although radius is not expected to vary very much for objects older than a few 100 Myr, the reliance on evolutionary models is problematic, since they are poorly calibrated for stars with a young age. Commonly used conversions from spectral type to effective temperature (e.g., Golimowski et al. (2004) for field objects and Luhman et al. (2003) for young M dwarfs) rely on model isochrones and on a monotonic relationship between spectral type and effective temperature, which might not represent accurately the complicated formation and evolution of low-mass objects (eg., Stassun et al. 2006). Evolutionary models also require atmospheric models to provide boundary conditions. Thus, synthetic spectra from such atmosphere models potentially offer a more direct method of inferring physical properties by means of a comparison with observed spectra. Advances in spectroscopy and photometry, especially at infrared wavelengths, promise to give a wealth of new data on low-mass stars. Making parallel improvements in models of cool stellar atmospheres is thus very important if the full potential of these data is to be realized.

Some of the most important challenges to the modelling of stellar atmospheres and spectroscopic properties arise in describing high temperature molecular opacities and cloud formation. Early M dwarfs shows the onset of the formation of water vapours at $T_{\rm eff}$ around 2000-3900 K. Dust aerosols form in the upper atmospheric layers of late-type M dwarfs ($T_{\rm eff}$ $\leq$ to 2900 K). At the hydrogen-burning limit, the peculiar spectral distribution (Kirkpatrick et al. 1993b) suggests that all signs of the TiO bands disappear from the optical spectrum, leaving only atomic lines and perhaps VO bands (Kirkpatrick et al. 1995), CaH, CaOH, and/or FeH bands. As the effective temperature drops for stars in the brown dwarf regime, methane (CH_4) features begin to appear (Tsuji 1995; Allard et al. 1996; Marley et al. 1996) and corundum (Al2O3), perovskite ($CaTiO_3$), iron, enstatite ($MgSiO_3$) and forsterite (Mg_2SiO_4) clouds may form, enhancing the carbon/oxygen abundance ratio and profoundly modifying the thermal structure and opacity of the photosphere (Sharp & Huebner 1990; Fegley & Lodders 1996). The chemistry of cool dwarf atmospheres is, therefore, a complex nonlinear problem requiring a detailed knowledge of the concentration of atoms and molecules. This prevents the straightforward derivation of quantities such as excitation temperatures and metallicities from line strength ratios which is possible for hotter stars. The most reliable way to estimate effective temperatures and metallicities of low-mass stars, and also to identify substellar brown dwarfs is by making a direct comparison of observed and model spectra.

3.2 Historical Overview

Theoretical work on the atmosphere of M dwarfs has progressed along lines parallel to those followed in the study of other classes of stars. Advances in the atmospheric modelling of cool stars are hampered by (a) incomplete molecular opacity data bases and (b) the inability to handle convection process rigorously. Even if these problems are addressed reasonably well, further problems arise in describing the effects of photospheric grain formation, chromospheres and magnetic fields, as well as departures from local thermodynamic equilibrium and spatial variations in atmospheric structure due to starspots, which influence cloud formation and general

weather patterns. The earliest work by Mould (1975) and Mould (1976a) was aimed solely at constructing models of the photosphere, in which the only relevant energy fluxes were considered to be thermal (radiative plus convective). Later models have become increasingly sophisticated as improvements in opacity calculations in the equation of state used, and due to the revised solar abundances and progress in completeness and quality of molecular line lists. As a result, spectrophotometric data on M dwarfs can now be fitted rather well by current models.

The interior and evolutionary models of M dwarfs can be constrained systematically by carrying the integrations inward and constructing credible models of the stars. In this regard, the M dwarfs are in a somewhat unique position because they bracket the mass range in which the main-sequence stars are believed to be completely convective. Slight errors in the assumed surface parameters and in modelling techniques can lead to large uncertainties in the predicted interior structure. The study of M dwarfs may allow one to check the constitutive thermal physics which enter into the study of all stars. The combination of high gravity and low $T_{\rm eff}$ in M dwarfs ensures that molecular formation occurs. The number density of molecules (eg., H_2) becomes a significant fraction of the atomic number density (eg., H), or even exceeds it at certain levels in the atmosphere. Historically, model atmospheres for M dwarfs have evolved in the direction of attempting to give an increasingly realistic treatment of the double complexities of molecule formation and of optically thin convection. Dust may form even in the coolest star if no chromosphere is present. Molecules and dust have an especially serious effects on the opacities, increasing them by a factor of up to 10^5 relative to purely atomic values. The earliest thermal model atmosphere for M dwarfs (Tsuji 1966) ignored convection altogether but included the opacities due to H_2O, H_2, and CO. Vardya (1966) treated convection, using the mixing-length formalism of Henyey et al. (1965), and derived thermal models in which the molecular equilibrium of 160 species (including TiO, CaH, MgH) were subsequently evaluated. Radiative fluxes from the models were found to fit R-I colours well, but predicted colours at shorter and longer wavelengths became increasingly poor, presumably because of the lack of major sources of line opacity. A better treatment of H_2O line opacity made it possible to obtain more realistic emergent flux distributions from his models.

Auman (1969) applied his extensive H_2O opacity calculations to cool stars and devised a method of replacing the effect of a large number of closely spaced lines by a representative mean opacity. This was an important step forward in modelling the thermal photospheres of cool dwarfs. Auman (1969) found that in the M dwarfs (despite the strong TiO bands in M dwarf spectra), H_2O is the dominant source of opacity at $T_{\rm eff} \leq 2500$ K. In the presence of H_2O, the surface temperature falls below the values which would occur without H_2O; this occurs because the H_2O spectrum reaches its maximum on the red side of the Planck peak in these stars. Metal abundances in M dwarfs may differ from solar ones by a factor of 2 to 3 (Mould 1978) and produce atmospheric temperature variation of several hundred degrees. Lack of TiO in these models makes Auman (1969) predicted colours less accurate in the visible region. Mould (1975, 1976b) was the first to produce an extensive grid of convective M dwarf model atmospheres for $T_{\rm eff}$ between 4750 and 3000 K. The models effectively combined the ATLAS code (Kurucz 1970) with a treatment of TiO band model opacities and chemical equilibrium by Tsuji (1966, 1973), of H_2O opacities by Auman (1969), together with a mixing-length treat-

ment of convection (Böhm-Vitense 1958). Mould (1976b) obtained emergent spectra which could be fitted rather well to RIJHKL filter data for several M dwarfs. In particular the strong TiO bands and H_2O bands appear prominently in the emergent fluxes from the Mould (1976b) model. Mould & Hyland (1976) exploited information contained in many bandpasses, distributed across a broad spectral range, to derive $T_{\rm eff}$ values for 20 M dwarfs with an precision of ± 100 K at 4000 K and ± 200 K at 2850 K. These represent substantial improvements in accuracy compared with the $T_{\rm eff}$ values obtained by fitting a single observed colour (R-I) to the predicted colour of the model.

Over the last two decades, a tremendous improvement in the model atmospheres for low mass stars has been achieved. The work of Allard (1990a) and (Kui 1991) finally broke the 3000 K barrier in $T_{\rm eff}$ by applying the model codes of Wehrse (1972). Wehrse (1972) had treated the more extreme atmospheric conditions of cool white dwarfs ($T_{\rm eff} \backsim 7000$ K). Apart from the dominant opacity sources such as TiO and H_2O, both the authors included a number of important molecular bands which are important in low-metallicity subdwarfs, such as those of hydrides (CaH, MgH, SiH, OH, CH), as well as those VO (Keenan & Schroeder 1952) and CO which give the characteristic molecular bands in the red and infrared regime, respectively, and which act as sensitive temperature indicators (Henry et al. 1994; Kirkpatrick et al. 1995; Martin et al. 1996). The new $T_{\rm eff}$ sequence for M dwarfs (Kirkpatrick et al. 1993b) used the model grid from Allard (1990a) that casts new light on traditional results based on blackbody methods. This new $T_{\rm eff}$ sequences for M dwarfs is 500-K higher at a given luminosity and shifted the predicted positions of the late-type dwarfs in the HR diagram from cooling tracks to the blue side of the theoretical lower main sequences (Dantona & Mazzitelli 1985; Burrows et al. 1989, 1993). This made it more likely that field late-type M dwarfs were hydrogen-burning stars rather than young, contracting, substellar brown dwarfs. By introducing the laboratory oscillator strengths for the TiO bands, Allard et al. (1994a) resolved most of the remaining discrepancies in the optical model spectra that had been pointed out by Kirkpatrick et al. (1993a); Gustafsson & Jorgensen (1994) and Jones et al. (1994). Failing to allow for the presence of the correct absorbers the success with the thermal models there are still some problems concerning the modelling of cool photospheres. Missing absorbers (in particular at very low temperatures) may lead to grossly incorrect calculated opacities. The oscillator strengths of some important bands are also still poorly known.

3.3 Model Construction

Late type dwarfs have been particularly difficult to model, mainly because i) cool stars have complicated equations of state, with large number of composite particles (including dust at low temperatures), ii) The absorption is dominated by a very large numbers of lines, in particular molecular bands (plus dust at very low temperatures), iii) the strong wavelength dependence of opacities may lead to difficulties in finding the stratification structure which fulfills the energy equation, in particular by using temperature correction methods which use weighted mean

opacities, iv) very accurate modelling is required if an important absorber such as H_2O which has a great influence upon the stratification reacts sensibly to stratification changes, v) gravity-sensitive feature are very hard to find at low temperatures, vi) since all elements are coupled with each other via the molecules and grains in the state equation, a consistent set of element abundances has to be determined instead of carrying out an element by element analysis, viii) treatment of convection by a mixing-length method is required. The extension of computing capacities made it possible to pass from an analytical treatment of the transfer equation using moments of the radiation field (Allard 1990a) to a line-by-line opacity sampling in spherical symmetry (Allard et al. 1994a, 1997; Hauschildt et al. 1999) and more recently to a study of 3D radiation transfer (Seelmann et al. 2010). These steps have made it possible to model the complex atmosphere of M dwarfs. In parallel with these development detailed hydrodynamical simulation have been developed to give a realistic representation of the granulation and its resulting induced line shifts for the sun and sun-like stars (see e.g. the review by Freytag et al. 2010)

The photosphere is the part of the atmosphere which is responsible for the SED. It is easy to model the photosphere by ignoring the magnetic fields, using radiative transfer models and radiation hydrodynamical (RHD) simulation. With the exception of the ultraviolet and visual spectral range for flaring stars and their resulting emission lines, it is a good approximation to ignore magnetic field when modelling the neutral photosphere (from which most of the emitted flux emerges) when dealing with low mass stars and brown dwarfs. Classical model atmospheres differ from one another in their construction philosophy, which varied according to the period of their initial development. The code by Tsuji (1965, 2002), the ATLAS code by Kurucz (1973) and the MARCS code by Gustafsson et al. (1975, 2008) put most of their efforts into limiting memory requirements and reducing computing time. The PHOENIX code (Allard et al. 1994a, 2001, 2012a) on the other hand, to distinguish itself from its predecessors, took the approach of computing the opacities during the model execution. This involves computing the opacities for billions of atomic and molecular transitions on-the-fly, together with a selection of the most important spectral lines. This approach makes PHOENIX much slower than former codes, but allows it gives a more consistent account of important physical phenomena, such as those involving a modification of local elemental abundances throughout the atmosphere (due to diffusion and cloud formation).

The traditional assumptions of plane-parallel stratification in homogenous layers, of stationary hydrostatic equilibrium, of mixing-length convection and of local thermodynamic equilibrium (LTE) have been relaxed step-by-step. Asplund et al. (1999, 2000) developed 3D simulations with proper hydrodynamics and with radiation fields taken into account for solar-type stars. Freytag et al. (2002, 2012) and Allard et al. (2013) developed a full star-in-a-box models for supergiants and sun like stars. These simulations show a striking agreement with observations of solar granulation and spectral line profiles for solar type stars. They clearly demonstrate the qualitative difference between traditional 1D models and reality; while the temperature structure in the upper layers of the 1D models is determined by radiative cooling and heating, the radiative heating in real late-type stars is balanced to a significant extent by the expansion

cooling of upwelling gas. Achieving consistent treatment of radiative transfer in models for late-type stars without using the assumption of LTE is complicated because of the great number of atomic and molecular species affecting the radiation field; the wealth of levels and transitions in these species and the lack of basic data for these transitions-not the least of which is the lack of cross sections for atomic and molecular collisions with electrons and hydrogen atoms.

3.4 Molecular Opacities in M dwarfs

The SED in M dwarfs are entirely governed by molecular absorption bands that leave no window for the true continuum in the emergent flux. Russell (1934) and de Jager & Neven (1957) showed that most of the molecules play an important role in cool star atmospheres. Since the structure of the cool M dwarfs atmosphere is extremely sensitive to opacity sources which absorb on the Wien (or blue) side of the energy distribution, it is important to consider carefully all major molecular bands and atomic opacities. The TiO band is the primary source of opacity in M dwarf spectra in the optical region, while H_2O is an important source of opacity in the low temperature regime in the near infrared. Allard et al. (1994b) showed how important H_2O is for total opacities in the lower temperature regime, and how critically the description of this effect depends on the computational techniques used (e.g., the use of opacity sampling (OS), or SM, the wavelength resolution used and the coverage of the model spectrum). They did this by comparing Rosseland mean opacities from various authors, sources and techniques. These models were than tested my Leggett et al. (1996) by comparing them with the low resolution spectra and photometry of M dwarfs later on Leinert et al. (1998) compared the low resolution spectra of M dwarfs with the pure gas phase NextGen model atmospheres (Allard et al. 1997; Hauschildt et al. 1999). Leinert et al. (1998); Leggett et al. (1998, 2000) used the AMES-Dusty models Allard et al. (2001) which assume insufficient gravitational settling assumed, meaning that the dust is distributed according to the chemical equilibrium predictions.

The TiO line list by Plez (1992); Jorgensen (1994a) led to M-dwarf models which were great improvements upon previous models based on an SM treatment of opacities (Mould 1975; Kui 1991; Allard & Hauschildt 1995a). Each TiO line list applied in an OS treatment of the opacities leads to better agreement with the observed optical absolute magnitude of M dwarfs (see e.g. Brett 1995a,b; Chabrier et al. 1996). The list of the line positions and relative band strengths of TiO lines given by Plez (1992) and by (Jorgensen 1994a) is large step forward for an accurate high resolution spectral syntheses analysis of M dwarfs. Leinert et al. (1998) compared the low resolution spectra with the pure gas phase NextGen model atmospheres (Allard et al. 1997; Hauschildt et al. 1999)

The most recent improvement in the models was the inclusion of an improved TiO line list by Plez (1998). Based on these new data, the total TiO opacity effect is much reduced and also the typical line spacing of TiO transitions is much larger than that previously assumed. This invalidates the use of the SM technique for this molecule and has potentially sweeping

consequence for the study of atmospheric parameters, since TiO is even more important than H_2O. Brett (1994) has computed new M dwarf model atmospheres, expanding on the work of Kui (1991), which included water lines derived from the data of Ludwig (1971) as well as the earlier TiO line list of Plez (1992). Allard et al. (1994a) used the preliminary H_2O line list by Miller and Tennyson to evaluate the effects of a sufficiently line-by-line treatment of water opacities. Since this list is preliminary and does not yet extend to high quantum number J, it misses important sets of weak lines at the minima of the water opacity profile (at 1.2,1.6 and possible 2.2 μm). This leads to far too much flux emerging at those wavelengths in the synthetic spectra of M dwarfs. Impressive progress has also been made in the study of molecular absorption, of which little was known 30 years ago (see Jorgensen 1994b, for reviews). The lists are based on laboratory measurements of wavelengths and gf values with simple theoretical extensions, or are the result of more extensive quantum-mechanical ab-initio calculations. Even if the absorption cross-sections are not yet always of satisfactory quality, the existence of these lists makes it possible to calculate models for, e.g., M and C stars that are realistic enough to give results which compare reasonably well with observations. Very extensive line lists have thus been calculated for most diatomic and poly-atomic molecules that contribute to opacity effects in stellar atmospheres.

The model of Allard et al. (2012a, 2013) included a pure ab initio list of more than 6.2 million H_2O transitions. More realistic model atmospheres and synthetic spectra for low-mass stars, brown dwarfs and extra solar planets, using line-by-line or opacity sampling techniques, have been made possible owing to the development of accurate opacities values often calculated ab initio. The improvement has been especially remarkable in the case of the water vapour line list. Nevertheless the model atmospheres have failed to reproduce the strength of the water bands that shape the low resolution infrared SED of M dwarfs. The discrepancies in the model synthetic spectra were therefore believed to be due to an inaccurate or incomplete description of molecular opacities. In particular water vapour was suspected because the discrepancies were observed at infrared and wavelengths in the relative brightness of the flux peaks between water vapour bands. Fig. 3.1 show the comparison of the infrared spectra of M8 dwarfs VB10 (Allard et al. 2012b) with the synthetic spectra published since 1999. From figure 3.1 it is clear that the estimates of the water vapour opacity profile, which shapes this part of the spectrum, have strongly changed over time along with the improvement of computational capacities and with better knowledge of the interaction potential surface. More recently Allard et al. (2012b, 2013) added to the list of TiO transitions developed by Plez (1998) and BT2 water vapor line list, thus completing the evolution to a full line-by-line treatment of the major molecular opacities in M dwarfs and making it possible to reproduce the observations reasonably well for the optical and near-IR spectrum of cool M dwarfs (Rajpurohit et al. 2012b, 2013).

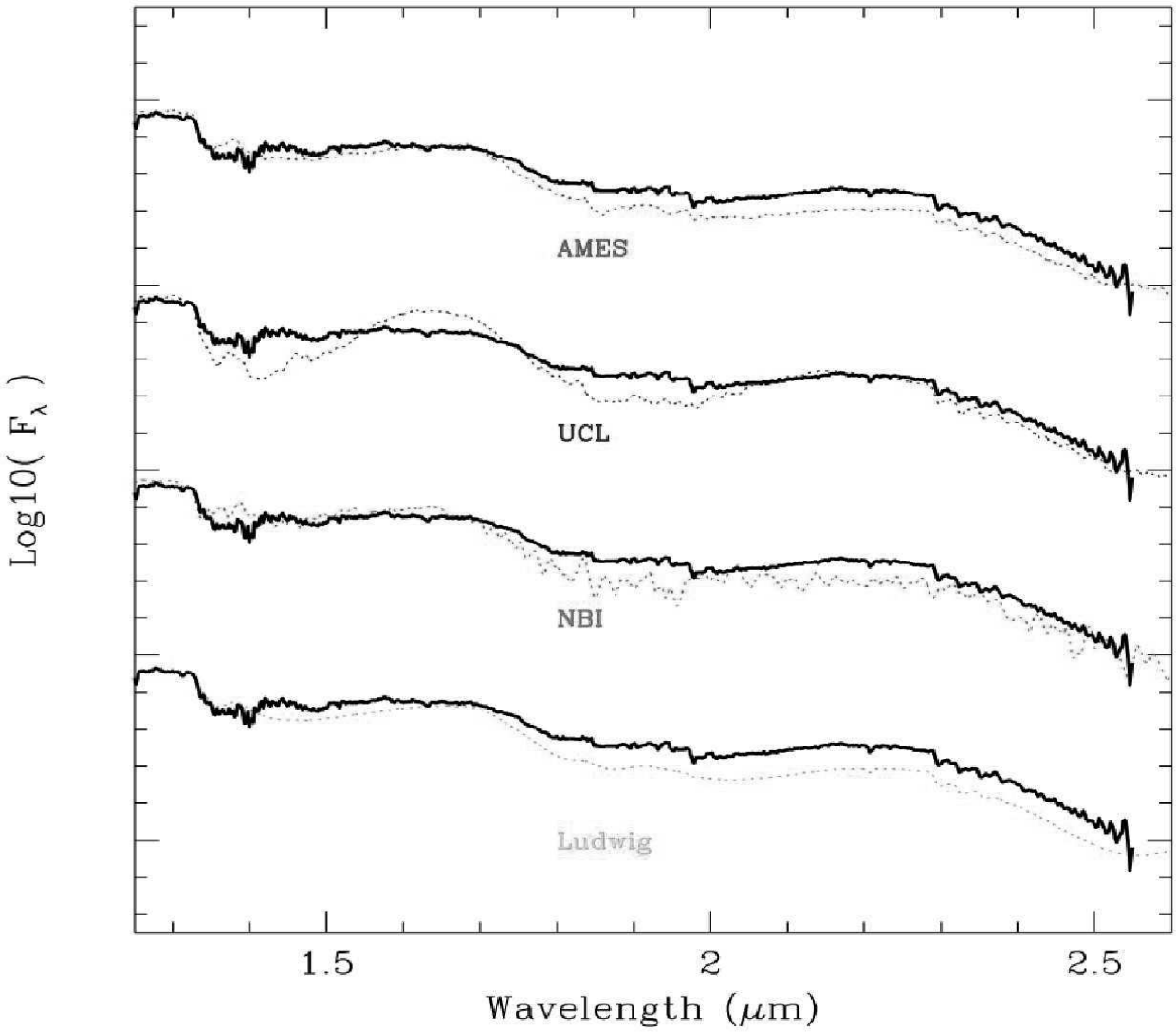

Figure 3.1 – Fig. 1 of the review article by Allard et al. (2012a). The near-infrared SED of VB10 is compared with the synthetic spectra (Teff = 2800 K, log g = 5.0, [M/H] = 0.0) from diverse model grids published through the years. All models (except the NextGen / UCL case) underestimate the flux in the K bandpass by 0.1 to 0.2 dex

3.5 Convective energy transport

Stars become fully convective throughout their interior and convection reaches furthest out in optically thin regions of the photosphere in M3 and in later dwarfs which have a $T_{\rm eff}$ below 3200 K (Allard 1990a; Allard et al. 1997; Chabrier et al. 2000). In most of the classical model atmosphere the convective energy transfer is treated using the Mixing Length Theory (MLT). This technique is scarcely adequate and modifications of it have been attempted by Ludwig et al. (2002) and Ludwig et al. (2006) by comparing the `PHOENIX` thermal structure obtained

using the MLT with that of RHD simulations. Kandel (1967a,b) found that the density inversion predicted in some earlier models might be attributed to deficiencies in the standard MLT formalism for treating convection (in which the MLT parameter $\alpha = \mathrm{L/H}_p$ is kept constant with depth). Kandel (1967a,b) therefore devised a modified MLT formalism in which the parameter α is allowed to vary with depth in such a way that the density inversion is eliminated. In recent years it has become apparent that the presence of a density inversion in a model may have little or nothing to do with errors in the MLT. Ludwig et al. (2002) and Ludwig et al. (2006) showed that the MLT could reproduce the horizontally averaged thermal structure of the hydro simulations when proper values of the MLT parameter are used. These values have been estimated for M dwarfs to vary with surface gravity from $\alpha = 1.8$ to 2.2 (2.5 to 3.0 for the photosphere).

The BT-Settl models of Allard et al. (2012a) use the mass and surface gravity dependent prescription of Ludwig et al. (1999) for hotter stars, together with an average values of α prescribed by (Ludwig et al. 2002, 2006) for M dwarfs. They also use the micro-turbulence velocities from the radiation hydrodynamical simulations of (Freytag et al. 2010), and the velocity field from the RHD simulations of Ludwig et al. (2006) and Freytag et al. (2010) in order to calibrate the scale height of overshoot, which becomes important for the formation of thick clouds in L dwarfs but is otherwise negligible for the SED of low-mass stars and brown dwarfs. Freytag et al. (2010) have indeed addressed the issue of mixing and diffusion in low-mass atmospheres by two dimensional (2D) RHD simulations, using the `PHOENIX` gas opacities in a multi-group opacity scheme, and including forsterite with geometric cross-sections. These simulations assume efficient nucleation, using initial monomer densities estimated from the total available density of silicon (the least abundant element in the solar composition involved in forsterite). They found that gravity waves form at the internal convective-radiative boundary and play a decisive role in cloud formation, while at around $T_{\mathrm{eff}} \approx 2200\,\mathrm{K}$ the cloud layers become thick enough to initiate cloud convection, which dominates in the mixing process.

Dark spots exist on the surface of certain M dwarfs, especially those which rotate faster than a critical velocity $\backsim$ 5 km/s (Noyes et al. 1984; Marilli et al. 1986). The activity-age correlation has been observed by West et al. (2011) when rotation rate of star is coupled with star age. The magnetic spot are cooler than the photosphere at least by several hundred degrees (ensuring quite different equilibria in the spot atmosphere than outside). The spot areas may be $\geq$ 10 percent of the disk area. The problem of energy transport through the star in the presence of such a gross inhomogeneity is one of great interest, part of the normal energy flux may be trapped beneath the surface, reducing the bolometric luminosity of the star. The surface activity in the M dwarfs has been observed to exhibit general characteristics that contrast with solar-type stars. While, as in solar-type stars, M dwarfs show little or no activity when the rotation rates reaches below a certain threshold ($\backsim$ 5 km/s Marcy & Chen 1992). By analogy with the Sun, spots and active region on M dwarfs are believed to be magnetic origin. Magnetic field of many kilogauss may exist on the surface of M dwarfs shows that M dwarfs are therefore more active than solar-type stars. This indicates that some change in the magnetic field generation and/or magnetic field of kilogauss strength certainly interfere with convective flow patterns in M dwarfs interact with the stellar atmosphere. Modelling an M dwarf chromosphere is a complex problem owing

to the complexity of the radiative transfer calculation in such cool, dense environment. Several attempt has been tried to model the M dwarfs chromosphere using hydrogen Balmer emission line observations (Cram & Mullan 1985). Ca II observation has also used to model M dwarfs chromosphere (Giampapa et al. 1982). But all these attempt were unsuccessful at fitting both Ca II and hydrogen Balmer lines in their quiescent and and flare observations. Currently there is no model who can predict all the major chromospheric activity observed in active M dwarfs atmosphere. Systematic development of hydrodynamical studies of chromosphere activity is still in progress to truly understand the cool dwarfs photosphere. The model atmospheres used here are only radial models which do not account for surface homogeneity. The models would therefore under-predict the $T_{\rm eff}$ and radius as a function of the contrast in temperature of the spots to the rest of the surface, and of the surface coverage of spots.

3.6 Dust Grain and Atmospheric composition in M dwarfs

The presence of dust in the circumstellar envelopes of M giants and supergiants is a common phenomenon but the location in the atmospheric structure of this dusty material is not known. In view of the presence of high densities, with correspondingly efficient formation rates, the star's photosphere would be a favourable place for the condensation of matter into solid particles. The surface temperatures of late M type stars of low mass and high luminosity are below the condensation temperature of various grains (e.g Al_2O_3, ZrO_2), so condensation clearly must be included in the calculations as indicated by the work of Sharp & Huebner (1990). The importance of condensation in the atmosphere of late-type M dwarfs and brown dwarfs has been confirmed by Tsuji et al. (1996a,b) who found large concentrations of such condensates in their model atmospheres. The M dwarf model atmosphere of Brett (1995b) and Allard et al. (1996) does not include the condensation of molecules into grains. In an M dwarf a $T_{\rm eff}$ value below 3000 K gives rise to cloud formation (involving iron, magnesium silicates or graphite grains) in the atmosphere, causing a strong variation in opacity with effective temperature. The effect on the temperature profile depends strongly on the particle size and on the vertical distribution of grains. The effect of condensation on the spectral distribution and atmosphere of cool dwarfs is to produce a gradual depletion of the gas phase abundance of titanium, iron, vanadium , and oxygen. The optical SED become more transparent if the opacity of the grains is ignored, which causes the TiO, VO, FeH, and metal-line opacities to decline with decreasing effective temperature of a star. The dusty model of (Tsuji et al. 1996b) was the first model atmosphere for M dwarfs and brown dwarfs which included not only grain formation but also grain opacities. Tsuji et al. (1996b) showed that including corundum, iron, and enstatite opacities by assuming arbitrary spherical grain sizes could heat the photospheric layers and change the overall structure of the atmosphere. This leads to the formation of weaker molecular spectral features than for models without grain opacities. This results in the predicted SED of late-type M dwarfs moving towards the red, which can reproduce the infrared broadband fluxes of the latest-type M dwarfs. A $T_{\rm eff}$ of 2600 K and below is sufficiently low to give rise to sufficient silicate dust formation in the photospheric layers to affect the spectral properties of late type M dwarfs. These grains produce a 'veiling' in the optical spectral region by dust scattering and also an

important greenhouse effect (redistribution of flux to the infrared) which strongly influence the infrared spectral properties. Tsuji et al. (1999); Allard et al. (2001) treated the dust formation in the low-mass stars in pure Chemical Equilibrium (hereafter CE). CE yields the formation of condensates from zirconium dioxide and silicates (Mg_2SiO_4) to refractory ceramics ($CaTiO_3$, Al_2O_3), salts (CsCl, RbCl, NaCl), and ices (H_2O, NH_3 , NH_4 SH_4). The models studied how these processes depend on the temperature of the atmosphere for stars of M through T and Y spectral types (Allard et al. 2001; Lodders & Fegley 2006). Helling et al. (2008a,b); Allard et al. (2012a) explored the properties of the formation of the dust clouds in low-mass stars by determining the radial distribution and average size of the grains.

Stars begin their life when an ordinary dense cloud of interstellar matter becomes unstable and begins to collapse. The elemental abundance within such a cloud of matter determines the composition of the stellar atmosphere which results from the collapse. The composition of a star is also a function of $T_{\rm eff}$ (which is determined by radiation either due to internal heat from nuclear fusion and contraction or from irradiation by a parent star), and to a lesser extent of surface gravity. Scaled solar abundances have been generally used for all elements relative to hydrogen. Additionally, some allowance has been made for the enrichment of α-process elements (C, O, Ne, Mg, Si, S, Ar, Ca, and Ti) because of the production of star-forming gas by the explosion of a supernova. The spectral energy distribution of M dwarfs is mainly diminished by the presence of oxides such as TiO and VO in the optical region and by water vapour and CO in the infrared region. This shows the importance of elemental oxygen abundances in their atmosphere. The revised solar abundances, based on RHD simulations and spectral synthesis analysis of the solar photosphere, due to Asplund et al. (2009) and Caffau et al. (2011) give an oxygen reduction of -0.11-0.19 dex compared with the previously used abundances of Grevesse et al. (1993). Different model atmosphere use different solar abundances; for example the BT-Settl model by Allard et al. (2012a) is based on the Asplund et al. (2009) solar abundance values, while DRIFT models by Helling et al. (2008b) use the Grevesse et al. (1993) solar abundances. The MARCS model by Gustafsson et al. (2008) uses the values of Grevesse et al. (2007). Fig. 3.2 shows the effect of using solar oxygen abundance estimates and compares the Casagrande et al. (2008) $T_{\rm eff}$ and metallicity estimates with the Baraffe et al. (1998a) NextGen isochrones (assuming an age of 5 Gyrs), using model atmospheres from various authors. The higher oxygen abundance causes models to appear too blue as compared with models based on the Asplund et al. (2009) values. The MARCS models of Gustafsson et al. (2008) based on the Grevesse et al. (2007) values on the contrary show a systematically increasing excess in J - Ks with decreasing $T_{\rm eff}$. The models are most sensitive to the choice of solar oxygen abundances for M dwarfs with $T_{\rm eff}$ around 3300 K, i.e. at the onset of water vapour formation in the atmosphere. Fig. 3.3 shows the same comparison as Fig. 3.2 in the brown-dwarf regime.

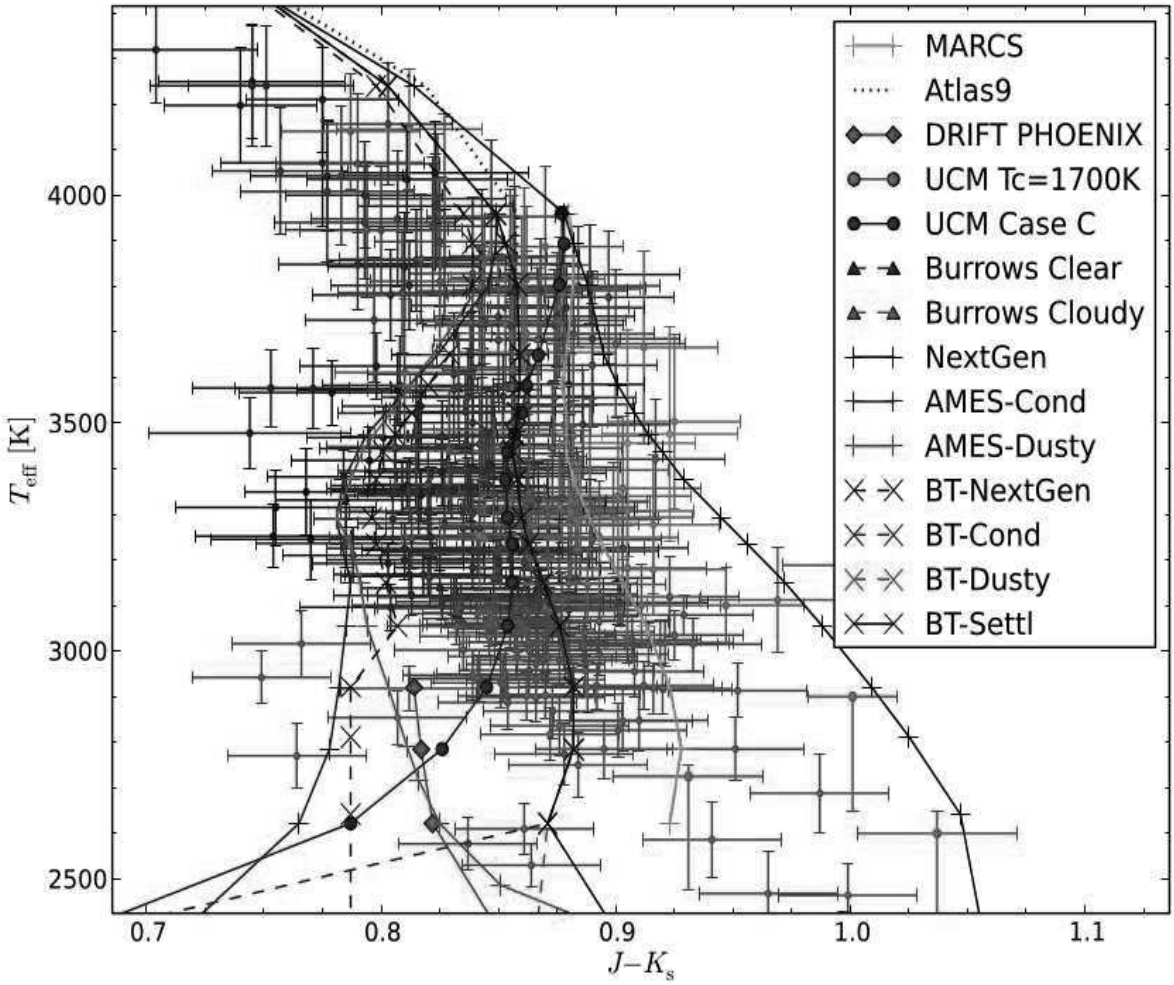

Figure 3.2 – Fig. 2 of the article by Allard et al. (2013). Estimated $T_{\rm eff}$ and metallicity for M dwarfs by Casagrande et al. (2008) on the left, and brown dwarfs by Golimowski et al. (2004) and Vrba et al. (2004) on the right are compared to the NextGen isochrones for 5 Gyrs Baraffe et al. (1998a) using model atmosphere of various co-authors (see Allard et al. 2012a, 2013, for more detail)

.

3.7 Current Model Atmospheres for Low Mass stars

In the following I describe the different model atmospheres for low mass stars which are used in this study.

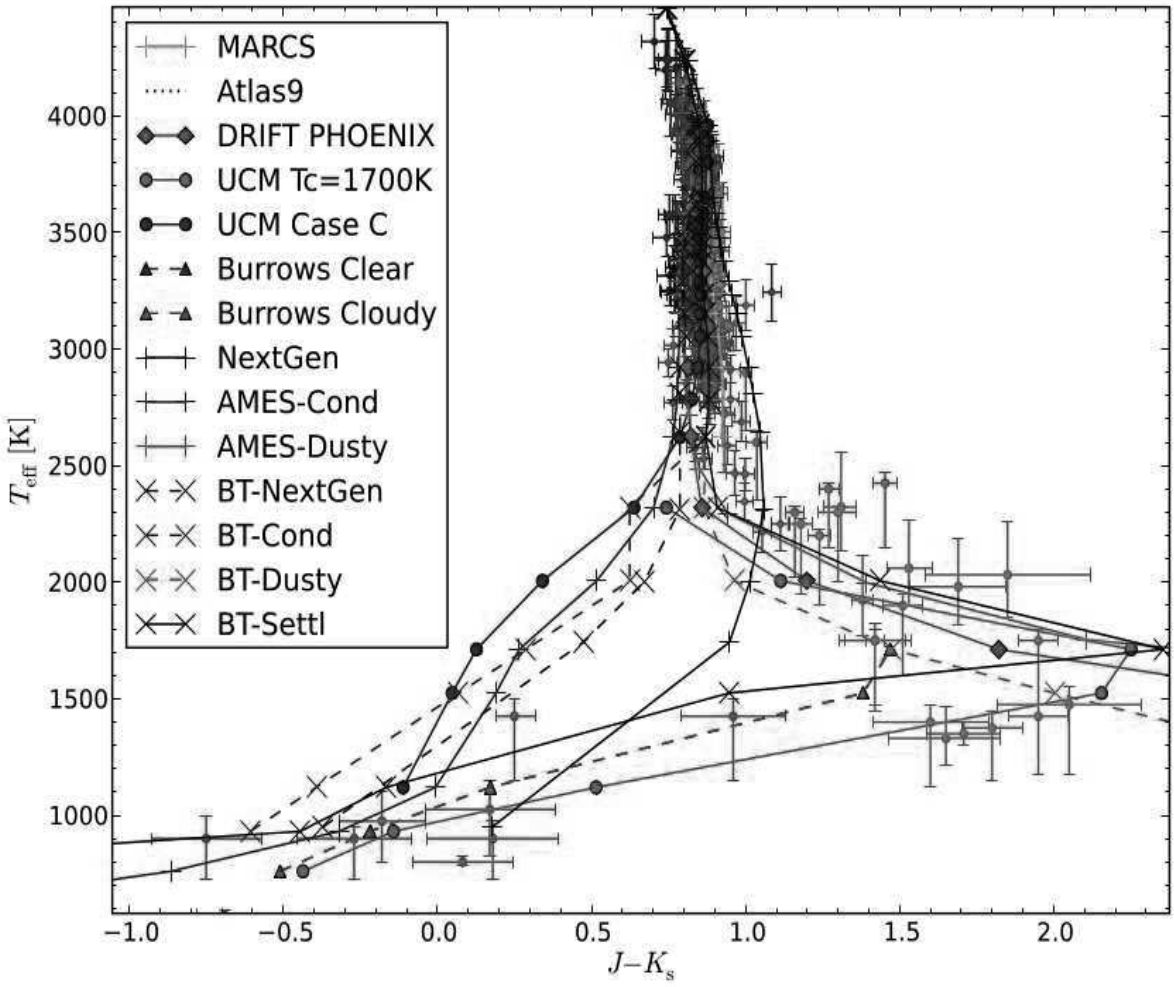

Figure 3.3 – Fig. 3 of the article by Allard et al. (2013). This is the same as Fig. 2 but extends into the brown dwarf regime for an age of 3 Gyrs. The region below 2900 K is dominated by dust formation (see Allard et al. 2012a, 2013, for more details)

3.7.1 BT-Dusty and BT-Settl

The new BT models (Allard et al. 2011) make a great step towards the quantitative understanding of the spectral properties of cool objects and propose for the first time a transition from the stellar to the substellar regime, dealing with their spectroscopic and photometric properties (J, H, and K) and with the effective temperature scale as observationally quantified by Vrba et al. (2004); Golimowski et al. (2004); Casagrande et al. (2008).

The notation BT stands for the Barber and Tennyson so-called BT2 water vapour line list (Barber et al. 2006). The new models are provided in several versions, addressing different

limiting treatment of the cloud physics which prevails in late M dwarf atmospheres (below 2600K). The BT-Dusty and BT-Cond models refer to an equilibrium treatment of dust formation where dust opacities (assuming spherical grains with interstellar grain size distribution) are ignored in the Cond models, as in the earlier AMES-Dusty and AMES-Cond models (Allard et al. 2001). The BT-Dusty and BT-Cond models reproduce the colour properties of the 2001 AMES Dusty and Cond models, with minor differences relating to updated opacities (H_2O, TiO, VO and most of the hydrides, the alkali line profiles, methane, CO_2, and CIA to mention the most important changes) in the 2011 PHOENIX (see below) version. The BT-Settl models on the other hand include the gravitational settling of dust, which was ignored in the Dusty models, and which involves a cloud model. The cloud model used in the BT-Settl models is based on Rossow (1978) and accounts for nucleation, condensation, supersaturation, gravitational settling or sedimentation; it also gives a treatment of advective mixing derived from radiation hydrodynamic simulations (Freytag et al. 2012). The grains are still considered to be spherical but the grain size (a unique or mean value per atmospheric layer) is determined by comparison of the different timescales and thus varies with depth to reach a few times the interstellar values at the cloud base for the effective temperatures discussed in chapter 4. We note that in this context, the BT-Settl models do *not* treat dust in equilibrium with the gas phase, as is done in the case of the Dusty and Cond models. In the new models it is the background gas phase opacities which are adjusted to the depletion of elements from the gas phase caused by grain growth. This allows the BT-Settl models to account for the cooling history of the gas.

These model atmospheres are computed using the `PHOENIX` radiative transfer code (Allard 1990a; Allard & Hauschildt 1995a) assuming hydrostatic equilibrium and treating convection by using the Mixing Length Theory and the values prescribed by the results of radiation hydrodynamics (Ludwig et al. 2002, 2006). Spherically symmetric radiative transfer is treated, with departure from LTE for all elements up to iron, taking micro-turbulence velocities from radiation hydrodynamic simulations (Freytag et al. 2012). The latest solar abundances by Caffau et al. (2011) are used, equilibrium chemistry is assumed for the gas species. A database is used which includes the latest opacities as well as thermochemical data for atomic and molecular transitions and monochromatic dust condensate refractory indexes. Grains are assumed to be spherical and non-porous, and their Rayleigh to Mie reflective and absorptive properties are considered. The treatment of the diffusive properties of grains is based on 2-D radiation hydrodynamic simulations, including forsterite cloud formation in order to account for the feedback effects of cloud formation on the mixing processes in these atmospheres (Freytag et al. 2010).

Compared to previous models by Allard et al. (2001), the current version of the BT-Settl model atmosphere uses the BT2 water vapour line list computed by Barber et al. (2006), and line list for TiO, VO, CaH by Plez (1998), for MgH by Skory et al. (2003a), and Weck et al. (2003), FeH and CrH by Chowdhury et al. (2006) and Dulick et al. (2003), NH_3 by Yurchenko et al. (2011), for CO_2 by Tashkun et al. (2004), and for H_2 Collision Induced Absorption (CIA) by Borysow et al. (2001) and Abel et al. (2011), to mention the most important. It uses the CO line list by Goorvitch & Chackerian (1994a,c). Detailed profiles for the alkali lines are also used (Allard et al. 2007a).

We used extended model grids of the BT-Dusty and BT-Settl synthetic spectra which are

available online (http//phoenix.ens-lyon.fr/simulator). We have used CIFIST2011 version of the BT-Settl models. The synthetic spectra generated by CIFIST2011 models are provided over the entire spectral range of interest at a spectral resolution of 0.001Å. These models have not been used before to study M dwarfs. Rajpurohit et al. (2012b, 2013) have compared first time the recent BT-Settl model atmosphere grid to M dwarfs of the main sequence and L-type brown dwarfs. In chapter 6 we present first time the comparison of BT-Settl model atmosphere with the high resolution spectra of M subdwarfs to explore the metallicity effects.

3.7.2 MARCS

The MARCS code (Gustafsson et al. 2008) assumes hydrostatic equilibrium, Local Thermodynamic Equilibrium (LTE), chemical equilibrium, homogeneous plane-parallel stratification, and the conservation of the total flux (radiative plus convective, with the convective flux being computed using the local mixing length recipe). The radiation field used in generating the model is calculated by assuming absorption from atoms and molecules by opacity sampling at approximately 100 000 wavelength points over the wavelength range 1300 Å–20 μm. For details on the data on absorption by atomic species and by the 15 molecular species, see Gustafsson et al. (2008).

The code used for calculating the synthetic spectra is the BSYN v. 7.12 code which is based on routines from the MARCS code. The atomic line list used in Gustafsson et al. (2008) calculations is compiled using the VALD I database (Kupka & Ryabchikova 1999) and updated accordingly. The molecular line lists include those for CO, SiO, TiO, ZrO, VO, OH, H_2O, CN, C_2, NH, CH, AlH, SiH, CaH (see references in Gustafsson et al. 2008), for MgH (Skory et al. 2003b), for FeH (Dulick et al. 2003) and for CrH (Burrows et al. 2002). Up-to-date dissociation energies and partition functions are used. The synthetic spectra were calculated in plane parallel symmetry. A constant micro-turbulence velocity of 2 km s^{-1} is assumed. Important differences from the BT models are due to the use of different opacities and to the fact that MARCS is a pure gas phase model with no formation of dust. Synthetic spectra are calculated for the wavelength region of $0.50 - 2.53\,\mu$m, with a resolution of $R = 600,000$. Önehag et al. (2012) compared the high-resolution spectra of M dwarfs with the MARCS model. Their studies is restricted to hotter M dwarf ($\geq$ 3000K) as MARCS model doesn't include any dust formation which is the case for cooler M dwarfs below 3000K (Allard et al. 2012a).

3.7.3 DRIFT

The DRIFT-PHOENIX model atmosphere code has been developed by Dehn et al. (2007); Helling et al. (2008a,b); Witte et al. (2009). The code yields a consistent dust cloud structure, with corresponding opacities. It gives an altitude-dependent depletion and redistribution of gas phase abundances. These features have a feedback effect on both the thermodynamical struc-

tures and the radiation field. This feedback means that an iterative solution procedures required. This determination of stationary atmospheric and dust cloud properties and yields the respective synthetic spectra. The dust formation which takes place via the formation of seed particles and their subsequent growth or evaporation is considered. The DRIFT model considers only the seven most important solids (TiO_2, Al_2O_3, Fe, SiO_2, MgO, $MgSiO_3$, Mg_2SiO_4) composed of six different elements. The growth of the grains is governed by the supersaturation ratio of the gas and is triggered by the actual collision rates between grains and gas molecules. It depends on the grain surface. The model thus does not enforce a phase equilibrium requirement. The local number and size of the dust grains, as well as their mean composition throughout the atmosphere, are natural results given by the model. DRIFT models also include the mixing by convection and overshooting by assuming an exponential decrease in the mass exchange frequency in the radiative zone (Woitke & Helling 2004). The model code DRIFT-PHOENIX has been discussed in more detail by Witte et al. (2009). The most important difference from the BT models is the treatment of the dust opacity, which is done manually by adjusting the assumed amount of dust. The synthetic spectra are provided over the entire spectral range of interest at a spectral resolution of 0.05Å. Previous tests of DRIFT-PHOENIX on observations have been presented by Helling et al. (2008b); Schmidt et al. (2008) and Neuhäuser et al. (2009). Witte et al. (2009) used the corresponding synthetic spectra generated from DRIFT-PHOENIX to fit dwarf spectra and gave a more general analysis of dust and atmosphere properties over the parameter space.

Chapter 4

The very low mass multiple system LHS 1070. A testbed for model atmospheres for the lower end of the main sequence

4.1 Introduction

LHS 1070 (other common name GJ 2005) is a low mass multiple system of cool dwarfs discovered by Leinert et al. (1994), with visual magnitude 15. It is a high proper motion star located at a distance of 7.72±0.15 pc from the Sun (Costa et al. 2005). With its velocity component perpendicular to the galactic plane of 36 ± 3 km s^{-1} (Basri & Marcy 1995), it is considered a member of the old disk population with a probable age of several Gyrs (Leinert et al. 2001). Leinert et al. (1994) discovered a pair of cool, very low-mass stars as close companions to LHS 1070, turning the system into a nearby triple system. The spectral type for the A, B, and C component was found to be M5.5-M6, M8.5, and M9-M9.5 (Leinert et al. 2000). A fourth component was suspected very close to the primary by Henry et al. (1999) from HST Fine Guidance observations but this detection is no longer considered real (T. Henry, private communication). Components A, B, and C were the faintest stars within 10 pc from the Sun for which dynamical determinations of mass appeared possible.

The mass range spanned by the components of LHS 1070 makes it a valuable system for understanding the formation of dust in the cool atmospheres and the processes that occur at the star/brown dwarf transition. LHS 1070 is therefore a testbed to validate and define further developments of the atmospheric models at the lower end of the main sequence. One approach to study the physics at the low end of the main sequence is to compare observed spectra with synthetic spectra from various model atmosphere. The determination of the physical parameters (effective temperature, gravity, metallicity, radius) is obtained by spectral synthesis, i.e. χ^2 minimization.

In this chapter we present the spectral analysis of the component A, B and C of LHS 1070. We have determined their physical parameters by comparing the well calibrated HST/NICMOS spectra in the optical and in near-IR with synthetic spectra computed from recent stellar atmosphere models: BT-Dusty and BT-Settl (Allard et al. 2010), MARCS (Gustafsson et al. 2008), and DRIFT (Witte et al. 2009). This work aims to determine the fundamental stellar parameters of LHS 1070 and to test recent model atmospheres.

4.2 Observations and data reduction

We used optical photometry and spectroscopy, described in Leinert et al. (2000) as well as new input in the IR which are described below.

4.2.1 Photometry

The J, H, K, and L' photometry are described for the 3 component in Leggett et al. (1998). M-band photometry was obtained with the UIST instrument on UKIRT on November 9, 2002, as well as N-band photometry with the MAX camera (Robberto & Herbst 1998) on the same telescope on August 27, 1996. The brightnesses of the individual components were then derived from the brightness ratios obtained with NACO (Rousset et al. 2003; Lenzen et al. 2003) for J, H, K on December 12, 2003, for L' and M on December 6, 2001. The MAX observations in N-band yielded separate brightnesses only for component A and the sum B+C of the other two components.

The M band data were obtained in the Mauna Kea Observatory near-IR System ($\lambda_{\rm central}$ = 4.7μm, 50%-width= 0.23μm) in service mode. Aperture photometry was applied to the pipeline-reduced data. The N band photometry used a standard filter ($\lambda_{\rm central}$ = 10.47μm, 5%-width = 4.65μm). After the standard processing steps (bad pixel correction, combination of individual chop cycles after shift-and-add) aperture photometry a was performed. The absolute calibration at 10.4 μm relied on the HR 6464 spectrophotometric standard model, produced by P. Hammersley using the procedure described in Hammersley et al. (1998), and made available on the ISO web page for ISO standards. HR 6464 has the same spectral type M0III as the standard HR 400 actually observed, and the flux ratio of the two was determined from their fluxes in the IRAS 12 μm band. Strictly speaking, the result is a narrow-band (0.25 μm) brightness at 10.4 μm under the assumption of an M0III type spectrum. The spectral slopes in this wavelength region are smooth and all are representing Rayleigh-Jeans tail emission. Uncertainties resulting from the difference in spectral type between M0III and our object therefore are not important. To be conservative, errors of ± 5 mJy, ± 4 mJy, and ± 3mJy are taken for the fluxes of the combined system, of component A, and the sum of components B and C, respectively.
The NACO observations were used in determining the relative brightnesses of the three components of LHS 1070, because of the superior spatial resolution of this instrument. After standard

reduction (flat fielding, bad pixel correction), aperture photometry was applied. The NACO bandpasses closely match the MKO near-IR system for the J, H, K, L' bands. The main difference is in the M band (4.8 μm for NACO versus 4.7 μm at Mauna Kea, 20% width of 0.64 μm for NACO versus 50% width of 0.23 μm at Mauna Kea). In this wavelength range, the slopes of the component spectra are very similar. Therefore the NACO-measured brightness ratios were applied to extract the component brightnesses from the MKO near-IR based total brightnesses.

LHS 1070 was observed with ISOCAM (Cesarsky et al. 1996) on the ISO satellite in the LW2 (6.7 μm) and LW3 (14.3 μm) filters on November 28, 1996 (PI H. Zinnecker). Near-IR narrow and medium-band photometry from 0.90 μm to 2.15 μm was obtained with the NIC1 and NIC2 cameras of the HST NICMOS instrument on Jan. 2, 1998. On each frame the system was clearly resolved, and it was possible to obtain separate photometric measurements for the three stars. Before performing aperture photometry for a given star, the images of the other two objects was removed by subtracting a scaled PSF template, constructed from component A and shifted to the known coordinates of the stars. An aperture correction, taken from the NICMOS Data Handbook, was applied, and photometric calibration was performed via multiplying by a conversion factor between the counts and F_ν as stated in the Handbook. The results are given in Table 4.1.

4.2.2 Spectroscopic observations

Near-IR spectra of the individual components of LHS 1070 were taken with grisms G096, G141 and G206 and the NIC3 camera of the HST NICMOS instrument on January 2, 1998 for the J, H, and K bands. In a first step, four spectra were removed for each grism the short wavelength and long wavelength ends. For grism G096 this left the range of 0.80-1.085 μm or 0.8-1.15 μm, depending on the local noise level. Similarly, G141 covered the range of 1.10-1.60 μm or 1.10-1.85 μm. G206 ranged from 1.65 μm to 2.45 μm. For each wavelength pixel, all spectra covering that wavelength were averaged using a weighted average, where the weights came from the formal uncertainties of the spectra (typically from 2% to 5%). The reduction was based on the NICMOSlook IDL-based data reduction package. For the extraction of the spectra, the 'no weighting' option was used. The result for the A component was slightly scaled (by a few percent) to fit the NICMOS photometry. The extraction procedure also gave the combined spectrum of components B and C (separated only 0.4" on the detector), which was decomposed into the spectra of the individual components on basis of the brightness ratio as a function of wavelength as determined from the narrow- and medium band photometry. The spectral resolution of the NICMOS spectra is $R = \lambda/\Delta\lambda = 200$.

Higher resolution spectra with $R = 400, 1500$, and 1400 in the J, H, and K bands, respectively, were taken with the VLT NACO instrument (Rousset et al. 2003; Lenzen et al. 2003) on telescope UT4 of the VLT for the individual components of LHS 1070. The camera/grism/filter settings were S27/Grism4/J, S54/Grism3/H, and S27/Grism3/K, respectively. The slit width

was 86 milli-arcsec in all three bands. After subtracting the sky from the raw data, a flat normalized along the dispersion direction was applied. The spectra were then traced and extracted. Finally, the individual exposures were averaged. This procedure was also applied to the telluric standards. All telluric standards are of spectral type G2V, which allows a proper modeling of their intrinsic spectrum with that of the Sun. The Solar spectrum was constructed using the data and scripts provided by Maiolino et al. (1996). Wavelength calibration was obtained by arc lamp exposures. The additional effort to guarantee the absolute flux calibration was not taken, so only the relative shape of the spectrum was determined in each band. For each component, a scaling factor for each band was applied to bring the spectra to the absolute level as resulting from the NICMOS observations. The errors, taken as the formal uncertainties of the averaging process, typically range from 5-10%. The number of pixels per resolution element in the J, H, and K band is about 3, 1.5, and 3. Because of the missing independent absolute calibration, the NACO spectra are used primarily for the study of spectral features. However, comparison with the NICMOS spectra, like in Figure 4.1, gives confidence also in their spectral shape.

Spectra for the system from 2.5 μm to 11.7 μm were obtained with the ISOPHOT-S spectrometer on board the ISO satellite on November 23, 1996 (PI: T. Tsuji) with an exposure time of 4096 s. ISOPHOT-S was the spectroscopic sub-instrument of ISOPHOT (Lemke et al. 1996). It had an entrance aperture of 24"x24", covering simultaneously the 2.5 to 4.9 and 5.9 to 11.7μm ranges. The spectral resolution of both channels ranged between 65 and 130. The ISOPHOT-S observations were processed using the `Phot Interactive Analysis (PIA) V10.0` (Gabriel et al. 1997) following the standard data reduction scheme. The measurements were further reduced following our self-developed processing scheme (Kóspál et al. submitted), correcting for the slight off-centre positioning of the source.

4.2.3 Spectroscopic features

Figure 4.2 shows the optical spectra of all the three components, with expected atomic and molecular features in the optical range between 5000 to 8500 Å. The most important lines are molecular bands of TiO, CaH and VO, and atomic lines like CaII, NaI and KI. The TiO bands get weaker toward lower temperature, from component A to C, due to condensation into dust species. The hydride bands such as CaH at 6380 Å and 6880 Å,decreases in strength with decreasing temperature. The KI doublet at 7665 Å and 7699 Å is very strong and is useful for gravity determination. The NaI doublet at 8183 Å and 8195 Å is strong in all the components, whereas CaI at 6103 Å $\approx$ is weak at all temperatures.

Figure 4.3 and 4.4 shows the near-IR spectra obtained with NICMOS on HST for all the three component as well as the thermal infrared spectrum of the unresolved system A+B+C taken from ISOPHOT on ISO . Photometric results are superimposed on these spectra.

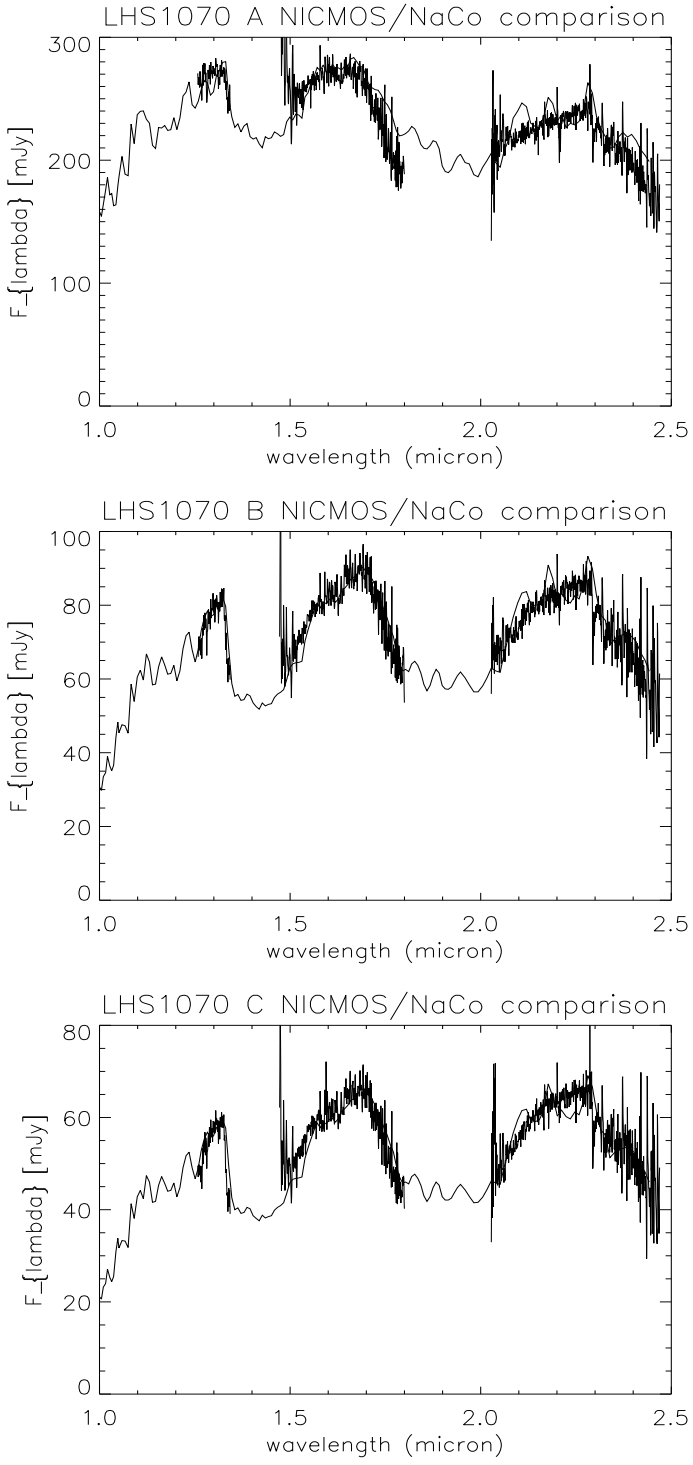

Figure 4.1 – Comparison between NICMOS and NACO spectra of three different components.

Figure 4.5 to 4.7 shows the NACO spectra obtained at the VLT of the three individual components in the J, H, and K band for components A, B, and C. The main expected features are also indicated. The Paschen Beta and CaI lines can be seen in the J-band spectra with

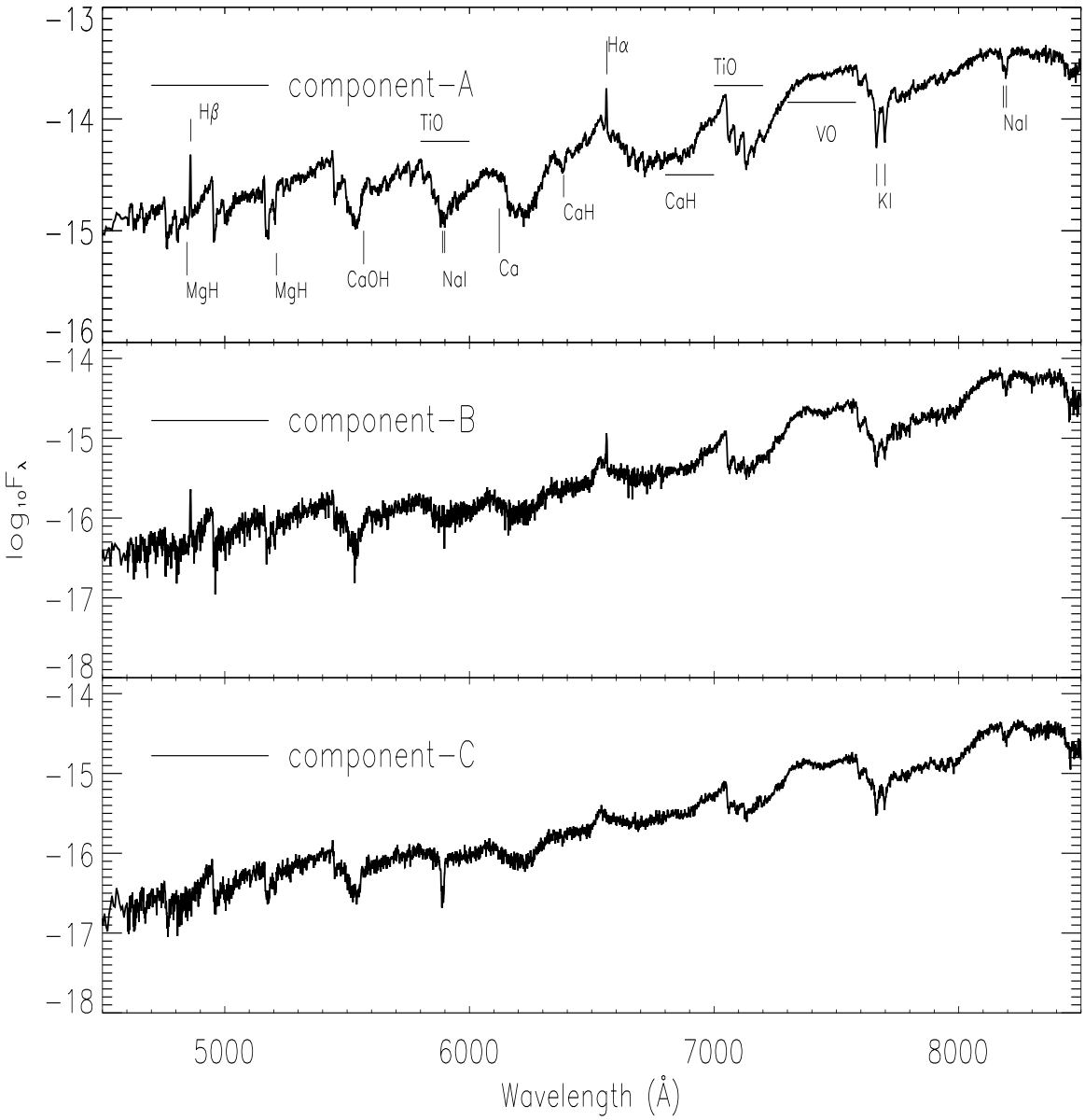

Figure 4.2 – Optical Spectra of all the components of LHS 1070 system obtained with the Faint Object Spectrograph (FOS) on HST. The atomic and molecular features visible in all three components are shown in the upper panel.

"equivalent widths" of 2-2.5 Å and 1.5-2 Å, respectively. The H-band spectra contain many relatively weak absorption features, which defy definite identifications, with possible exception

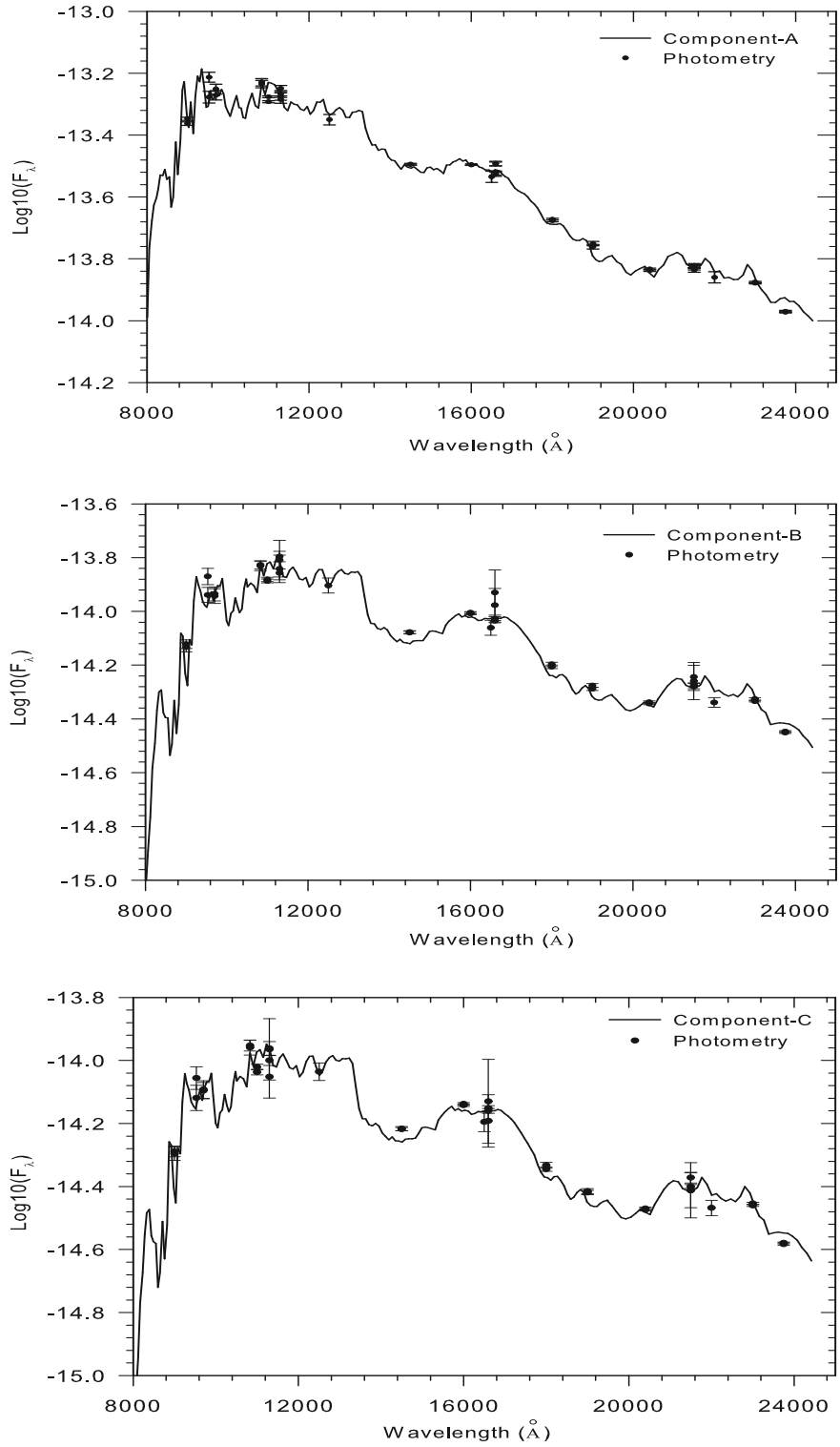

Figure 4.3 – Near-IR spectra (solid line) and photometry (solid circles) obtained with NICMOS on HST for components A (upper), B (middle), and C (bottom).

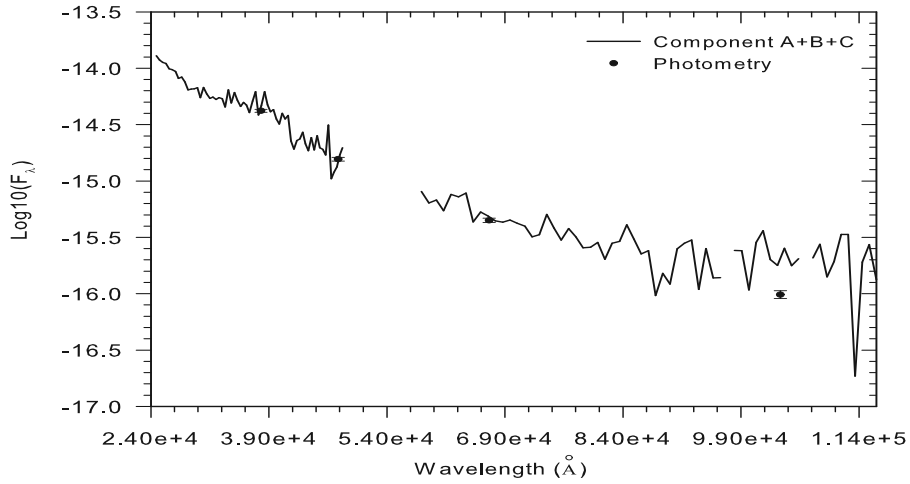

Figure 4.4 – The ISOPHOT thermal infrared spectra of the unresolved system.

of Mg (1.711 μm), OH (1.689 μm), and Al (1.675 μm). H_2O bands define the shape of the J and H band peaks. Water absorption is most obvious in the J-band at 1.33 μm and strengthens through the later types: the flux ratio between the peak and the minimum of the absorption band increases from 1.09 ± 0.01 for component A to 1.30± 0.01 and 1.39 ± 0.01 for the cooler components. The K-band spectra of the three components show strong CO bands and more or less pronounced atomic features. The NaI lines weaken from the hotter component A to the cooler components B and C as dust forms.

4.3 Physical Parameters Determination

The first analysis of LHS 1070 by spectral synthesis was made by Leinert et al. (1998) using the FOS spectra and the pure gas phase NextGen model atmospheres (Allard et al. 1997; Hauschildt et al. 1999). But the quality of the fits, even for the A component was disappointing, especially below 0.72 μm, and the $T_{\rm eff}$ of the B and C components were strongly overestimated (2700 K) mainly due to the absence of dust formation in the model. Leinert et al. (2000) have therefore used the AMES-Dusty models (Allard et al. 2001) to re-analyze the LHS 1070 system. However if the quality of the fits and precision of the $T_{\rm eff}$ for the B and C components were clearly improved, this was still clearly not the case of the M dwarf primary. The stellar parameters obtained with the assumption of a distance of 8.8 pc are summarized:

- Component A: $T_{\rm eff}$ =2950 K, log g=5.3±0.2, [M/H]=0.0
- Component B: $T_{\rm eff}$ =2400 K, log g=5.5±0.5, [M/H]=0.0
- Component C: $T_{\rm eff}$ =2300 K, log g=5.5±0.5, [M/H]=0.0

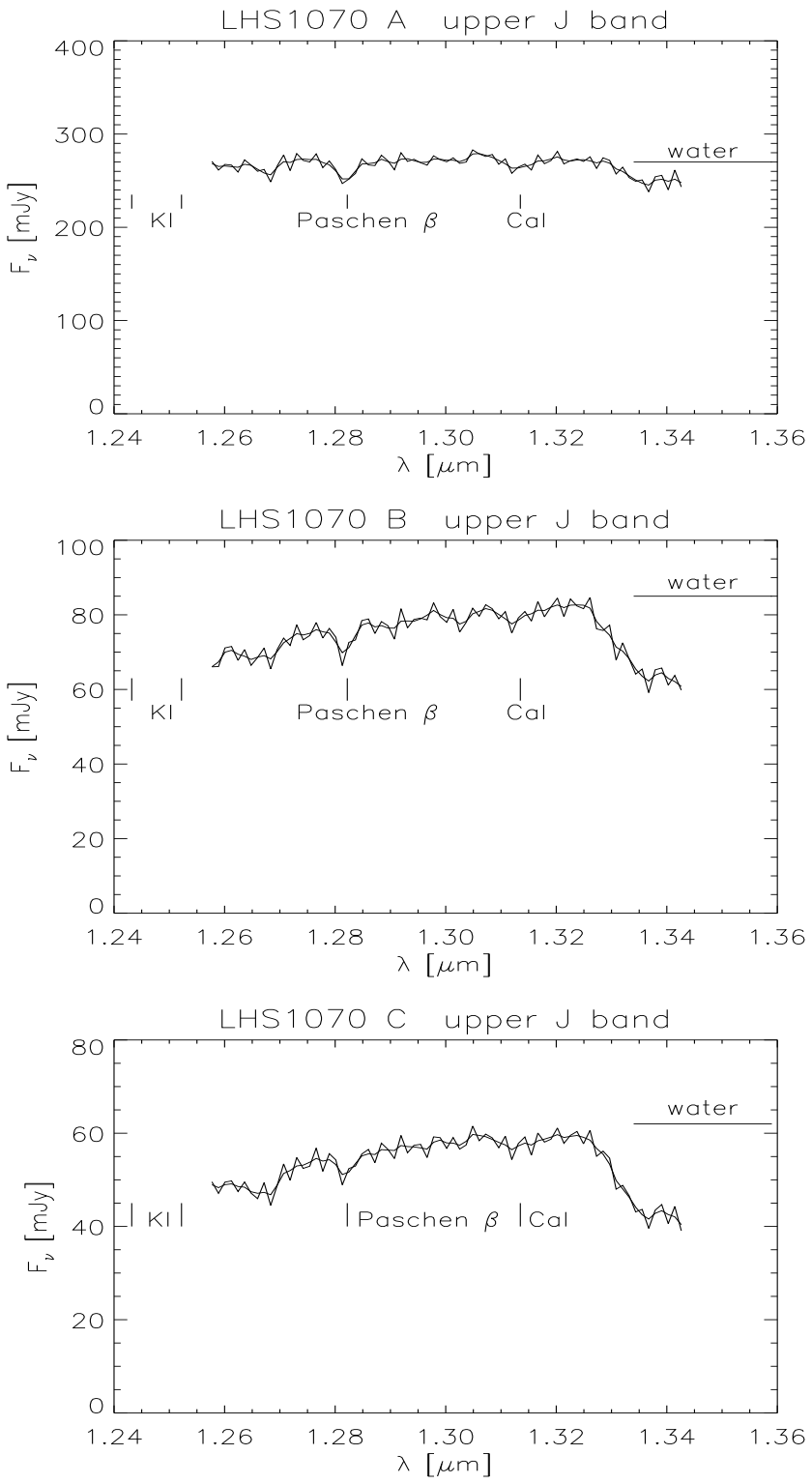

Figure 4.5 – VLT (NACO) spectra of all the component in J band with atomic and molecular lines indicated.

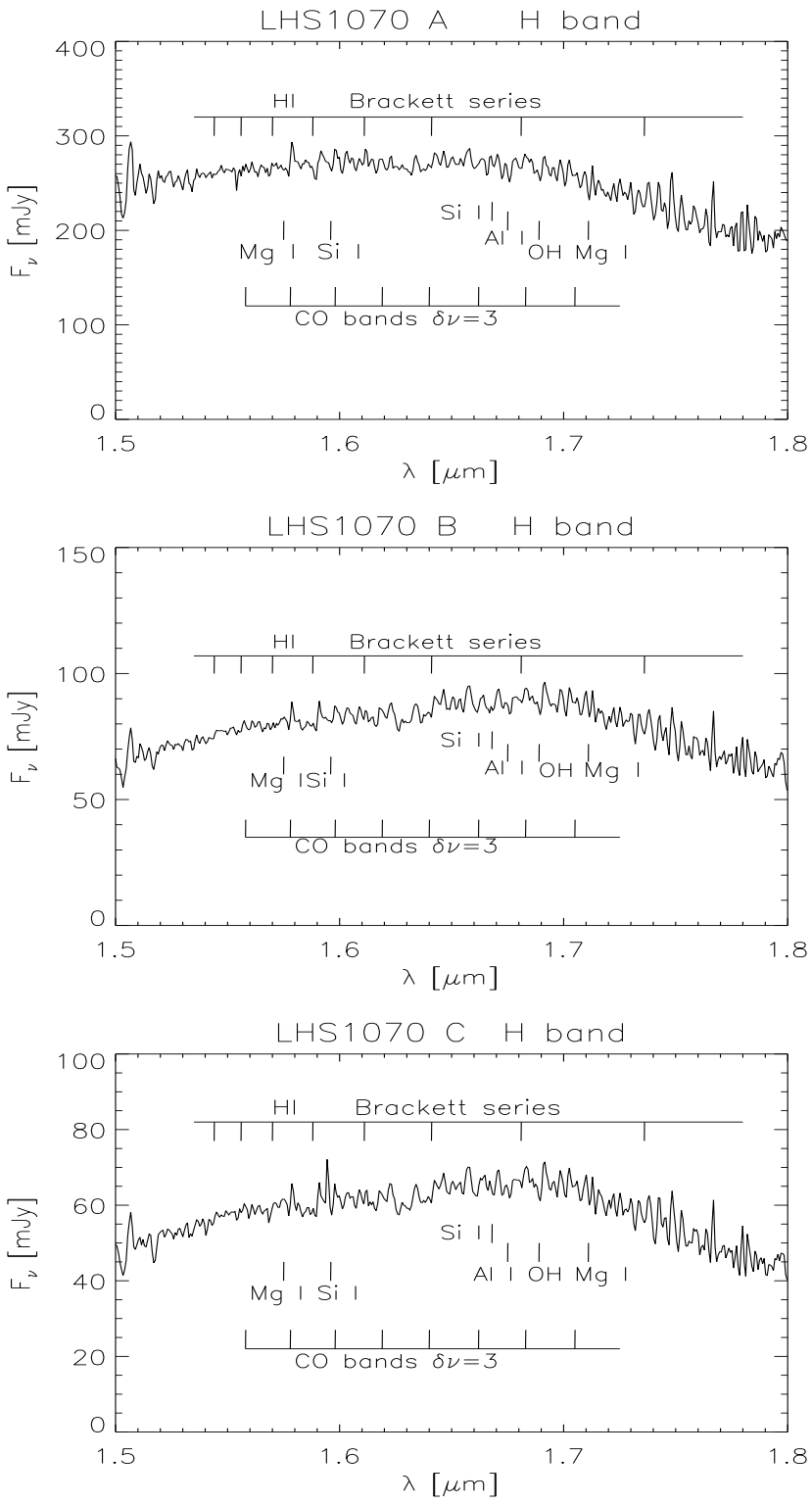

Figure 4.6 – VLT (NACO) spectra of all the component in H band with atomic and molecular lines indicated.

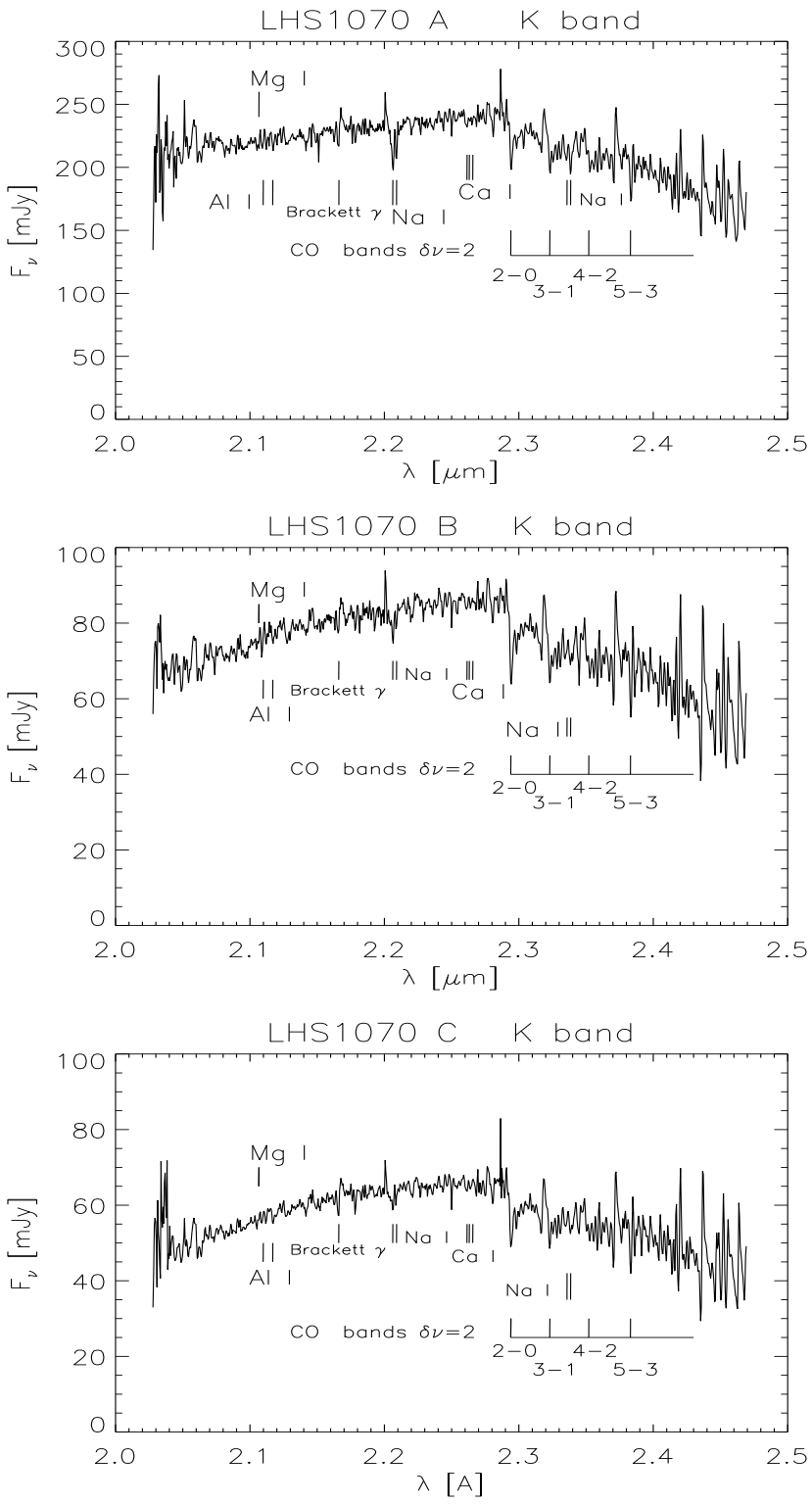

Figure 4.7 – VLT (NACO) spectra of all the component in K band with atomic and molecular lines indicated.

In the following, we derive the stellar parameters using more recent atmosphere models and spectroscopic informations covering both the optical and IR ranges. Metallicity and gravity are determined from peculiar spectral features, whereas effective temperature and radius are constrained from the overall shape of the spectra, following the different steps : (i) a first $\chi 2$ minimization is performed on the overall spectra considering effective temperature, radius, metallicity, and gravity as free parameters. It gives a first guess for the parameter space of each component; (ii) we looked for peculiar spectral features that are mainly sensitive to metallicity (see Sect.4.3.3) or gravity (see Sect. 4.3.4) to refine these two parameters; (iii) we fixed these parameters to perform another $\chi 2$ minimization and derive effective temperature and radius (see Sect. 4.3.5.). At each step we checked that the resulting value is not sensitive to changes on the value of the other parameters. Age is estimated from kinematics and rotation. Before entering the details of our study, we also summarize our results in Table 4.2. Note that these values have been obtained by assuming a revised distance of 7.72 pc (Costa et al. 2005) whereas Leinert et al. (2000) used the higher value of 8.8 pc. For the current study we have used three different model atmosphere as explained in chapter 3.

4.3.1 Atmosphere models

We explored these different model atmosphere grids with parameter described as follows:

BT-Dusty and BT-Settl grid:

- $T_{\rm eff}$ from 2000 K to 3000 K with 100 K step, as expected for mid-M to L dwarfs,
- log g = 5.0 and 5.5 dex ,
- [Fe/H] = -1.0, -0.5, 0, +0.3, and +0.5 dex.

MARCS grid :

- $T_{\rm eff}$ from 2550 K to 3100 K with 100 K step (lower temperatures are not available),
- log g = 5.0 and 5.5 dex,
- [M/H] from -0.5 to 0.25 dex with 0.25 dex step.

DRIFT grid :

- $T_{\rm eff}$ from 2200 K to 3100 K with 100 K step,
- log g = 5.0 and 5.5 dex,
- [M/H] from -0.5 to 0.5 with 0.5 dex step.

4.3.2 Spectral Type

A well-defined spectral classification for the M dwarfs helps in the calibration of the temperature of the late type stars and for the definition of the end of the main sequence on the HR diagram. We have derived spectral indices and spectral types for all three components. For the early M-dwarf, i.e. the primary, we used the classification scheme based on the TiO and CaH band-strengths, as defined by Reid et al. (1995). For the late M-dwarfs, we also used the PC_3 index defined by Lépine et al. (2003a); Hawley et al. (2002); Martín et al. (1999). We have computed the spectral index H_2O-K in the near-IR K-band defined by Covey et al. (2010) and used the spectral-type vs. index relation from Rojas-Ayala et al. (2010). The spectral indices and corresponding spectral types are given in Table 4.3. The obtained spectral classification for components B and C is one subclass higher as compared to Leinert et al. (2000). The spectral types obtained in the K-band differs from the optical indices by up to two sub-classes showing inconsistency on the spectral type versus spectral index relations defined from the optical and near-IR spectra. Here we adopt the spectral type obtained from optical spectral indices.

4.3.3 Metallicity

In order to estimate the metallicity of the system, we looked for special features in the spectra that are mainly sensitive to the metallicity. The main indicator of metallicity is the VO absorption band at 7300-7600 Å. It is well reproduced at solar metallicity for all components, and shown in fig. 4.8 for the primary with the BT-Settl model. We checked that the same metallicity is found when changing the other parameters. This solar metallicity can also be inferred from the NaI, CaI, and H_2O features in the K-band of the primary using the calibration determined by Rojas-Ayala et al. (2010). In the following, we adopt this [M/H] = 0 dex value.

4.3.4 Gravity

The surface gravity can be estimated by analyzing the width of atomic lines such as the K I and Na I D doublets, as well as the relative strength of metal hydrides bands such as those of CaH. The K I doublet at 7665 Å and 7699 Å is a particular useful gravity discriminant for M stars. Figure 4.9 shows the gravity effects on the strength and pressure broadening of the K I lines as modeled by the PHOENIX BT-atmosphere models. The overall line strength (central depth and equivalent width) increases with gravity as the decreasing ionization ratio due to the higher electron pressure leaves more neutral potassium in the deeper atmosphere. The width of the damping wings in addition increases due to the stronger pressure broadening, mainly by H_2 , He and H I collisions. Figure 4.10 shows the determination of gravity for the component A from the K I doublet using the BT-Settl, MARCS, and DRIFT models. The determined log g values are given in Table 4.2. The best agreement is obtained with log g = 5.0 dex for all the atmospheric models. This value is confirmed by the CaH molecular bands (Fig. 4.11). We checked that the

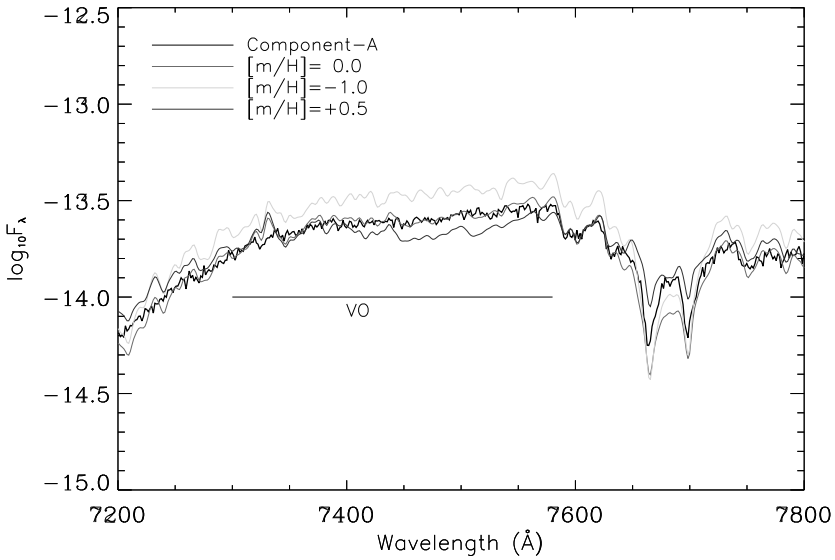

Figure 4.8 – The VO band observed in the component A (red) are compared to the BT-Settl model at 2900 K, log g= 5.5, $R_{\odot}$ = 0.134 at different metallicity (different colors)

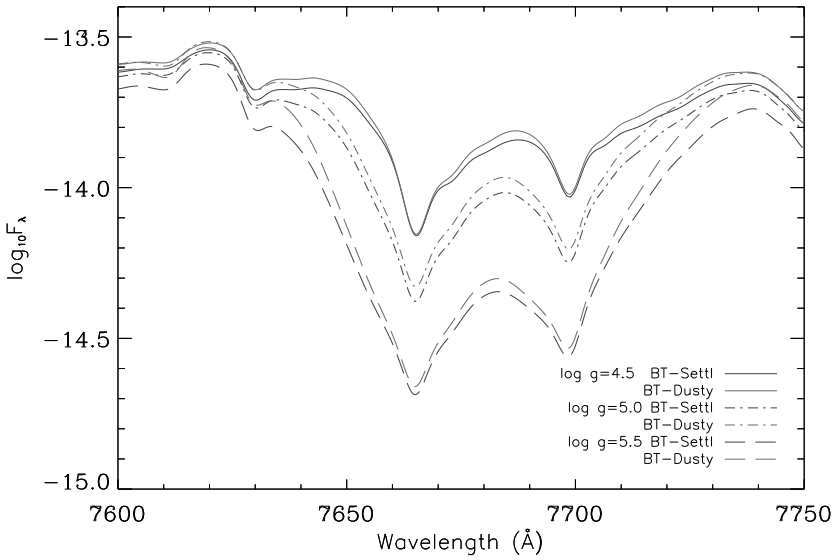

Figure 4.9 – BT-Settl and BT-Dusty models for an effective temperature of 2900 K and varying log g. The effect of gravity and the pressure broadening of the KI doublet is clearly visible. The details of the dust treatment only cause negligible differences at this $T_{\rm eff}$

same metallicity is found when changing the other parameters. For comparison, the gravities inferred from the masses found from the orbits of the system (Seifahrt et al. 2008) are also listed, which are also in good agreement with the values found by fitting.

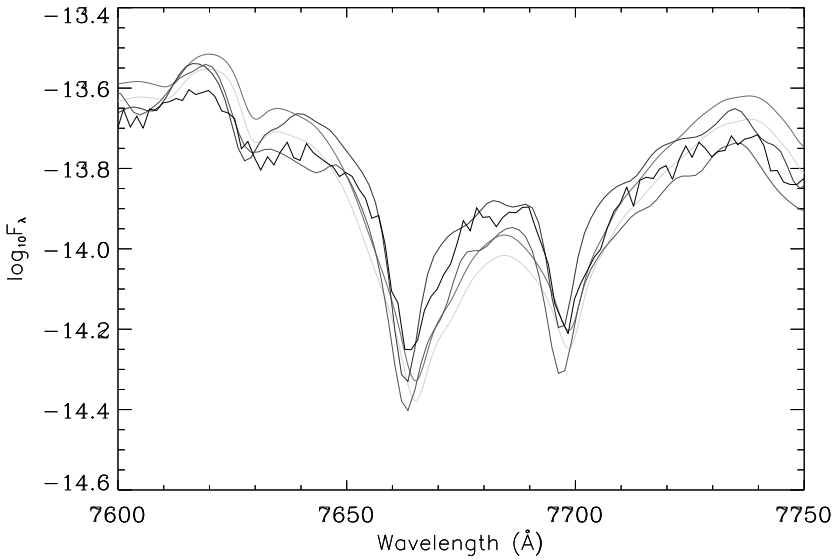

Figure 4.10 – K I doublet as observed for the primary (black) compared to the BT-Dusty (red), BT-Settl (green), DRIFT (blue), and MARCS (brown) models with log g = 5.0.

4.3.5 Effective Temperature and Radius

We performed a second $\chi 2$ minimization by adopting the metallicity and gravity derived in Sects. 4.3.3 and 4.3.4 and refined the effective temperature and the radius by comparing the overall shape of the observed and synthetic spectra. As opposed to the studies mentioned previously in which the best fit was found by trial and error, in this study we derive the effective temperature and radius by performing a $\chi 2$ minimization technique. For this purpose, our approach was to first convolve the synthetic spectrum with a Gaussian kernel using equation 7.1 at the observed resolution and then interpolate the outcome with the observation. For each of the observed spectra we have calculated the $\chi 2$ using the equation 7.2 explained in Apendix. We have excluded the spectral region below 4500 Å due to the low signal-to-noise ratio of the observed spectra. The number of data points used for the $\chi 2$ computation is thus 1487 in the optical and 204 in the near-IR. In a second step, a $\chi 2$ map has been obtained for each component in the optical and in the near-IR as a function of temperature and radius. Such a map is shown in Fig. 4.12 for the primary using the BT-Dusty model. The minimum $\chi 2$ value is given on the left part of the color bar. The parameter space which gives an acceptable solution around the minimum $\chi 2$ valley is within the white contour, defined by visual inspection. We have identified on the contour maps the possible solutions in the optical and near-IR. The adopted values of effective temperature and radius are the common intersection between the solutions found in the optical and near-IR $\chi 2$ map. The $\chi 2$ value at this significance level is indicated along the white contour. Error bars are derived from this contour.

The solutions were finally inspected by comparing it with the observed spectra. The same

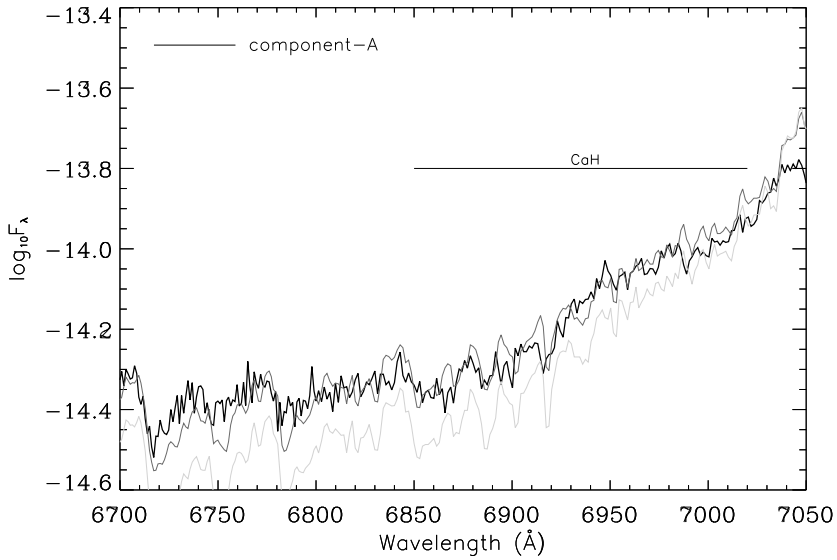

Figure 4.11 – CaH molecular band as observed for the primary (black) compared to the BT-Settl model at 2900 K, log g= 5.0 (red) and log g=5.5 (green), $R_{\odot}$ = 0.134 at solar metallicity.

procedure has been used with BT-Settl, MARCS and DRIFT model grids. Differences of 100 K to 200 K in the $T_{\rm eff}$ determination (see Table 4.2) are found for the B and C components depending on the model used, whereas all models agree on the effective temperature of the primary.

4.3.6 Age and mass

With its high velocity component of W = 43 kms^{-1} perpendicular to the galactic plane based on Basri & Marcy (1995), LHS1070 has been considered as part of the old disk population with an age of several Gyrs. Reiners et al. (2007b) refined this estimate to about 1 Gyr based on measured rotation velocities of its components using a modified Skumanich braking law (Skumanich 1972). They do not exclude however that the braking law may also have to be changed in its absolute time scale, which could increase this estimate.

By an orbital fit, Leinert et al. (2001) have computed the combined mass of the components B and C and showed that their mass is very close to the hydrogen burning minimum mass, in good agreement with the masses of 0.080 to 0.083 M and 0.079 to 0.080 M derived by Leinert et al. (2000) from theoretical mass-luminosity relations (Baraffe et al. 1998a; Chabrier et al. 2000). Seifahrt et al. (2008) constrained the combined mass of B and C to $M_B + M_C = 0.157 \pm 0.009$ M which is higher than Leinert et al. (2001) because of the refined distance by Costa et al. (2005). Recently, an improved fit for the orbit of LHS 1070 B and C around each other,

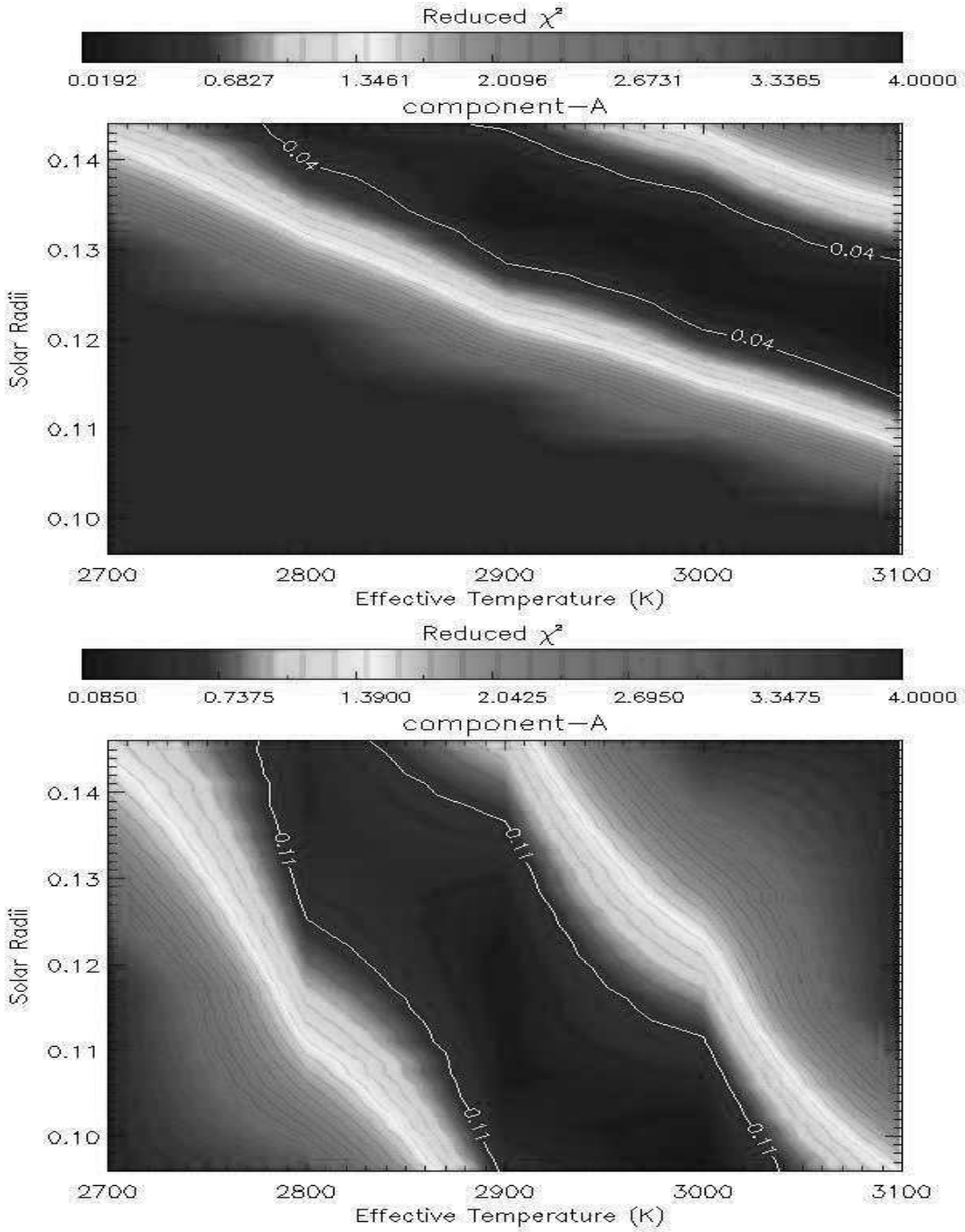

Figure 4.12 – Top: χ^2 map computed for component A using the optical spectrum and the BT-Settl model. All values inside the white contour also give an acceptable fit (checked by eye). Bottom: same using the IR spectrum. We consider both χ^2 maps to define the best model that satisfies both optical and IR observations: $T_{\rm eff}$ =2900 K and r = 0.134 $R_\odot$.

and an estimate for the orbit of B and C around A have been performed. The masses of the three components are found to be M_A = 0.13 to 0.16 $M_\odot$, M_B = 0.077 ± 0.005 $M_\odot$, and M_C = 0.071 ± 0.004 $M_\odot$ (Köhler et al. 2012). Here, the values for the primary are uncertain, because the wide

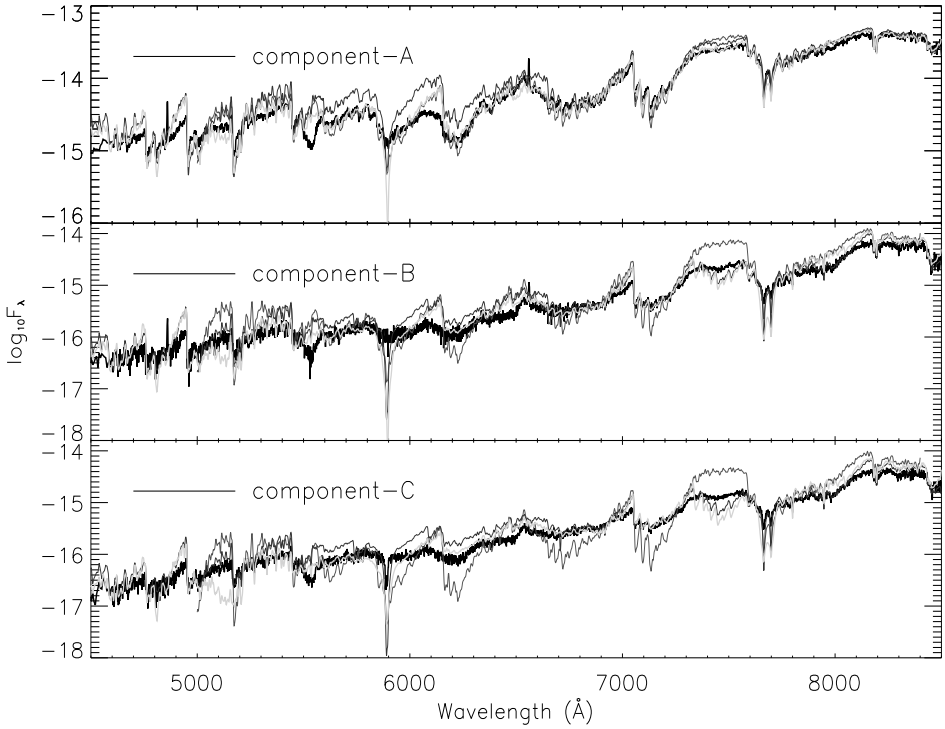

Figure 4.13 – Optical spectra of all three components. Black: observed spectra. Green: best fit BT-Settl model. Blue: best fit DRIFT model. Brown: best fit MARCS model. The parameters that give the best fit are given in Table 4.2

orbit of this triple system has not yet been determined with sufficient accuracy. Finally, Seifahrt et al. (2008) have not measured individual masses for the B and C components, but using the mass ratio $M_C / M_B = 0.923$ from Köhler et al. (2012), their masses for A, B, C become 0.115 ± 0.01, 0.082 ± 0.01 and 0.075 ±0.01 M .

The interpolations of the NextGen (Baraffe et al. 1998a) isochrone for the primary, and of the AMES-Dusty (Chabrier et al. 2000) isochrone for the B and C components, assuming an age of 1 Gyr for the dynamical masses of Seifahrt et al. (2008) are shown in Table 4.2. For masses above the hydrogen burning limit these values do not change much for larger ages, since in the stellar regime small evolution effects are seen after the age of 1 Gyr. No evolution models have yet been calculated using the BT-Settl models. However, only negligible changes are expected with the revision of the evolution calculations. Such revision of the interior and evolution models is currently being prepared (I. Baraffe,Exceter, priv. comm.).

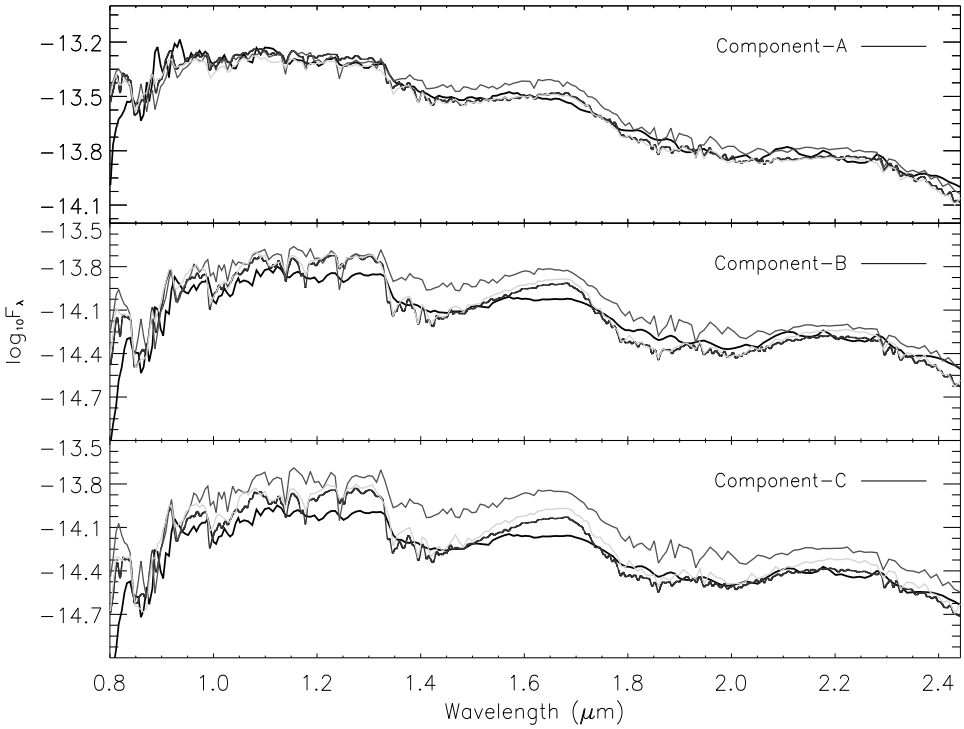

Figure 4.14 – Same as Fig. 4.13 in the IR.

4.4 Results

Figures 4.13 and 4.14 show the best fit model superimposed to the observed optical (FOS) and near-IR (NICMOS) spectra for all the three components using the BT-Settl, BT-Dusty, MARCS, and DRIFT models. Note that the observed NICMOS spectra of all three components plunge down away from the model predictions below 0.85 μm (see Fig. 4.14), whereas the observed FOS spectra are correctly represented by the models in the same wavelength range (see Fig. 4.13). This deviation is due to difficulties with the NICMOS data at the very edge of the wavelength range.

The FOS spectral distribution is better reproduced by the models for the primary than for the cooler components B and C. The revised opacities and oxygen abundance (among other elements) used in the current BT-Settl models allow a significant improvement compared to the AMES-Dusty and NextGen models used in previous analysis (Leinert et al. 1998, 2000). The slope of the spectra is now reproduced over the complete FOS spectral distribution, and the strength of molecular bands is reproduced on average quite well. However some problems remain which are probably due to uncertain and missing opacity sources. Hence, the MgH feature

at around 5200 Å is too strong in all the models while the CaOH band at 5500 Å is missing in all models. The NaI doublet at around 5900 Å is far too strong in the models as well as the CaH band at 7000 Å. Largest discrepancies are found around 6000-6400 Å for all models. The TiO bands around 7055 Å as well as the CaH band around 6900 Å are too strong in all the models. The VO band around 7334 Å is also visible and is quite well matched by the BT-Settl model. The BT-Settl models also differ from the DRIFT models by the strength of atomic lines which are deeper in the DRIFT models.

In the near-IR NICMOS range, the BT-Settl models fit slightly better the primary than the DRIFT models. The MARCS model overestimates the flux over most of the spectral range above 1.3 μm while the DRIFT model shows a slightly different shape of the H band peak which is shared by the BT-Settl models in the case of the B and C components. But all the models appear over luminous in the J and H bands in the case of the B and C components for the selected radius and effective temperature. This is also apparent in fig. 4.15 to 4.20 which shows the comparison of high resolution near-IR spectra (NACO) with the best fit of all the four models. The change in the NaI and CaI strength as the temperature decreases (K-band) is quite well reproduced by the BT-Settl, BT-Dusty and DRIFT models.

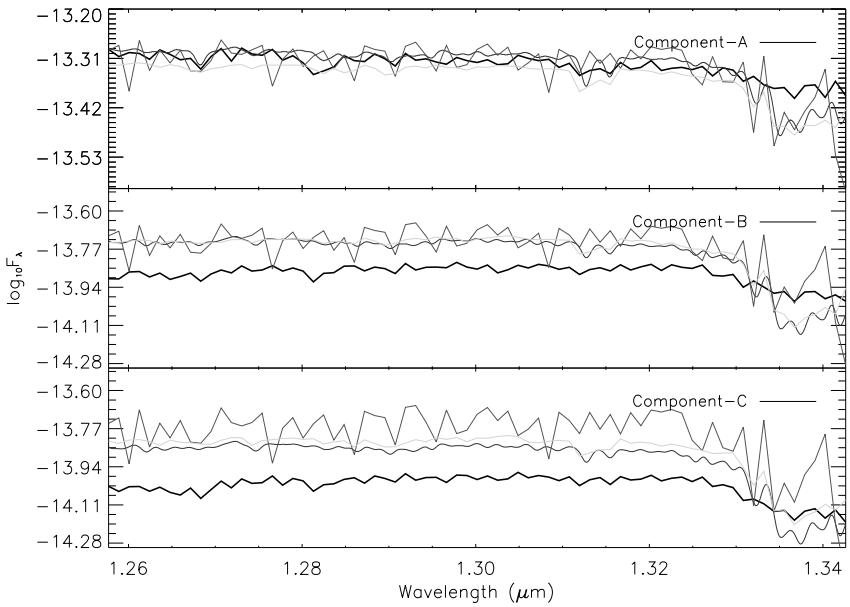

Figure 4.15 – Black: J band NACO spectra of all three components. Comparison with model predictions. Green: best fit BT-Settl model. Red: best fit BT-Dusty model. Blue: best fit DRIFT model. Brown: best fit MARCS model

As an additional check on the effective temperature determination, we also compared the

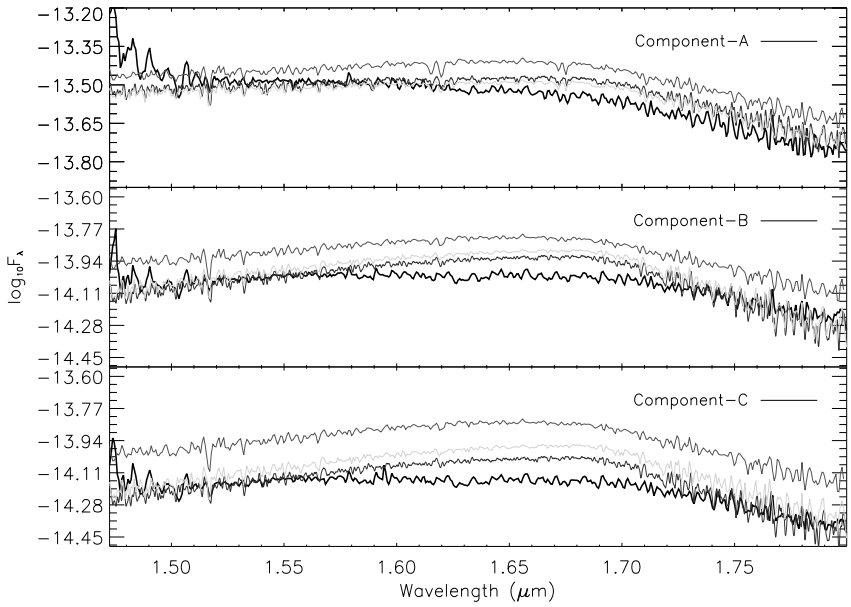

Figure 4.16 – Same as fig 4.15 for H band

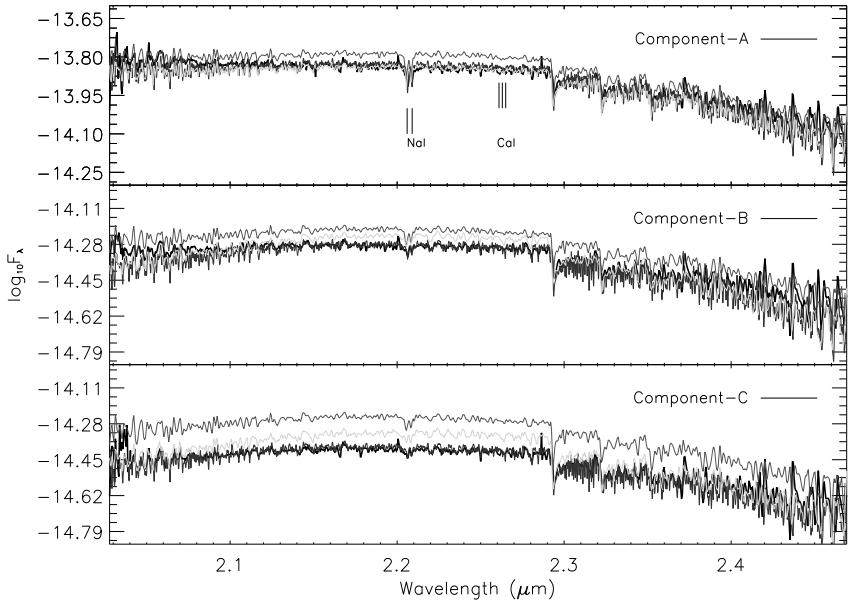

Figure 4.17 – Same as fig 4.15 for K band

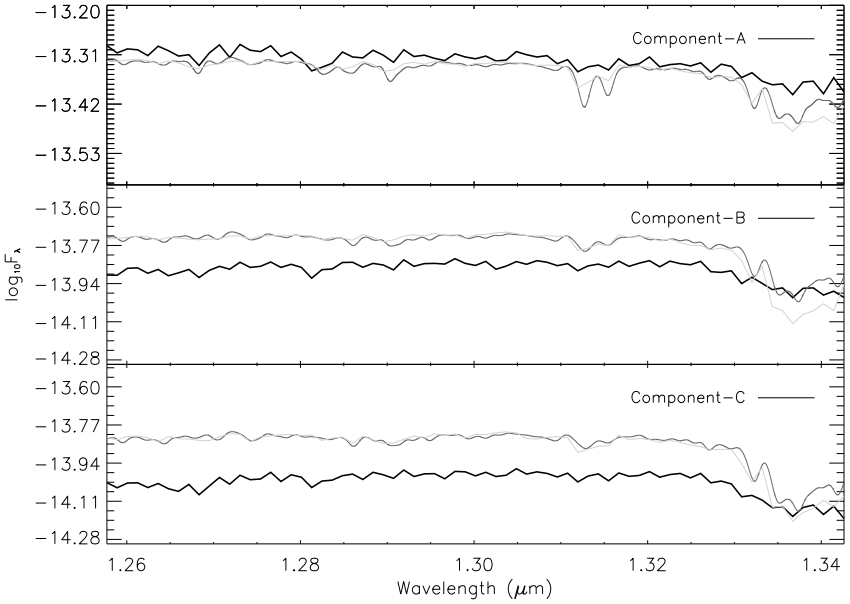

Figure 4.18 – The comparison of the BT-Dusty (red) and BT-Settl (green) models together with the observations for all the three components in J band.

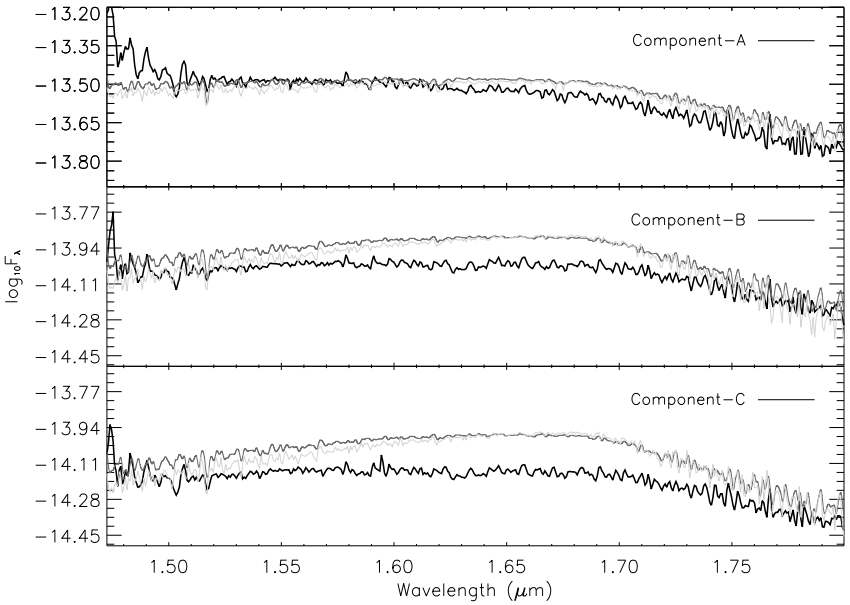

Figure 4.19 – Same as fig 4.18 for H band

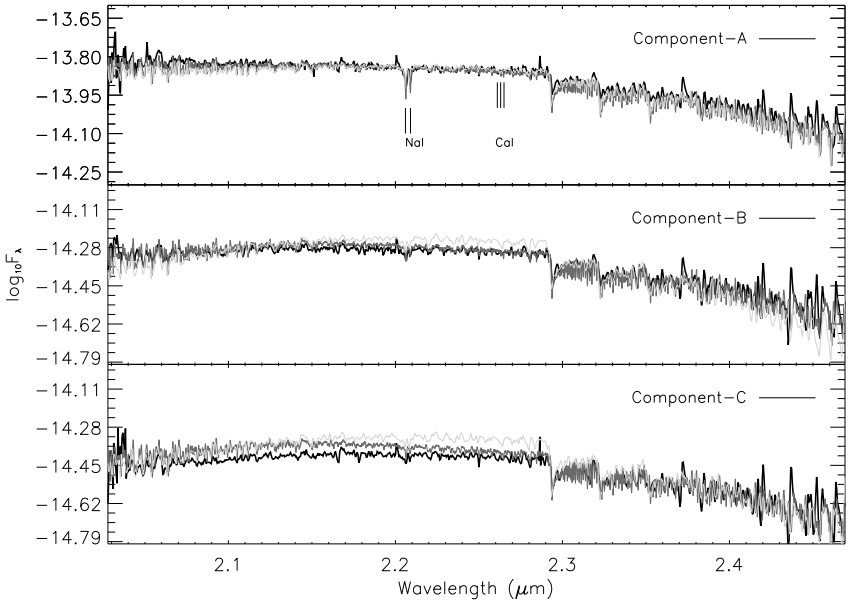

Figure 4.20 – Same as fig 4.18 for K band

spectrum of the unresolved system in the 3-14 μm range with the BT-Dusty, BT-Settl and DRIFT models (MARCS models are not available in this wavelength range). The synthetic spectra of the unresolved system are computed by adding the individual best fit synthetic spectra. The comparison is shown in fig. 4.21, where the ISOPHOT spectrum is in black, the BT-Dusty model in red, the BT-Settl model in green, and the DRIFT model in blue. Star symbols indicates the photometry obtained in the IR bands. The overall agreement is good except for the observed spectrum above 8.7 μm, where it gets quite noisy.

Relatively small differences distinguish the MARCS, DRIFT and BT models in the IR spectral range for the primary. In the case of the B and C components, the MARCS models suffer clearly of the lack of dust grain scattering which tends to flatten out or veil the spectral features in this spectra range. This effect is observed in the DRIFT, BT-Settl and BT-Dusty models which include dust formation. Differences in the cloud model approaches explain the differences between the DRIFT, BT-Dusty and BT-Settl models. The DRIFT models appear as dusty as the 2001 AMES-Dusty models with similar effective temperatures and surface gravities for B and C than derived by Leinert et al. (2000). The BT models tend to attribute slightly hotter effective temperatures (+100 K) and lower gravities (-0.5 dex) to these objects, while the dust-free MARCS models would attribute them the highest values (+200 K). But judging from the overall fits obtained to the NICMOS spectra it appears that neither of the models are yet dusty enough to explain the IR spectral distribution of B and C. Indeed the over-luminosity of the models in the J band could be attributed to missing or to weak veiling by dust scattering.

The Köhler et al. (2012) mass estimate for the primary requires a 150 to 300 K higher effective temperature and up to 30% larger radius than using the revised Seifahrt et al. (2008) mass, resulting in an over-prediction of the luminosity of up to one magnitude. In the case of the B and C components, the Köhler et al. (2012) mass estimates correspond to effective temperatures which are 100 to 200 K cooler than obtained in this study using the DRIFT models, and in correspondingly larger discrepancies with the BT-Settl fits. On the other hand, the results obtained in this paper for all three components are consistent with the isochrone interpolation for the revised Seifahrt et al. (2008) masses of the A, B and C components of LHS 1070 (see Table 4.2), and there is no evidence that the components may have been influenced by their binary nature.

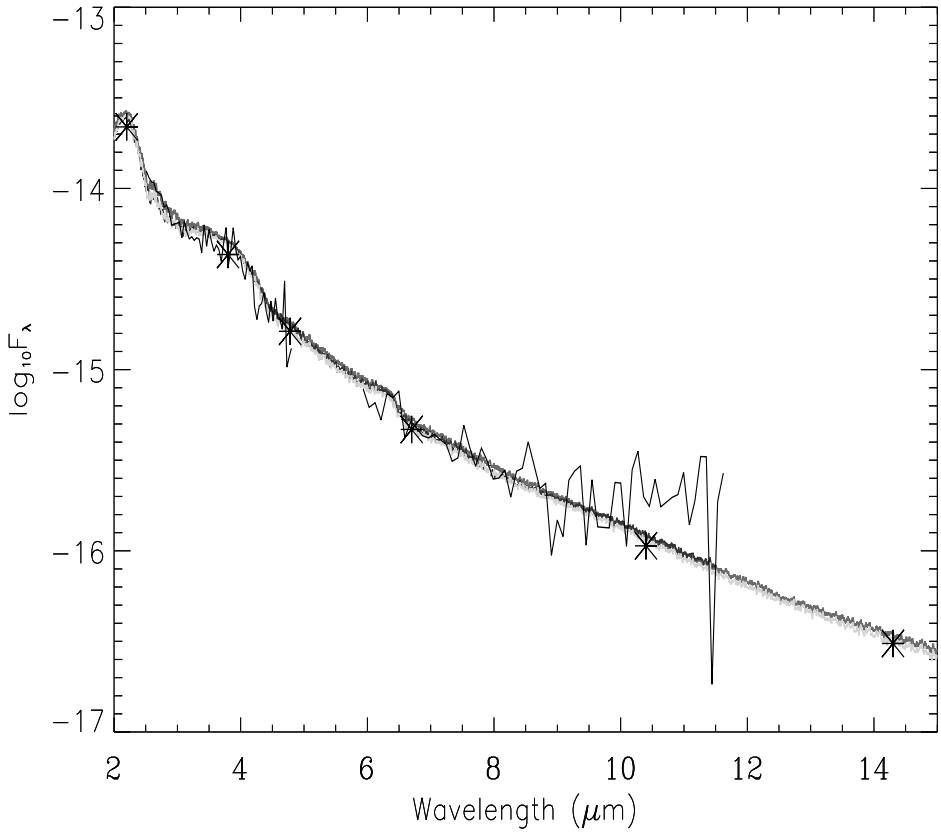

Figure 4.21 – Black: ISOPHOT thermal IR spectra of the unresolved system, with photometric measurements over plotted (stars). Red: best fit BT-Dusty model. Green: best fit BT-Settl model. Blue: best fit DRIFT model.

4.5 Discussion and Conclusion

This chapter presents the results from the spectral synthesis analysis for the LHS 1070 triple system. This system has been extensively observed from the optical to the IR, and dynamical

masses have been determined (Leinert et al. 2001; Seifahrt et al. 2008). Therefore, it constitutes a testbed of model atmospheres of low-mass stars. The components are classified as M5.5, M9.5, and L0 dwarfs, and their atmopshere lie in a temperature range where dust starts to form. Using a χ^2 square minimization technique, we have determined the physical parameters $T_{\rm eff}$, log g , metallicity and radius for all the three components of the LHS 1070 system by comparing them with the synthetic spectra computed with the most recent atmospheric models: BT-Dusty, BT-Settl, MARCS, and DRIFT. A solar metallicity is derived from all three models. The derived gravity differs by 0.5 dex depending on the model used but still agrees within the uncertainties with the values derived from dynamical mass (Seifahrt et al. 2008). By assuming an age of 1 Gyr, [M/H] = 0.0 and $T_{\rm eff}$ = 2900K for component A, 2500K for component B and 2400K for component C gives mass of $0.11 M_{\odot}$, $0.09 M_{\odot}$ and $0.08 M_{\odot}$ using Baraffe et al. (1998a) isochrones which is in agreement with (Seifahrt et al. 2008) mass. We found the same value for $T_{\rm eff}$ for the component A from all models while differences of 100 K and 200 K are found for component B and C. $T_{\rm eff}$ values found for component B and C are also 200 K higher than the Leinert et al. (2000) findings.

The main cause of these differences resides on the dust treatment. The AMES-Cond/Dusty models used by Leinert et al. (2000) only explored the limiting case of dust formation, considering dust formation in equilibrium with the gas phase whereas the BT-Settl model (Allard et al. 2010) includes a cloud model where in each atmospheric layer: 1) start concentrations of condensates are set to equilibrium values (nucleation is assumed efficient); 2) sedimentation and condensation timescales by Rossow (1978) are compared to the mixing efficiency (Freytag et al. 2010); 3) a gradual depletion occur as the solution progress from the bottom to the top of the atmosphere; and 4) the gas phase is systematically refreshed iteratively with the cloud model solution in each layer to account for the depletion of condensible elements from the gas phase composition. MARCS models are pure gas phase models where no grain formation is consider at all whereas the DRIFT model consider the dust cloud structure in which the seed grain size proceed via seed particle or by evaporation. Moreover the molecular opacities assumed in the MARCS model are different than the ones in the PHOENIX code used to compute the BT-Settl and DRIFT atmosphere models.

The derived parameters for LHS 1070 components agree with those derived using evolutionary models and observed bolometric luminosities (Baraffe et al. 1998a; Chabrier et al. 2000). However, we pointed out several discrepancies between the model atmospheres and the observed spectra. In the optical, the TiO bands around 7055 Å, CaH band around 6900 Å are recovered for all the components but we find that these bands are too strong in all the models. This might be due to the treatment of the dust settling in the atmosphere of the cool objects in the model. The VO band around 7334 Å is also visible and is quite well matched by the BT-Settl model. The overall fit for the B and C component is better with BT-Settl than DRIFT and MARCS model in the optical. The MgH feature at around 5200 Å is too strong in the all the models while the CaOH at 5500 Å band is missing in all models. The NaI doublet at around 5900 Å is far too strong as well as the CaH band at 7000 Å.

In the near-IR part the calculated fluxes are too high mainly in the J and H band. This indicates an inaccuracy in the atmosphere structure (outer temperatures too low) due to uncertainties in the oxygen composition of the star, to uncertainties in the treatment of the dust grains, or less likely to uncertainties and incompleteness of opacities as effective temperature decreases. The apparent weakness of NaI and CaI line in K band for all three components are clearly visible. These variations are mainly caused by the changing cloud thickness, inhomogeneous cloud distribution or changing opacity properties of the clouds where the condensation of dust could takes place. The recent development in the modeling of the atmosphere of very low mass stars by Allard et al. (2010) by considering the main molecular opacities sampling treatment in the BT2 water opacity line list (Barber et al. 2006), the revised solar opacity by Asplund et al. (2009) and also by considering the cloud model which is the cause for supersaturation and RHD mixing appears to be a breakthrough in the agreement of the modeled effective temperature scales with the observation of the late M-type dwarf star.

Table 4.1 – Photometric data. Fluxes F_λ are in log10(ergs cm^{-2} s^{-1}Å^{-1}).

Wavelength	Filter[1]	Component A	Component B	Component C	Components A+B+C	
μm			log10(F_λ)		log10(F_λ)	original notation
0.900	NIC1 F090M	−13.347 ± 0.010	−14.122 ± 0.016	−14.289 ± 0.017		156 ± 2 mJy^2
0.953	NIC1 F095N	−13.213 ± 0.031	−13.870 ± 0.03	−14.056 ± 0.036		253 ± 8 mJy^2
0.970	NIC1 F097N	−13.251 ± 0.031	−13.943 ± 0.027	−14.092 ± 0.028		237 ± 7 mJy^2
1.083	NIC1 F108N	−13.229 ± 0.024	−13.831 ± 0.017	−13.953 ± 0.017		332 ± 7 mJy^2
1.100	NIC1 F110M	−13.292 ± 0.006	−13.887 ± 0.007	−14.037 ± 0.009		295 ± 2 mJy^2
1.130	NIC3 F113N	−13.267 ± 0.022	−13.809 ± 0.073	−13.965 ± 0.097		343 ± 15 mJy^2
1.130	NIC1 F113N	−13.249 ± 0.020	−13.796 ± 0.019	−13.962 ± 0.022		355 ± 7 mJy^2
1.25	J	−13.350 ± 0.017	−13.904 ± 0.028	−14.036 ± 0.028	−13.189 ± 0.012	9.14 ± 0.03 mag
1.450	NIC1 F145M	−13.494 ± 0.005	−14.077 ± 0.005	−14.218 ± 0.005		326 ± 2 mJy^2
1.640	NIC1 F165M	−13.517 ± 0.004	−14.026 ± 0.004	−14.163 ± 0.004		419 ± 2 mJy^2
1.65	H	−13.535 ± −0.018	−14.061 ± 0.028	−14.195 ± 0.031	−13.367 ± 0.013	8.51 ± 0.03 mag
1.660	NIC3 F166N	−13.492 ± 0.013	−13.930 ± 0.084	−14.130 ± 0.133		472 ± 29 mJy^2
1.800	NIC2 F180M	−13.677 ± 0.006	−14.197 ± 0.008	−14.333 ± 0.009		346 ± 2 mJy^2
1.900	NIC1 F190N	−13.751 ± 0.014	−14.276 ± 0.007	−14.415 ± 0.008		324 ± 4 mJy^2
2.040	NIC2 F204M	−13.833 ± 0.006	−14.343 ± 0.004	−14.474 ± 0.004		314 ± 2 mJy^2
2.150	NIC2 F215N	−13.825 ± 0.013	−14.273 ± 0.005	−14.400 ± 0.006		378 ± 5 mJy^2
2.2	K	−13.860 ± 0.018	−14.339 ± 0.018	−14.468 ± 0.024	−13.674 ± 0.014	8.14 ± 0.03 mag
2.300	NIC2 F222M	−13.844 ± 0.004	−14.301 ± 0.003	−14.429 ± 0.003		378 ± 2 mJy^2
2.375	NIC2 F237M	−13.973 ± 0.005	−14.447 ± 0.003	−14.579 ± 0.003		317 ± 2 mJy^2
3.8	L’	−14.604 ± 0.013	−14.990 ± 0.013	−15.097 ± 0.014	−14.377 ± 0.012	7.63 ± 0.06 mag
4.78	M	−15.008 ± 0.019	−15.449 ± 0.028	−15.536 ± 0.041	−14.806 ± 0.017	7.72 ± 0.04 mag
6.7	LW2				−15.349 ± 0.019	70 ± 3 mJy
10.4	N	−16.190 ± 0.053			−15.973 ± 0.035	38.4 ± 3 mJy
14.3	LW3				−16.555 ± 0.043	21 ± 2 mJy

[1] M: medium-band filter ($\Delta\lambda = 0.1 - 0.2\mu$m), N: narrow-band filter ($\Delta\lambda = 0.02 - 0.04\mu$m)

[2] these values are the sum of the values measured directly for the individual components

Table 4.2 – Derived parameters for the LHS 1070 system. The uncertainties are drawn from the χ^2 maps and is 100 K for $T_{\rm eff}$. The metallicity is assumed to be [M/H] = 0 and log g = 5.0 to 5.5 (as explained in the text). The luminosity L is computed from the radius and effective temperature.

Component A				
Model	$T_{\rm eff}$ (K)	log g (dex)	Radius ($R_\odot$)	log(L) (ergs s^{-1})
BT-Dusty	2900	5.5	0.134±0.005	-2.93±0.090
BT-Settl	2900	5.0	0.134±0.005	-2.93±0.090
MARCS	2900	5.0	0.136±0.005	-2.92±0.090
DRIFT	2900	5.5	0.136±0.005	-2.92±0.031
Component B				
Model	$T_{\rm eff}$ (K)	log g (dex)	Radius ($R_\odot$)	log(L) (ergs s^{-1})
BT-Dusty	2500	5.5	0.102±0.004	-3.43±0.105
BT-Settl	2500	5.0	0.102±0.004	-3.43±0.105
MARCS	2600	5.0	0.098±0.002	-3.39±0.086
DRIFT	2400	5.5	0.106±0.005	-3.46±0.044
Component C				
Model	$T_{\rm eff}$ (K)	log g (dex)	Radius ($R_\odot$)	log(L) (ergs s^{-1})
BT-Dusty	2400	5.0	0.098±0.002	-3.53±0.090
BT-Settl	2400	5.0	0.098±0.002	-3.53±0.090
MARCS	2500	5.0	0.100±0.002	-3.44±0.090
DRIFT	2300	5.0	0.102±0.005	-3.57±0.034

Table 4.3 – Spectral indices values and derived spectral type computed from TiO and CaH band-strengths for component A and from the PC3 index for components B and C.

Component A		
TiO_5	0.211	M5.5
CaH_2	0.281	M5.5
CaH_3	0.557	M6
Component B		
PC3	2.305	M9.5
Component C		
PC3	2.608	L0

Chapter 5

The effective temperature scale of M dwarfs

5.1 Introduction

The $T_{\rm eff}$ scale of M dwarfs remains to this day model dependent to some level. Many efforts have been made to derive the effective temperature scale of M dwarfs. Due to the lack of very reliable model atmosphere, indirect methods such as blackbody fitting techniques have historically been used to estimate the effective temperature. The Bessell (1991) $T_{\rm eff}$ scale was based on blackbody fits to the near-IR (JHKL) bands by Pettersen (1980) and Reid & Gilmore (1984). The much cooler blackbody fits shown by Wing & Rinsland (1979) and Veeder (1974) were fits to the optical. Their fitting line was a continuation of the empirical $T_{\rm eff}$ relation for the hotter stars through the Pettersen (1980) and Reid & Gilmore (1984) NIR fits for the cooler stars. The work by Veeder (1974), Berriman & Reid (1987), Berriman et al. (1992), and Tinney et al. (1993) also used the blackbody fitting technique to estimate the $T_{\rm eff}$. Tsuji et al. (1996a) provide good $T_{\rm eff}$ using infrared flux method (IRFM). Casagrande et al. (2008) provide a modified IRFM $T_{\rm eff}$ for dwarfs including M dwarfs. These methods tend to underestimate $T_{\rm eff}$ since the blackbody carries little flux compared to the M dwarfs in the Rayleigh Jeans tail redwards of 2.5 μm. Temperatures derived from fitting to model spectra (Kirkpatrick et al. 1993b) are systematically $\sim$ 300 K warmer than those attained by empirical methods. This cooler $T_{\rm eff}$ scale for M dwarfs was corrected recently by Casagrande et al. (2012) bring it close to the Bessell (1991, 1995) $T_{\rm eff}$ scale.

Tinney & Reid (1998) determined an M dwarf $T_{\rm eff}$ scale in the optical by ranking the objects in order of TiO, VO, CrH, and FeH equivalent widths. Delfosse et al. (1999) pursued a similar program in the NIR with H_2O indices. Tokunaga & Kobayashi (1999) used a spectral colour index based on moderate dispersion spectroscopy in the K band. Leggett et al. (1996) used observed NIR low-resolution spectra and photometry for comparison with the AMES-Dusty models (Allard et al. 2001). They found radii and effective temperatures that are consistent with

the estimates based on photometric data from interior model or isochrone results. Leggett et al. (1998, 2000) revised their results by comparing the SED and NIR colours of M dwarfs to the same models. Their study provided for the first time a realistic temperature scale of M dwarfs.

In this chapter, we compare the revised BT-Settl synthetic spectra with the observed spectra of 152 M dwarfs using spectral synthesis and χ^2 minimization techniques, as well as colour-colour diagrams to obtain the atmospheric parameters (effective temperature, surface gravity and metallicity). We determine the revised effective temperature scale along the entire M dwarfs' spectral sequence and compare these results to those obtained by many authors.

5.2 Observations

Spectroscopic observations were carried out on the 3.6 mm New Technology Telescope (hereafter NTT) at La Silla Observatory (ESO, Chile) in November 2003 (Reylé et al. 2006). Optical low-resolution spectra were obtained in the red imaging and low-dispersion spectroscopy (RILD) observing mode with the ESO Multi Mode Instrument (hereafter EMMI) instrument. The spectral dispersion of the grism were used was 0.28 nm/pix, with a wavelength range of 385-950 nm. An order-blocking filter to avoid the second-order overlap that occurs beyond 800 nm. Thus the effective wavelength coverage ranges from 520 to 950 nm. The slit was 1 arcsec wide and the resulting resolution was 1 nm. The seeing varied from 0.5 to 1.5 arcsec. Exposure time ranged from 15 s for the brightest to 120 s for the faintest dwarf (I = 15.3). The reduction of the spectra was done using the context *long* of MIDAS. Fluxes were calibrated with the spectrophotometric standards LTT 2415 and Feige 110.

We use a sample of spectra for 97 M dwarfs along the entire spectral sequence. They are presented in Reylé et al. (2006); Phan-Bao et al. (2005); Crifo et al. (2005); Martín et al. (2010). The list of stars, their spectral types, and their optical and NIR photometry are given in Table 1. We compiled the photometry using the Vizier catalog access through the Centre de Données astronomiques de Strasbourg. It comes from the Naval Observatory Merged Astrometric Dataset (NOMAD) catalog (Zacharias et al. 2005), the Deep Near-Infrared Survey (DENIS, Epchtein 1997), and the Two Micron All Sky Survey (2MASS, Skrutskie et al. 2006), Reid et al. (2004, 2007), Koen & Eyer (2002); Koen et al. (2010).

The observations of 55 additional M dwarfs at Siding Spring Observatory (hereafter SSO) were carried out using the Double Beam Spectrograph (hereafter DBS),which uses a dichroic beamsplitter to separate the blue (300–630 nm) and red (620–1000 nm) light. The blue camera with a 300 l/mm grating provided a 2-pixel resolution of 0.4 nm, and the red camera with a 316 l/mm grating provided a 2-pixel resolution of 0.37 nm. The detectors were E2V 2048x512 13.5 micron/pixel CCDs. The observations were taken on Mar 27 2008. The spectrophotometric standards used were HD44007, HD45282, HD55496, HD184266, and HD187111

from the Next Generation Spectral Library (NGSL, version 1)[1] L745-46a and EG131 from http://www.mso.anu.edu.au/~bessell/FTP/Spectrophotometry/. The list of stars with their photometry are given in Tables 5.1 and 5.2

Spectral types for the NTT sample are obtained by visual comparison with a spectral template of comparison stars, observed together with the target stars at NTT as explained in Reylé et al. (2006). For comparison, we also derive spectral types using the classification scheme based on the TiO and CaH bandstrength (Reid & Gizis 1997). However, no comparison stars have been observed with the DBS at SSO. Thus, spectral types for the SSO sample are computed from TiO and CaH bandstrength. Although the instrument is different, we allow the comparison stars observed with EMMI on the NTT to be used as a final check. The results agree within 0.5 subclass.

5.3 Model atmospheres

For this study, we use the most recent BT-Settl models, which are partially published in a review by Allard et al. (2012a) and described by Allard & Homeier (2012). The details of BT-Settl model atmosphere is described in chapter 3.

5.4 $T_{\rm eff}$ determination

We use a least-square minimization program described in chapter 4 to derive a revised effective temperature scale of M dwarfs. The stars in our samples most probably belong to the thin disc of our Galaxy (Reylé et al. 2002; Reylé & Robin 2004). Thus we determine the $T_{\rm eff}$ of our targets by assuming solar metallicity. This is a reasonable assumption, as can be seen in Fig. 5.1 and 5.2 where we compare our two samples to three 5 Gyrs isochrones with solar, [M/H]= -0.5 and -1.0 dex. The samples are clearly compatible with solar metallicity.

Both theory and observation indicate that M dwarfs have $\log g = 5.0 \pm 0.2$ (Gizis 1996; Casagrande et al. 2008) except for the latest type M dwarfs. We therefore restrict our analysis to $\log g = 5.0 - 5.5$ models. Each synthetic spectrum was convolved to the observed spectral resolution; a scaling factor is applied to normalize the average flux to unity. We then compare each of the observed spectra with all the synthetic spectra in the grid by taking the difference between the flux values of the synthetic and observed spectra at each wavelength point. We interpolated the model spectra on the wavelength grid of the observed spectra. The sum of the squares of these differences is obtained for each model in the grid, and the best model for each object is selected. The best models were finally inspected visually by comparing them with the corresponding observed spectra. Due to the lower signal-to-noise ratio in the SSO 2.3 m

[1] http://archive.stsci.edu/prepds/stisngsl/index.html

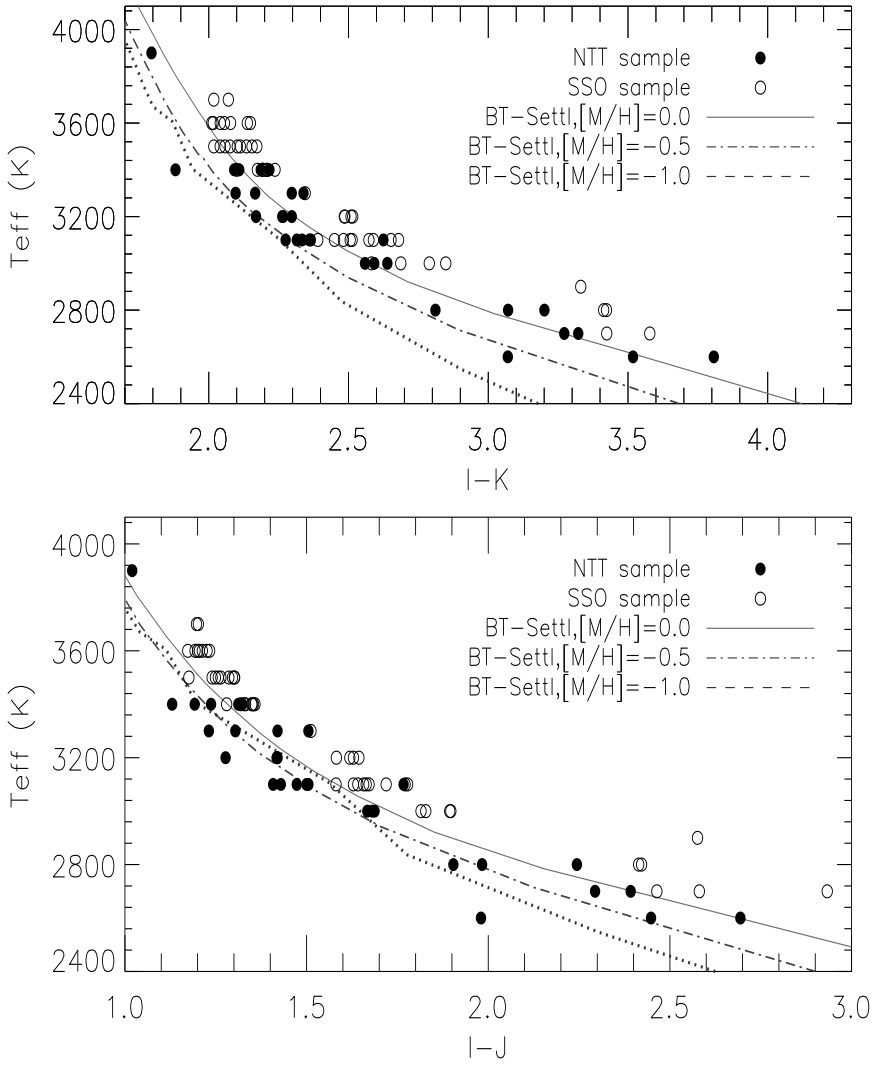

Figure 5.1 – $T_{\rm eff}$ vs NIR colours for observed M dwarfs (open and filled circle) compared to the values obtained with the 5 Gyrs isochrones from Baraffe et al. (1998b) at various metallicities.

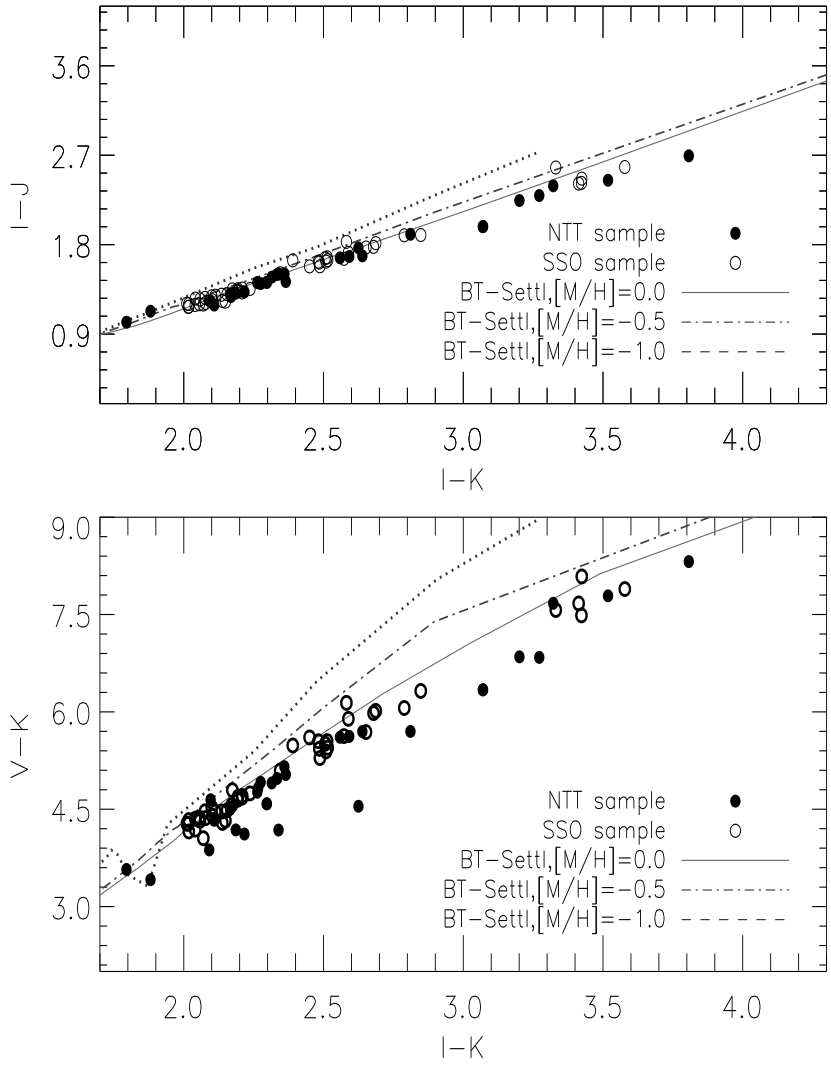

Figure 5.2 – colour-colour plot for observed M dwarfs (open and filled circle) compared to the values obtained with the 5 Gyrs isochrones from Baraffe et al. (1998b) at various metallicities.

spectra bluewards of 500 nm (see Fig. 5.4), especially for spectral types later than M4, we excluded this region below 500 nm from the χ^2 computation. We also checked the variation in effective temperature of the best fit as a function of the spectral type of the observed dwarfs. We found generally good agreement and conclude that our model-fitting procedure can be used to estimate the effective temperature with an uncertainty of ∼100 K. The purpose of this fit is to determine the effective temperature by fitting the overall shape of the optical spectra. No attempt has been made to fit the individual atomic lines, such as the K I and Na I resonance doublets. With the available resolution we cannot constrain the metallicity, high-resolution spectra would be necessary (Rajpurohit et al. 2012a). In addition, we checked the influence of the spectral resolution on our derived temperatures. We degraded the resolution of the spectra of SSO 2.3 m down to 1 nm and redid the procedure. No systematic difference in $T_{\rm eff}$ was found. The results are summarized in Tables 5.1 and 5.2.

5.5 Comparison between models and observations

5.5.1 Spectroscopic confrontation

The optical spectrum of M dwarfs is dominated by molecular band absorption, leaving no window onto the continuum (Allard 1990b). The major opacity sources in the optical regions are due to TiO and VO bands, as well as to MgH, CaH, FeH hydride bands and CAOH hydroxide bands in late-type M dwarfs. In M dwarfs of spectral type later than M6, the outermost atmospheric layers fall below the condensation temperature of silicates, giving rise to the formation of dust clouds (Tsuji et al. 1996a,b, Allard et al. 1997).

We compared the two samples of M dwarfs with the most recent BT-Settl synthetic spectra in Fig. 5.3 and 5.4 through the entire M dwarf spectral sequence. The synthetic spectra reproduce very well the slope of the observed spectra across the M dwarf regime. This is a drastic improvement compared to previous comparisons of earlier models (e.g., Leggett et al. 1998).

However, some indications of missing opacities persist in the blue part of the late-type M dwarf, such as the B' $^2\Sigma^+$<– X $^2\Sigma^+$ system of MgH (Skory et al. 2003a), and TiO and VO opacities around 8200 Å. Opacities are totally missing for the CaOH band at 5570 Å. The missing hydride bands of AlH and NaH between 3800 and 4600 Å among others could be responsible for the remaining discrepancies. We note that chromospheric emission fills the Na I D transitions in the latest type M dwarfs displayed here.

We see in this spectral regime no signs of dust scattering or of the weakening of features due to sedimentation onto grains until the M8 and later spectral types, where the spectrum becomes flat due to the sedimentation of TiO and VO bands and to the veiling by dust scattering.

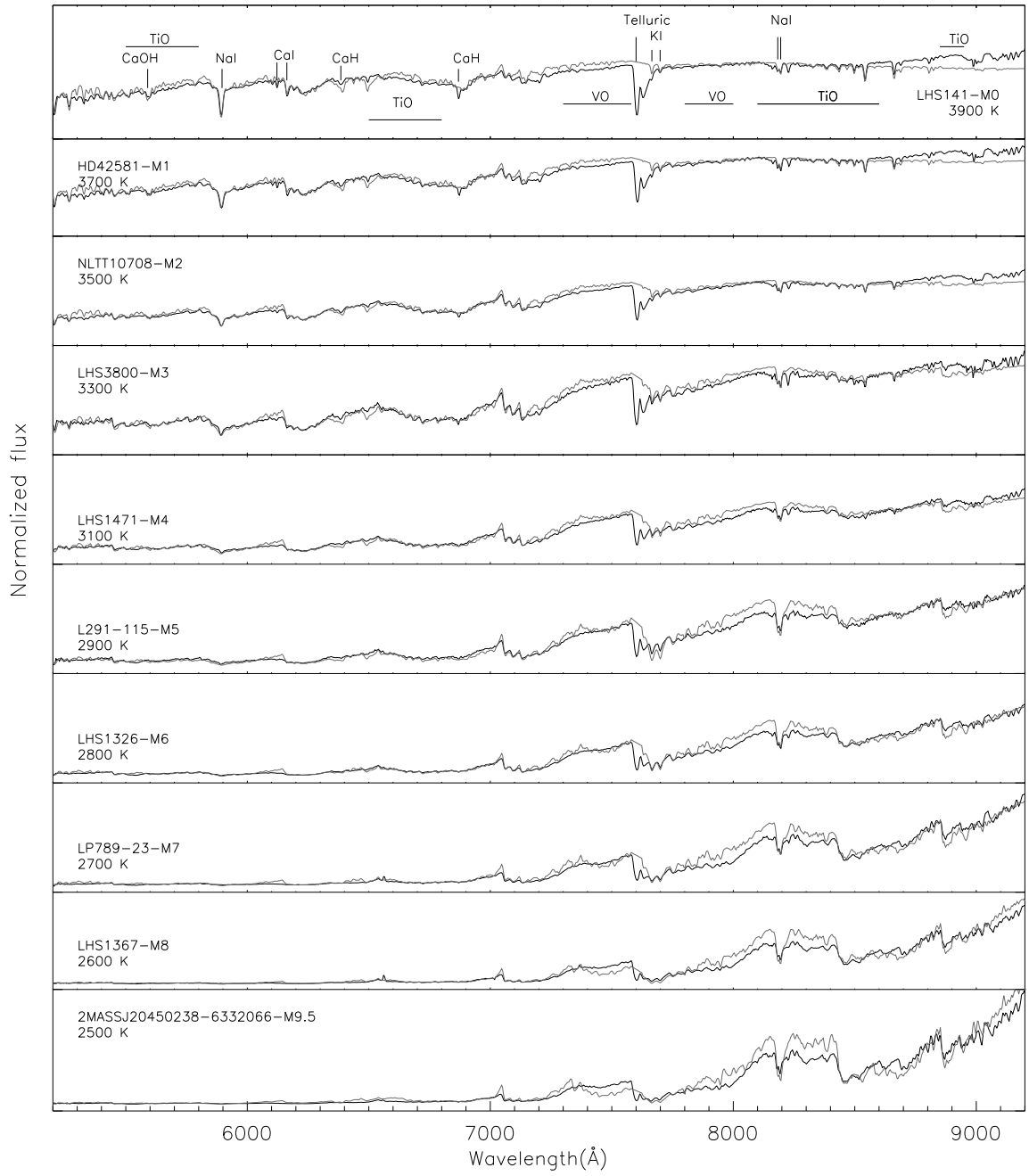

Figure 5.3 – Optical to red SED of M dwarfs from M0 to M9.5 observed with the NTT at a spectral resolution of 10.4 Å compared to the best fit BT-Settl synthetic spectra (red lines). The models displayed have a surface gravity of log g = 5.0 to 5.5. Telluric features near 7600 Å were ignored from the chi-square minimization.

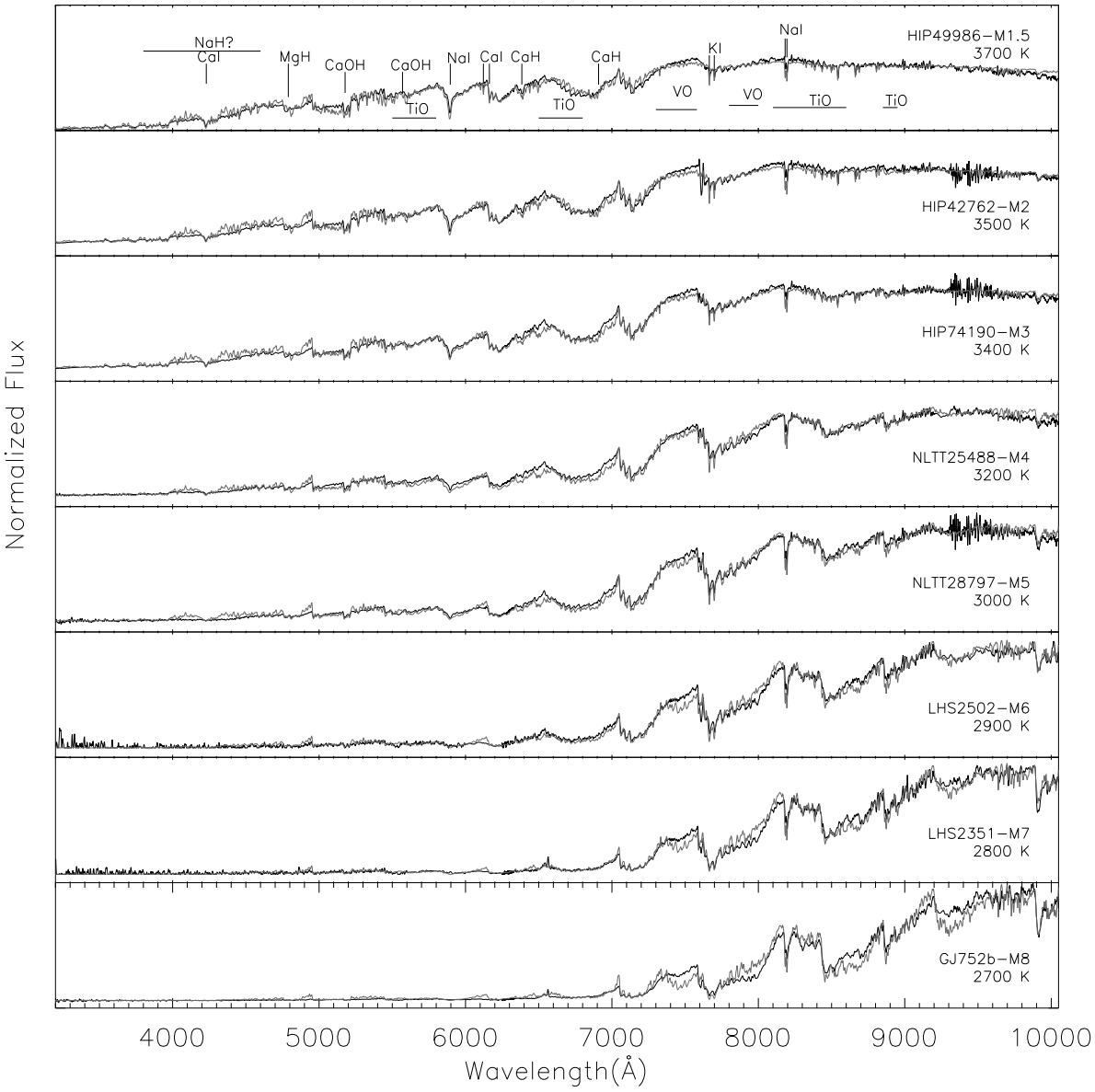

Figure 5.4 – Optical to red SED of M dwarfs from M1 to M8 observed with the SSO 2.3 m at a spectral resolution of 1.4 Å compared to the best fitting (chi-square minimization) BT-Settl synthetic spectra (red lines). The models displayed have a surface gravity of log g=5.0 to 5.5. At blue wavelengths (< 5000Å) the instrumental noise dominates the late-type M dwarfs.

5.5.2 Photometric confrontation

The models can be validated by comparing published isochrones interpolated into the new BT-Settl synthetic colour tables with observed photometry. We took the log g and $T_{\rm eff}$ for the fixed

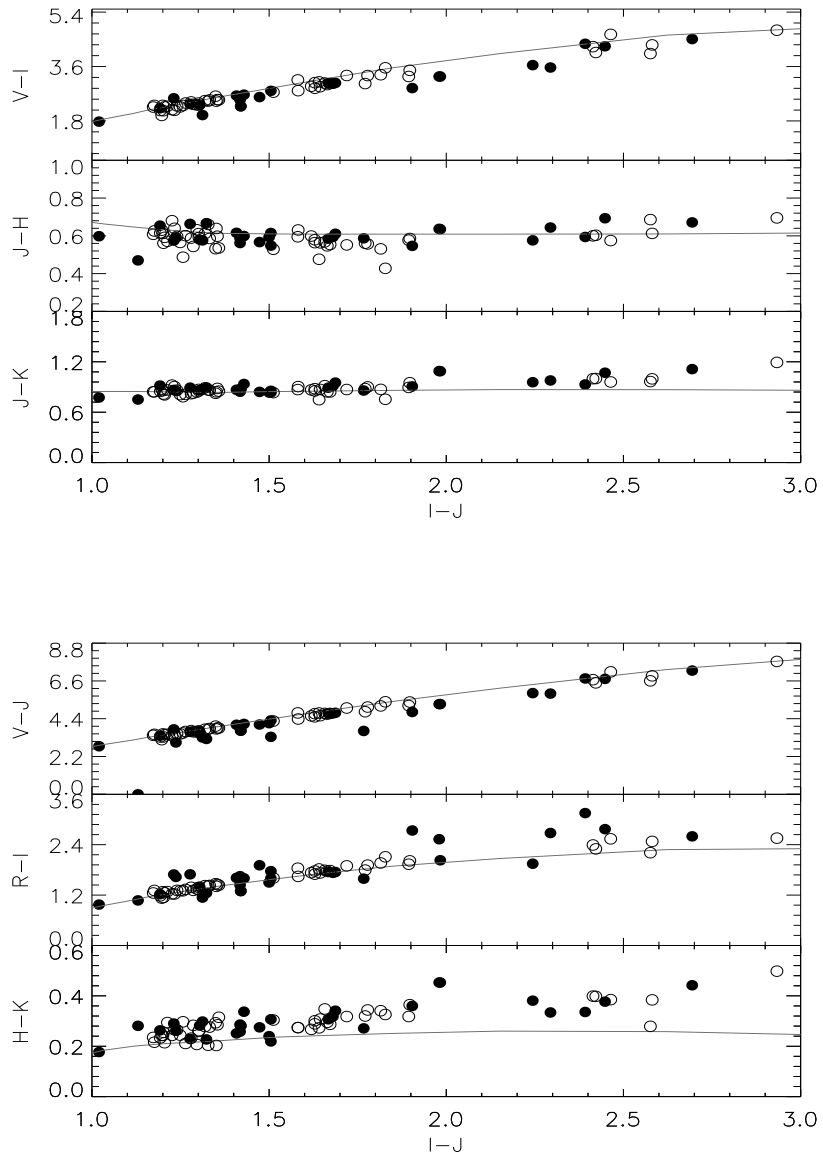

Figure 5.5 – Optical and NIR colours obtained with the 5 Gyrs isochrones from Baraffe et al. (1998b) at solar metallicity compared with the two observation samples (filled circles for the NTT sample and open circle for the SSO 2.3 m spectra). Typical error bars are comparable or smaller than the size of the symbols.

age of 5 Gyrs from Baraffe et al. (1998b) isochrones and calculated the colours of the star according to the BT-Settl models. The models are compared to observations in colour-colour diagrams in Fig. 5.5 for our two samples. The compiled photometry in the NTT sample is less homogeneous and translates to a larger spread, in particular for colours including the V and R band. This dispersion becomes dramatic for the coolest and faintest stars except for lowest mass objects at very young ages. The isochrone reproduces the two samples over the entire M dwarf spectral range in most colours. In particular, the models reproduce the V-band colours

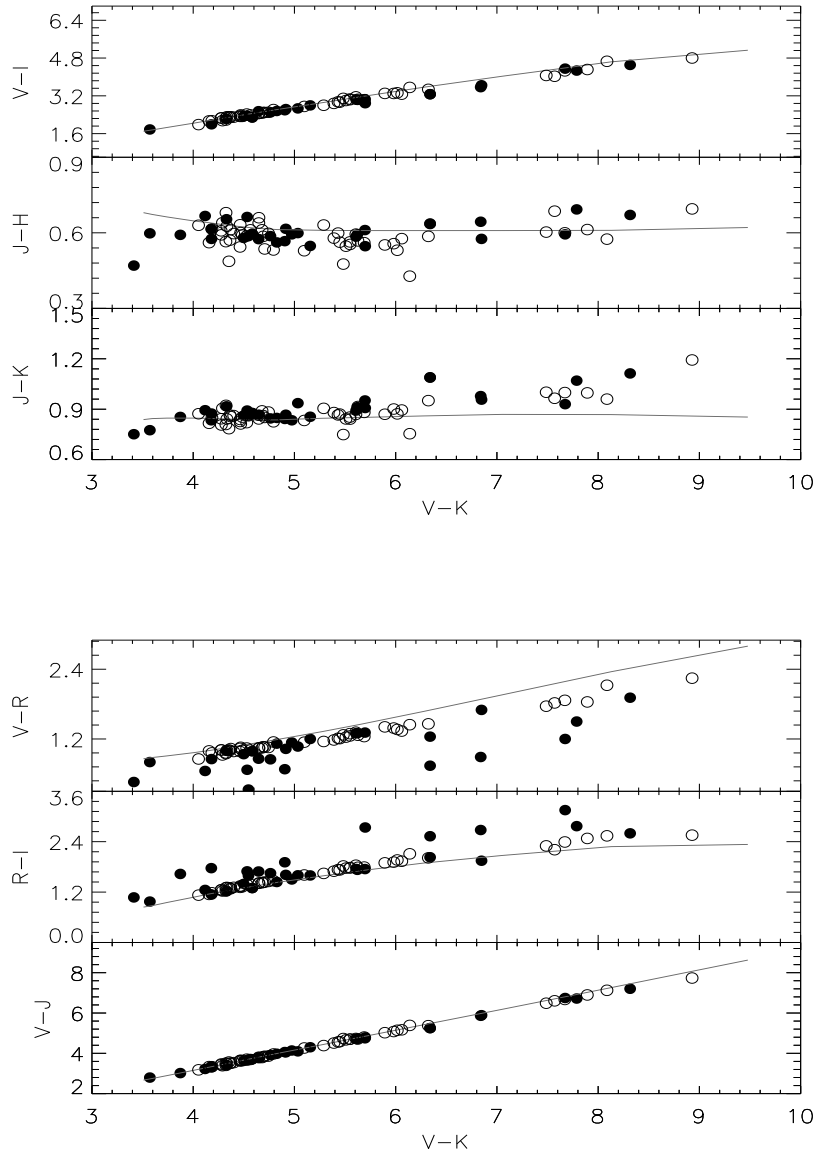

Figure 5.5 – Continued.

of M dwarfs, as illustrated by the V-I, V-J, and V-K colours. An increasing offset to the latest types persists in the H-K and V-R colour indices. The observations also suggest a flattening and possibly a rise in J-H and J-K to the latest types, which is not reproduced by the model. These inadequacies at the coolest temperature could be linked to missing opacities.

5.5.3 The $T_{\rm eff}$ scale of M dwarfs

The effective temperature scale versus spectral type is shown in Fig. 5.6. The $T_{\rm eff}$ scale determined using the NTT sample (filled circles) is in agreement with the SSO sample (open circles), but we found systematically 100 K higher $T_{\rm eff}$ for SSO samples for spectral types later than M5. The relation shows a saturation trend for spectral types later than M8. This illustrates the fact that the optical spectrum no longer changes sensitively with $T_{\rm eff}$ in this regime due to dust formation.

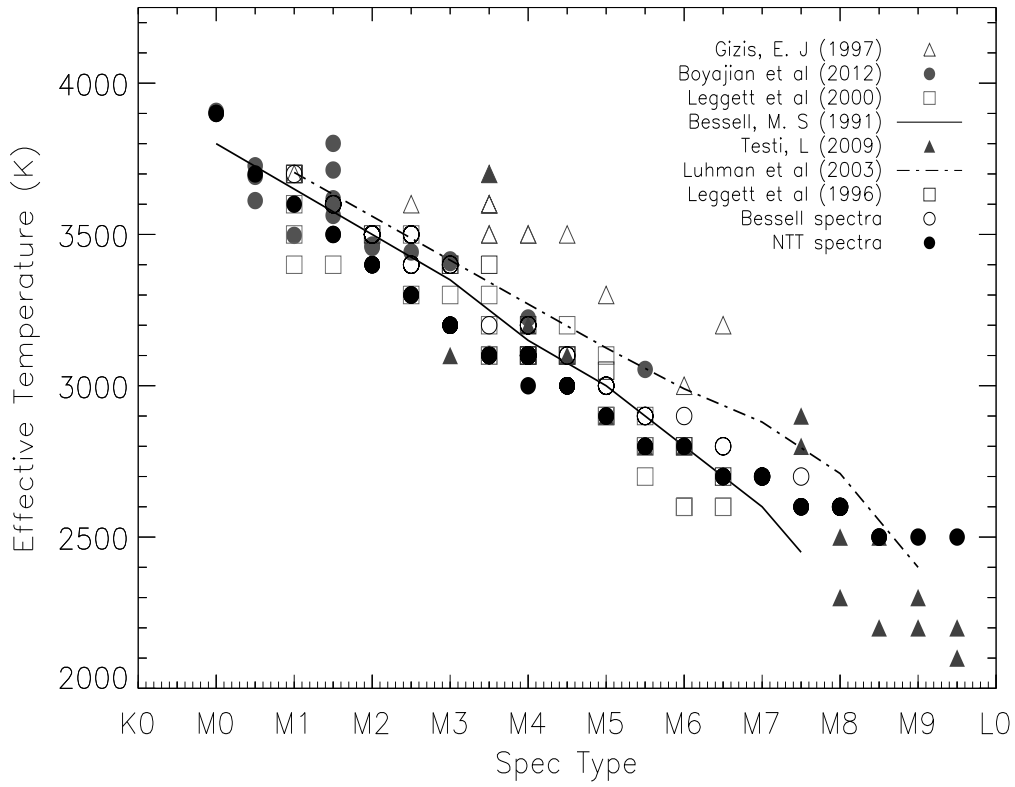

Figure 5.6 – Spectral type - $T_{\rm eff}$ relation obtained with the NTT sample (filled circles) and the SSO 2.3 m sample (open circles) compared to relations by Bessell (1991), Gizis (1997), Leggett et al. (1996), Leggett et al. (2000), Testi (2009), Boyajian et al. (2012) and Luhman (1999).

In the following we compare our scale to other works. Bessell (1991) determined the temperatures by comparing blackbodies to the NIR photometry of their sample. They used the temperature calibration of Wing & Rinsland (1979) and Veeder (1974). These calibrations were identical between $2700 \leq T_{\rm eff} \leq 3500$ K. Their scale agrees with the modern values for M dwarfs earlier than M6, but becomes gradually too cool with later spectral types and too hot for earlier M types.

Leggett et al. (1996) used the base grid by Allard & Hauschildt (1995b), which covers the

range of parameters down to the coolest known M dwarfs, M subdwarfs, and brown dwarfs. They obtained the $T_{\rm eff}$ of M dwarfs by comparing the observed spectra to the synthetic spectra. They performed their comparison independently at each of their four wavelength regions: red, J, H, and K. The different wavelength regions gave consistent values of $T_{\rm eff}$ within 300 K. Gizis (1997) used the NextGen model atmosphere grid by Allard et al. (1997). These models include more molecular lines from ab initio simulations (in particular for water vapor) than the previous base model grid. Leggett et al. (2000) used the more modern AMES-Dusty model atmosphere grid by Allard et al. (2001). They obtained a revised $T_{\rm eff}$ scale which is 150-200 K cooler for early Ms and 200 K hotter for late Ms than the scale presented in Fig. 5.6. Testi (2009) determined the $T_{\rm eff}$ by fitting the synthetic spectra to the observations. They used three classes of models: the AMES-Dusty, AMES-Cond, and the BT-Settl models. With some individual exceptions they found that the BT-Settl models were the most appropriate for M type and early L-type dwarfs.

Boyajian et al. (2012) used the interferometric angular diameter, Hipparcos parallax and new measurements of the star's bolometric flux to compute the $T_{\rm eff}$ of K0 to M4 main sequence stars. We compared their $T_{\rm eff}$ measurements with our findings. We have found good agreement within 100 K between our $T_{\rm eff}$ determination Boyajian et al. (2012).

Finally, for spectral types later than M0, Luhman et al. (2003) adopted the effective temperature, which is based on the NextGen and AMES-Dusty evolutionary models of Baraffe et al. (1998b) and Chabrier et al. (2000), respectively. They obtained the $T_{\rm eff}$ by comparing the H-R diagram from theoretical isochrones of Baraffe et al. (1998b) and Chabrier et al. (2000). For M8 and M9, Luhman et al. (2003) adjusted the temperature scale from Luhman (1999), so that spectral sequence falls parallel to the isochrones. Their $T_{\rm eff}$ conversion is likely to be inaccurate at some level, but as it falls between the scales for dwarfs and giants, the errors in $T_{\rm eff}$ are modest.

The different $T_{\rm eff}$ scales are in agreement within 250-300 K. But the Gizis (1997) relation shows the largest differences with the largest $T_{\rm eff}$ values (up to 500 K). This is due to the incompleteness of the TiO and water vapor line lists used in the NextGen model atmospheres. We also note also how the Luhman et al. (2003) $T_{\rm eff}$ scale is gradually overestimating $T_{\rm eff}$ towards the bottom of the main sequence for spectral types later than M4.

$T_{\rm eff}$ versus colour relations are shown in Fig. 5.7 in various photometric bands. The photometry of our NTT sample (filled circles) is compiled from the literature, which causes a large spread, particularly in the V and R band. The SSO 2.3 m sample (filled triangles) in comparison is more uniform. Our relations are compared to the predictions from BT-Settl isochrones at 5 Gyrs. The relations show that the model is able to reproduce quite properly the colours of M dwarfs, even in the V-band. There is a slight offset visible in the R band due to missing molecular opacities (see above). These relations are compared to previously published relations when available.

Berriman et al. (1992) derive the $T_{\rm eff}$ by matching the blackbody flux anchored at K band (2.2 μm) to the total bolometric flux, including both the spectroscopic and photometric ob-

served data points. They estimated the uncertainties in $T_{\rm eff}$ to be ± 4%. Leggett et al. (1996) used the synthetic I-K and I-J colours to estimate $T_{\rm eff}$. Leggett et al. (1996) used synthetic broadband colours from the preliminary version of AMES-Dusty model produced by Allard et al. (1994a). They used the V-K, I-K, J-H, and H-K colours assuming log$g$ = 5.0 and solar metallicity,finding a hotter $T_{\rm eff}$ scale (by on average 130 K) than that of Berriman et al. (1992). More recently, Casagrande et al. (2008) used the PHOENIX Cond-GAIA model atmosphere grid (P. H. Hauschildt, unpublished) to determine the atmospheric parameters of their sample of 343 nearby M dwarfs with high-quality optical and NIR photometry. These models are similar to those published by Allard et al. (2001), with the exception that they were computed by solving the radiative transfer in spherical symmetry.

The authors determined the $T_{\rm eff}$ using a version of the multiple optical-infrared method (IRFM) generalized to M dwarfs, and elaborated by Blackwell & Shallis (1977) and Blackwell et al. (1979, 1980). Figure 5.7 shows that the Casagrande et al. (2008) $T_{\rm eff}$ scale is systematically, and progressively with decreasing $T_{\rm eff}$, cooler than the BT-Settl isochrones. Given that a large number of stars are common with Casagrande et al. (2008) sample, we did a star-by-star comparison of the $T_{\rm eff}$ determination. The values are given in Tables 5.1 and 5.2. The comparison confirms the systematic offset in the temperature scale. For cooler stars with $T_{\rm eff} \leq 3000$ K, the $T_{\rm eff}$ determinations diverge by 100 to 300 K. This is due, among other things, to the use of the Grevesse et al. (1993) solar elemental abundances (see Allard et al. 2012 for a comparison of the different solar elemental abundance determinations and their effects on model atmospheres).

5.6 Conclusion

We have compared a revised version of the BT-Settl model atmospheres (Allard et al. 2012a) to the observed NTT and SSO 2.3 m spectra and colours. The use of revised TiO line list is very important and provides a more accurate description of the TiO bands in the M dwarfs. The systematic discrepancy between the delta and epsilon bands found by Reiners (2005), which seriously affected the effective temperature determination, is largely alleviated by using the Plez (1998) and B. Plez (private communication) TiO line list although discrepancies remain for the coolest stars. The BT-Settl models reproduce the SED and observed colours across the M dwarfs' spectral regime in unprecedented quality, as well as the colours. The V band is also well reproduced by the models. Discrepancies remain in the strength of some molecular absorption bands while other absorption bands are missing, in particular in the blue spectral range.

Effective temperatures were determined by using a least-square minimization routine, which gives accurate temperatures within 100 K uncertainty. We compared our temperature colour to relations using multi-wavelength photometry with the predictions from BT-Settl isochrones, assuming an age of 5 Gyrs. In general, the BT-Settl isochrones are in good agreement with the observed colours, even at temperatures below 2800 K affected by dust treatment in the BT-Settl models. We found that the Casagrande et al. (2008) $T_{\rm eff}$ scale is systematically cooler than

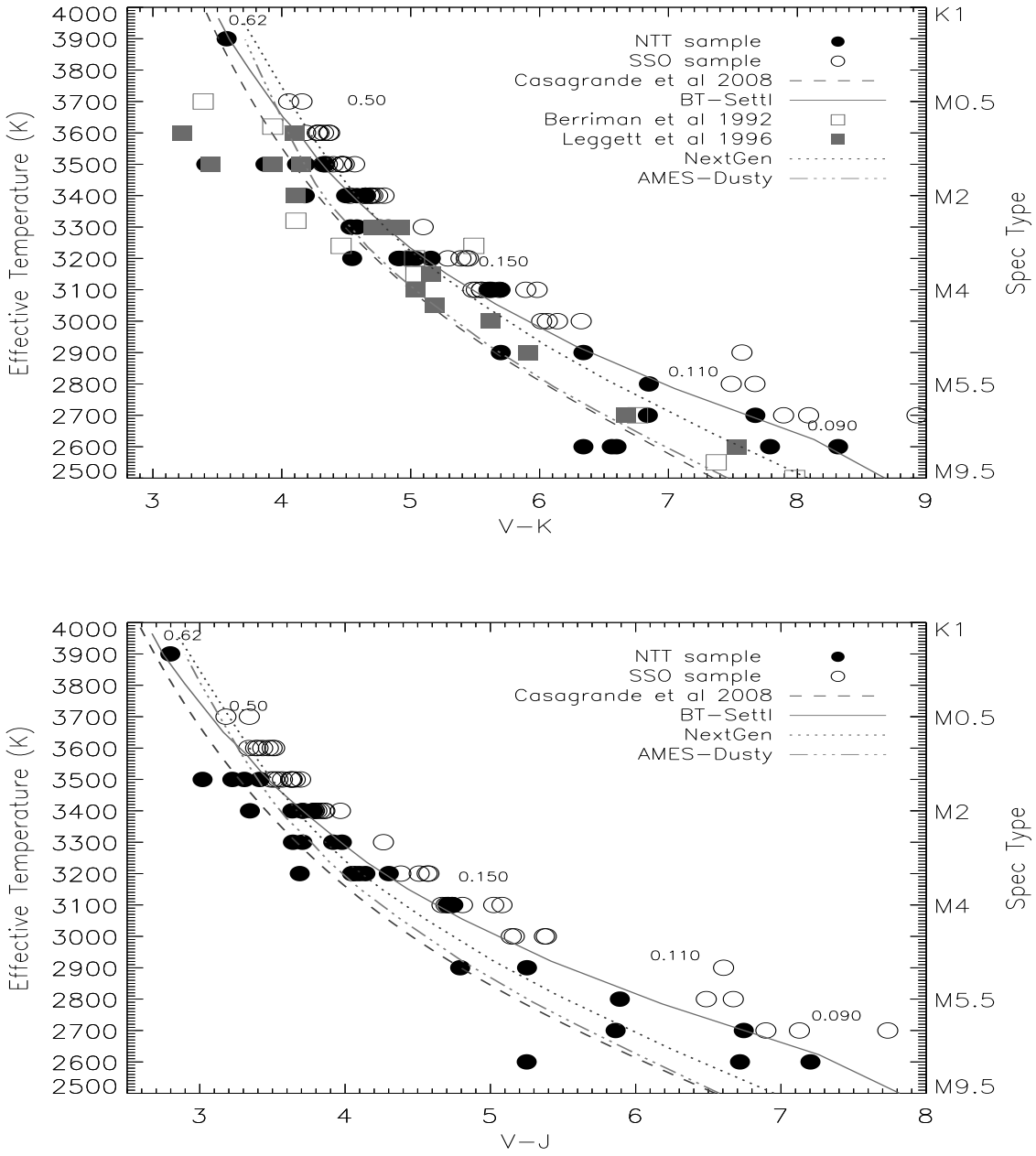

Figure 5.7 – coloured $T_{\rm eff}$ plots in different bands from the NTT sample (filled circles) and the SSO 2.3 m sample (open circles). Spectral types are also indicated. The predictions from BT-Settl (solid line), NextGen (dotted line), and AMES-Dusty (dash-dotted) for solar metallicities are over plotted. Theoretical masses in solar mass are indicated. Predictions from other authors are shown for comparison when available.

the BT-Settl isochrones due, among other things, to the Grevesse et al. (1993) solar elemental abundances adopted in the GAIA-Cond model atmosphere grid used for that work. In contrast the Luhman et al. (2003) $T_{\rm eff}$ scale is progressively too hot towards the bottom of the main sequence. This study enable us to improve the BT-Settl models. New interior and evolution

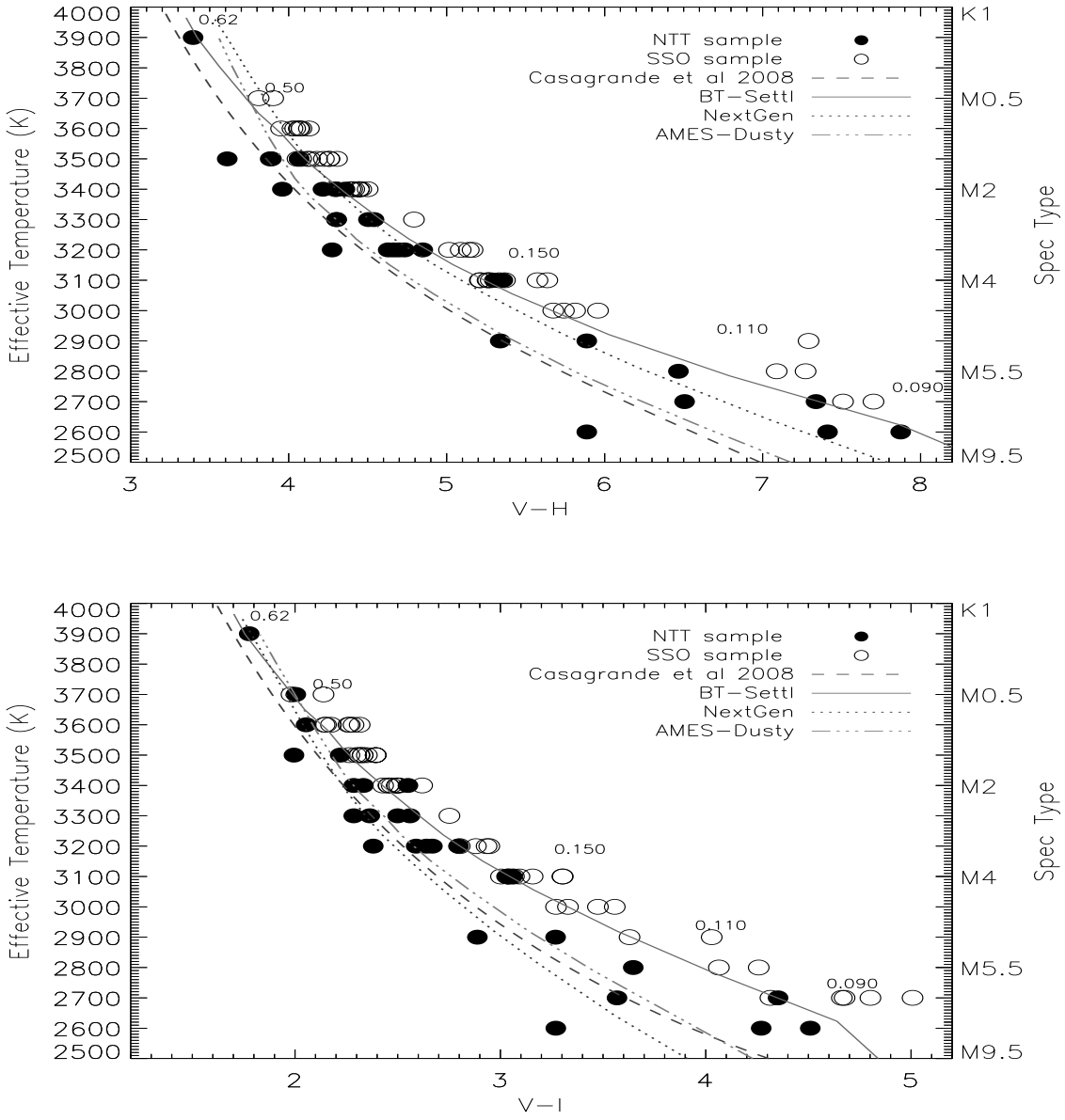

Figure 5.7 – Continued.

models based on the BT-Settl models are currently being prepared.

We provide and compare temperature versus colour relations in the optical and infrared, which match well the BT-Settl isochrones and can be further used for large photometric datasets. We determined the effective temperature scale for the M dwarfs in our samples. It extended down to the latest type of M dwarfs, where the dust cloud begins to form in their atmosphere.

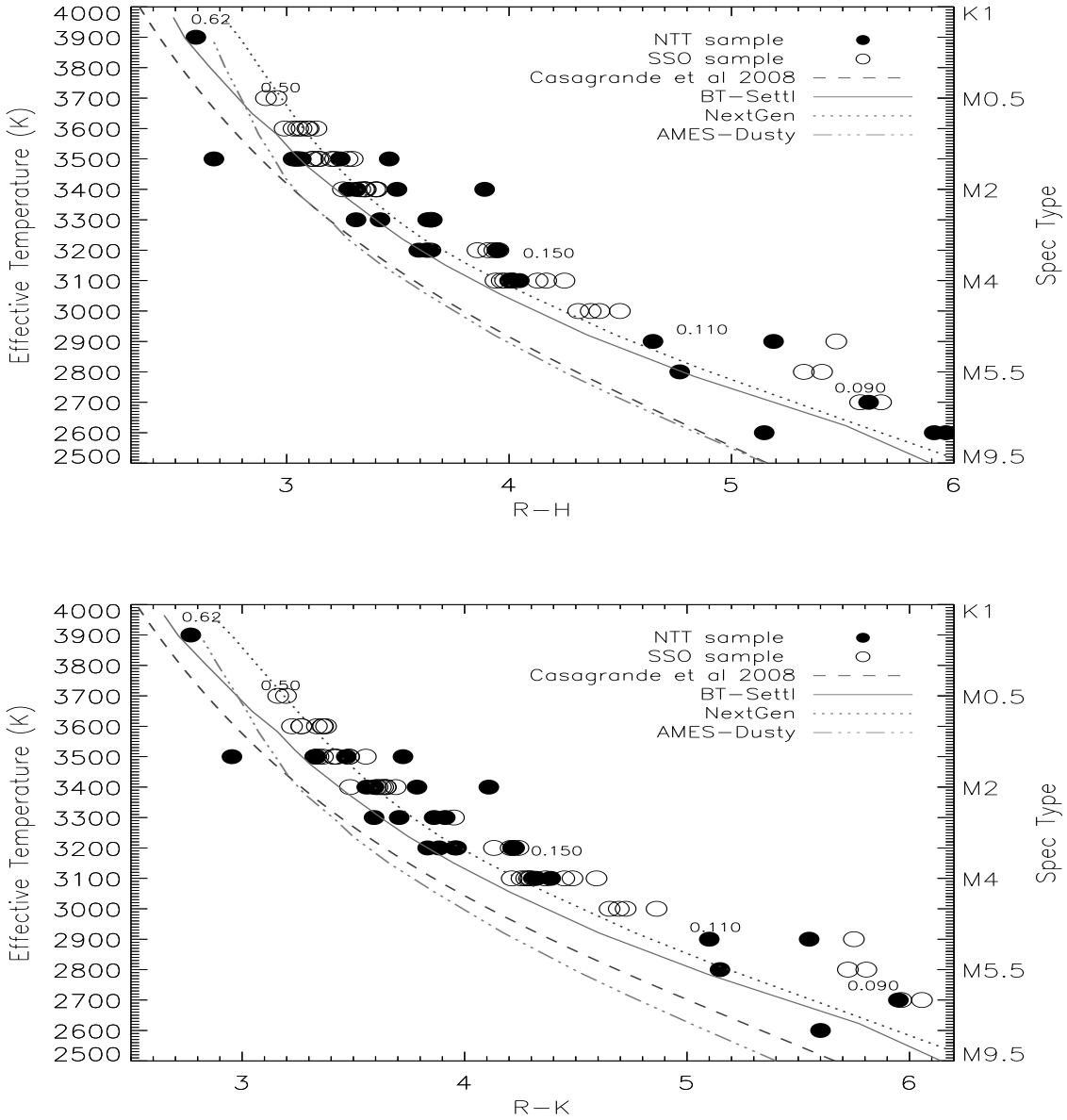

Figure 5.7 – Continued.

Table 5.1 – Observable and physical quantities for our sample of stars observed at NTT with EMMI.

Name	Spectral Type	$T_{\rm eff}$ (K)	$T_{\rm eff}$ [b] (K)	log g (cms^{-2})	V	R	I	J	H	K
Gl143.1[a]	K7	3900	—	5.0	10.03	9.15	—	—	—	—
LHS141	M0	3900	—	5.0	10.15	9.35	8.38	7.36	6.76	6.58
LHS3833[a]	M0.5	3800	—	5.0	10.06	9.33	—	—	—	—
HD42581[a]	M1	3700	—	5.0	8.12	7.16	6.12	—	—	—
LHS14[a]	M1.5	3600	—	5.0	10.04	9.09	7.99	—	—	—
LHS65[a]	M1.5	3600	3567	5.0	10.86	10.31	10.64	—	—	—
L127-33	M2	3500	—	5.0	14.19	14.04	12.41	11.17	10.58	10.32
NLTT10708	M2	3500	—	5.0	11.16	10.31	9.17	7.86	7.28	6.98
LP831-68	M2	3500	—	5.0	11.02	10.02	8.80	7.61	6.95	6.69
NLTT83-11	M2	3500	—	5.0	12.90	12.25	11.00	9.68	9.01	8.78
APMPMJ0541-5349	M2	3500	—	5.0	13.30	12.84	11.77	10.64	10.17	9.89
LHS1656	M2.5	3400	—	5.0	13.30	12.44	10.75	9.52	8.94	8.65
LP763-82	M2.5	3400	—	5.0	12.19	11.25	9.86	8.55	7.97	7.69
LP849-55	M2.5	3400	—	5.0	13.32	13.25	11.48	9.97	9.36	9.14
LHS5090	M3	3300	—	5.0	—	14.97	12.85	11.58	11.04	10.84
LHS3800	M3	3300	—	5.0	—	—	12.23	10.93	10.39	10.15
LHS3842	M3	3300	—	5.0	13.80	12.95	11.30	9.88	9.29	9.04
LHS1293	M3	3300	—	5.0	13.65	12.66	11.36	9.94	9.35	9.07
LP994-114	M3	3300	—	5.0	—	11.59	10.36	9.00	8.37	8.15
LTT9783	M3	3300	—	5.0	—	12.11	10.56	9.17	8.59	8.34
LP715-39	M3	3300	3161	5.0	12.65	11.53	10.09	8.67	8.11	7.82
LHS1208[a]	M3	3300	—	5.0	9.85	8.97	—	—	—	—
LEHPM4417	M3	3300	—	5.0	13.73	13.06	11.37	10.09	9.43	9.20

[a] Saturation in NIR bands.

[b] $T_{\rm eff}$ from Casagrande et al. (2008).

Table 5.1 Continued.

Name	Spectral Type	$T_{\rm eff}$ (K)	$T_{\rm eff}$ [b] (K)	log g (cms^{-2})	V	R	I	J	H	K
LP831-45	M3.5	3200	3125	5.0	12.54	11.51	9.90	8.49	7.88	7.62
2MASSJ04060688-0534444	M3.5	3200	—	5.0	13.29	12.28	—	9.13	8.55	8.30
LP834-32	M3.5	3200	3108	5.0	12.38	11.24	9.74	8.24	7.65	7.41
LHS502[a]	M3.5	3200	—	5.0	11.49	10.43	9.11	—	—	—
LEHPM 1175	M3.5	3200	—	5.0	—	13.08	11.51	10.01	9.47	9.17
LEHPM1839	M3.5	3200	—	5.0	—	13.32	12.11	10.55	9.95	9.71
L130-37	M3.5	3200	—	5.0	13.04	11.97	10.37	8.94	8.34	8.01
LEHPM6577	M3.5	3200	—	5.0	—	13.03	11.79	10.34	9.73	9.47
L225-57	M4	3200	—	5.0	—	11.70	9.79	8.23	7.61	7.31
LP942-107	M4	3200	3052	5.0	13.93	12.73	11.13	9.63	9.08	8.77
LP772-8	M4	3200	—	5.0	14.11	13.43	11.52	10.05	9.48	9.20
LP1033-31	M4	3200	—	5.0	—	12.12	10.54	9.10	8.46	8.21
L166-3	M4	3200	—	5.0	—	12.76	11.33	9.83	9.28	9.00
LP877-72	M4	3200	—	5.0	—	11.—	10.22	8.86	8.24	8.00
LP878-73	M4	3200	—	5.0	14.55	14.22	12.63	10.86	10.27	10.00
LP987-47	M4	3200	—	5.0	—	—	10.82	9.41	8.78	8.55
LP832-7	M4	3200	—	5.0	14.09	13.45	—	9.87	9.24	8.98
LHS183	M4	3200	—	5.0	12.79	11.51	—	8.57	8.00	7.75
LHS1471	M4	3200	—	5.0	—	13.22	11.56	9.94	9.37	9.08
APMPMJ2101-4125	M4	3200	—	5.0	—	13.34	11.47	9.96	9.38	9.09
APMPMJ2101-4907	M4	3200	—	5.0	—	—	10.52	9.12	8.48	8.19
LEHPM3260	M4	3200	—	5.0	—	12.53	10.60	9.13	8.54	8.19
LEHPM3866	M4	3200	—	5.0	—	—	11.82	10.21	9.58	9.29
LEHPM5810	M4	3200	—	5.0	—	13.58	11.66	9.91	9.33	9.05
LHS5045	M4.5	3100	—	5.0	—	—	10.78	9.17	8.60	8.24

[a] Saturation in NIR bands.

[b] $T_{\rm eff}$ from Casagrande et al. (2008).

Table 5.1 Continued.

Name	Spectral Type	$T_{\rm eff}$ (K)	$T_{\rm eff}$ [b] (K)	log g (cms^{-2})	V	R	I	J	H	K
LP940-20	M4.5	3100	—	5.0	—	14.87	12.65	10.92	10.32	10.01
L170-14A	M4.5	3100	—	5.0	—	12.86	11.50	9.76	9.13	8.88
LHS1201	M4.5	3100	—	5.0	17.55	15.52	12.90	11.12	10.52	10.25
LHS1524	M4.5	3100	—	5.0	—	14.45	12.65	10.98	10.45	10.17
LTT1732	M4.5	3100	—	5.0	—	13.19	11.27	9.69	9.11	8.80
LP889-37	M4.5	3100	2923	5.0	14.52	13.21	11.46	9.77	9.16	8.82
LHS5094	M4.5	3100	—	5.0	14.02	12.72	10.97	9.30	8.72	8.41
LP655-43	M4.5	3100	2924	5.0	14.44	13.14	11.41	9.73	9.14	8.82
LHS138[a]	M4.5	3100	—	5.0	12.07	10.70	8.94	—	—	—
APMPMJ1932-4834	M4.5	3100	—	5.0	—	14.38	12.37	10.63	10.02	9.72
2MASSJ23522756-3609128	M4.5	3100	—	5.0	—	17.27	—	13.09	12.57	12.28
LEHPM640	M4.5	3100	—	5.0	17.74	14.26	12.30	10.76	10.14	9.90
LEHPM1853	M4.5	3100	—	5.0	—	12.77	11.03	9.46	8.85	8.61
LEHPM3115	M4.5	3100	—	5.0	—	13.94	12.10	10.49	9.92	9.63
LEHPM4771	M4.5	3100	—	5.0	17.74	13.79	11.29	9.54	8.95	8.63
LEHPM4861	M4.5	3100	—	5.0	—	13.28	11.75	10.13	9.60	9.34
L291-115	M5	2900	—	5.0	15.88	14.90	12.26	10.44	9.83	9.54
LP904-51	M5	2900	—	5.0	—	15.32	12.84	11.04	10.44	10.16
LHS168	M5	2900	—	5.0	13.78	12.60	—	8.77	8.21	7.83
LP829-41	M5.5	2800	—	5.0	16.10	15.95	13.21	11.31	10.76	10.40
LP941-57	M5.5	2800	—	5.0	—	14.88	12.98	11.06	10.47	10.13
LHS546	M5.5	2800	—	5.0	14.69	—	—	9.15	8.50	8.18
LP714-37	M5.5	2800	—	5.5	16.26	15.02	12.99	11.01	10.37	9.92

[a] Saturation in NIR bands.

[b] $T_{\rm eff}$ from Casagrande et al. (2008).

Table 5.1 Continued.

Name	Spectral Type	$T_{\rm eff}$ (K)	$T_{\rm eff}$ [b] (K)	log g (cms^{-2})	V	R	I	J	H	K
LHS1326	M6	2800	—	5.5	15.61	14.49	—	9.84	9.25	8.93
2MASSJ12363959-1722170	M6	2800	—	5.0	17.56	15.86	13.91	11.67	11.09	10.71
2MASSJ21481595-1401059	M6.5	2700	—	5.0	—	20.20	17.15	14.68	14.11	13.65
2MASSJ05181131-3101519	M6.5	2700	—	5.0	17.74	16.85	14.17	11.88	11.23	10.90
LP788-1	M6.5	2700	—	5.0	—	16.66	13.36	11.07	10.47	10.07
APMPMJ1251-2121	M6.5	2700	—	5.0	—	16.65	13.78	11.16	10.55	10.13
APMPMJ2330-4737	M7	2700	—	5.0	—	—	13.70	11.23	10.64	10.28
LP789-23	M7	2700	—	5.0	—	17.90	14.55	12.04	11.39	10.99
LHS292	M7	2700	—	5.5	15.60	14.40	11.25	8.86	8.26	7.93
2MASSJ03144011-0450316	M7.5	2600	—	5.0	—	19.43	—	12.64	12.00	11.60
LHS1604	M7.5	2600	—	5.0	18.02	16.52	13.75	11.30	10.61	10.23
LP714-37	M7.5	2600	—	5.5	16.26	15.52	12.99	11.01	10.37	9.92
LP655-48	M7.5	2600	2250	5.0	17.86	15.95	13.35	10.66	9.99	9.54
LP851-346	M7.5	2600	—	5.5	—	16.79	13.77	10.93	10.29	9.88
LHS1367	M8	2600	—	5.0	—	17.34	14.18	11.62	10.95	10.54
2MASSJ05022640-0453583	M8	2600	—	5.0	—	20.39	17.35	14.52	13.95	13.58
LHS132	M8	2600	—	5.0	—	17.14	13.83	11.13	10.48	10.07
2MASSJ22062280-2047058	M8	2600	—	5.0	—	18.93	15.09	12.37	11.69	11.31
2MASSJ22264440-7503425	M8	2600	—	5.0	—	18.95	15.20	12.35	11.70	11.25
2MASSJ04103617-1459269	M8.5	2500	—	5.5	—	—	16.68	13.94	13.24	12.81
2MASSJ05084947-1647167	M8.5	2500	—	5.5	—	—	16.46	13.69	12.96	12.53
2MASSJ04362788-4114465	M8.5	2500	—	5.5	—	19.96	16.04	13.10	12.43	12.05
2MASSJ10481463-3956062	M9	2500	—	5.5	—	15.93	12.67	9.54	8.90	8.45
2MASSJ20450238-6332066	M9.5	2500	—	5.5	—	19.24	16.05	12.62	11.81	11.21
2MASSJ09532126-1014205	M9.5	2500	—	5.5	—	19.58	16.82	13.47	12.64	12.14

[a] Saturation in NIR bands.

[b] $T_{\rm eff}$ from Casagrande et al. (2008).

Table 5.2 – Observable and physical quantities for our sample of stars observed at SSO.

Name	Spectral Type	$T_{\rm eff}$ (K)	$T_{\rm eff}$ [b] (K)	log g (cms^{-2})	V	R	I	J	H	K
HIP49986	M1.5	3700	3445	5.0	9.07	8.21	7.08	5.89	5.26	5.01
HIP82256	M1.5	3700	3470	5.0	11.38	10.39	9.24	8.04	7.48	7.22
HIP56528	M1.5	3600	3472	5.0	9.81	8.85	7.66	6.47	5.86	5.62
NLTT19190	M1.5	3600	3456	5.0	11.49	10.57	9.34	8.11	7.47	7.20
NLTT42523	M2	3600	3444	5.0	12.08	11.06	9.81	8.60	8.01	7.80
HIP80229	M2	3600	3486	5.0	11.91	10.90	9.65	8.48	7.87	7.64
LP725-25	M2	3600	3476	5.0	11.76	10.82	9.59	8.36	7.68	7.44
HIP61413	M2	3500	3454	5.0	11.49	10.48	9.17	7.99	7.37	7.15
LP853-34	M2	3500	3339	5.0	12.32	11.31	9.99	8.69	8.10	7.83
LP859-11	M2	3500	3433	5.0	12.00	10.97	9.69	8.49	7.88	7.63
LP788-49	M2	3500	3356	5.0	11.81	10.85	9.55	8.30	7.74	7.49
HIP42762	M2	3500	3302	5.0	11.75	10.76	9.42	8.12	7.49	7.28
HIP51317	M2	3500	3403	5.0	9.67	8.67	7.34	6.18	5.60	5.31
HIP60559	M2	3500	3382	5.0	11.30	10.29	8.99	7.73	7.25	6.95
HIP47103	M2	3500	3319	5.0	10.87	9.89	8.58	7.34	6.74	6.47
HIP93206	M2.5	3500	3366	5.0	11.23	10.18	8.80	7.52	6.93	6.70
LP834-3	M2.5	3500	—	5.0	—	—	—	—	—	—
HIP84521	M2.5	3500	3345	5.0	11.57	10.53	9.22	7.93	7.39	7.11
HIP91430	M2.5	3500	3352	5.0	11.32	10.26	8.92	7.66	7.06	6.85
HIP50341	M2.5	3500	3314	5.0	11.02	10.01	8.62	7.32	6.71	6.45
LP672-2	M2.5	3400	—	5.0	12.58	11.54	10.12	8.80	8.14	7.93
NLTT24892	M2.5	3400	3244	5.0	12.52	11.47	10.05	8.73	8.118	7.84
NLTT34577	M2.5	3400	3254	5.0	12.44	11.40	9.99	8.64	8.00	7.80
LP670-17	M3	3400	3226	5.0	12.14	11.08	9.63	8.28	7.68	7.39
HIP59406	M3	3400	3226	5.0	11.75	10.69	9.25	7.89	7.36	7.04
HIP74190	M3	3400	3258	5.0	11.55	10.48	9.05	7.72	7.13	6.86

[a] Saturation in NIR bands.

[b] $T_{\rm eff}$ from Casagrande et al. (2008).

Table 5.2 Continued.

Name	Spectral Type	$T_{\rm eff}$ (K)	$T_{\rm eff}$ [b] (K)	log g (cms^{-2})	V	R	I	J	H	K
NLTT46868	M3.5	3400	3221	5.0	12.23	11.08	9.61	8.26	7.73	7.44
HIP62452	M4	3300	3095	5.0	11.46	10.31	8.71	7.19	6.67	6.36
NLTT25488	M4	3200	2986	5.0	15.66	14.46	12.73	11.09	10.52	10.21
NLTT29087	M4	3200	2971	5.0	14.79	13.57	11.84	10.22	9.62	9.35
NLTT29790	M4	3200	2987	5.0	14.73	13.54	11.85	10.22	9.64	9.34
LP734-32	M4	3200	3024	5.0	12.15	10.99	9.35	7.77	7.14	6.86
LP739-2	M4	3100	2939	5.0	14.44	13.18	11.40	9.73	9.17	8.89
LP735-29	M4	3100	2940	5.0	14.18	12.95	11.18	9.52	8.97	8.67
GJ1123	M4	3100	—	5.0	13.14	11.90	10.10	8.33	7.77	7.45
GJ1128	M4	3100	—	5.0	12.66	11.40	9.61	7.95	7.38	7.04
NLTT35266	M4.5	3100	2942	5.0	15.15	13.88	12.05	10.41	9.94	9.66
NLTT41951	M4.5	3100		5.0	15.06	13.77	11.99	10.36	9.80	9.51
NLTT21329	M4.5	3000	2949	5.0	13.75	12.38	10.42	8.60	8.07	7.73
LP732-35	M5	3100	2901	5.0	14.10	12.78	10.94	9.36	8.76	8.49
NLTT18930	M5	3100	2903	5.0	15.34	13.93	12.03	10.31	9.76	9.44
2MASS J14221943-7023371	M5	3000	—	5.0	—	—	—	—	—	—
NLTT22503	M5	3000	2785	5.0	13.66	12.32	10.39	8.50	7.92	7.60
NLTT28797	M5	3000	2826	5.0	15.62	14.24	12.32	10.54	9.99	9.64
NLTT30693	M5.5	3000	2785	5.5	15.32	13.86	11.85	9.95	9.36	9.00
LHS288	M5.5	3000	2770	5.0	13.87	12.42	10.31	8.48	8.05	7.73
GJ551	M5.5	2900	—	5.0	3.63	2.08	5.36	4.83	4.38	—
LHS2502	M6	2900	2468	5.5	19.36	17.54	15.33	12.75	12.07	11.79
NLTT20726	M6.5	2800	2464	5.0	16.11	14.24	11.85	9.44	8.84	8.44
GJ406	M6.5	2800	—	5.5	13.57	11.81	9.51	7.08	6.48	6.08
LHS2351	M7	2800	2346	5.5	19.22	17.39	14.91	12.33	11.72	11.33
SCR J1546-5534	M7.5	2700	—	5.5	—	—	—	—	—	—
GJ752b	M8	2700	—	5.5	5.01	—	—	9.91	9.23	8.76
GJ644c	M7	2700	—	5.5	16.90	14.78	12.24	9.78	9.20	8.82
LHS2397a	M8	2700	—	5.5	19.66	17.42	14.86	11.93	11.23	10.73

[a] Saturation in NIR bands.

[b] $T_{\rm eff}$ from Casagrande et al. (2008).

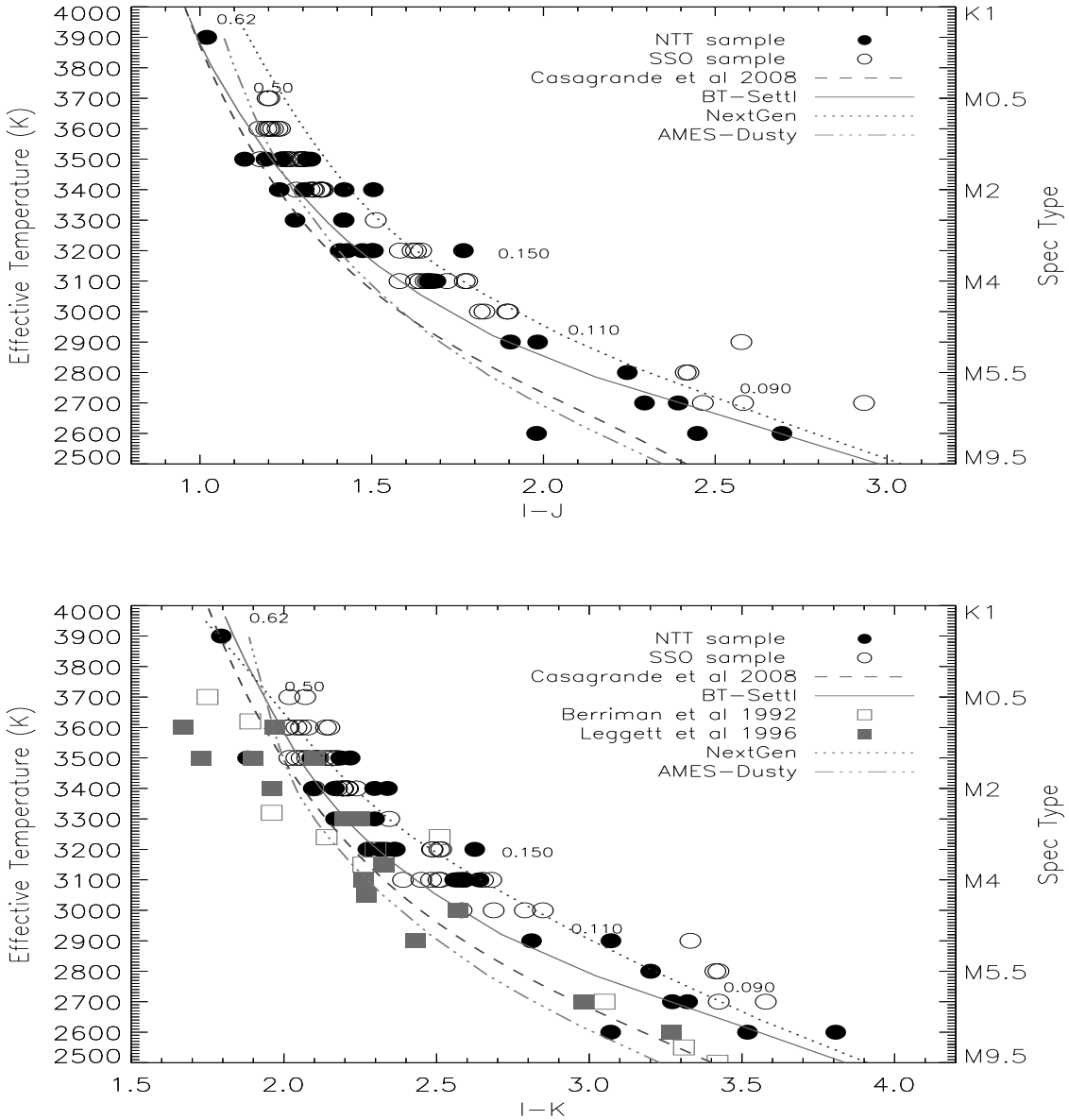

Figure 5.7 – Continued.

Chapter 6

High resolution spectroscopy of M subdwarfs: Effective temperature and metallicity

6.1 Introduction

M subdwarfs are metal poor, low-luminosity dwarfs. Very few are known and as a result the bottom of the main sequence is very poorly constrained for metal poor stars. Making spectroscopic studies of sdM at high resolution has proven to be a difficult task. In the low-temperature regime occupied by these stars, the optical spectrum is covered by a forest of molecular lines, hiding or blending with most of the atomic lines used in spectral analysis. However, over the last decade, stellar atmosphere models of very low mass stars have made great progresses exploring metallicity effects (Allard et al. 2011, 2012a). One of the most important recent improvement is the revision of the solar abundances (Asplund et al. 2009; Caffau et al. 2011)

Rapid progress in the investigation of cool atmospheres is expected thanks to the advent of 10 m class telescopes that allow high resolution spectroscopy of these faint targets. In high resolution spectra, several features are available to constrain several atmospheric parameters simultaneously. Thus, the determination of gravity from the pressure broadened wings can be expected to be much more accurate than by comparing colour ratios from low resolution spectra. Particularly for ultra-cool atmospheres, it is necessary to achieve a very good fit for all important absorbers in order to determine atmospheric properties, because the chemical complexity of these atmospheres reacts very sensitively to changes in the amount of any of its constituents. Descriptions of these stars therefore need validations by comparisons with high resolution spectroscopic observations.

Measuring metallicities for M dwarfs is also challenging. With decreasing temperature, the spectra show increasingly abundant diatomic and triatomic molecules (TiO, VO, H_2O, CO,

FeH, CrH). The TiO and H_2O bands have complex and extensive absorption band structures, creating a pseudo-continuum, letting through only the strongest, often resonance, atomic lines. However, recent advances in model atmospheres for low-mass dwarf stars have boosted the number of studies which derive accurate metallicities for M dwarfs. Metallicities have recently been obtained using high resolution spectra to measure equivalent widths of atomic lines in spectral regions less dominated by discrete molecular bands (Woolf & Wallerstein 2005; Woolf et al. 2009; Bean et al. 2006a,b). Metallicities have also been obtained by observing visual binaries that contain both an M-dwarf and a solar-type star. Assuming that they share a common metallicity that reflects the composition of the molecular cloud in which they were formed, the metallicity is measured on the much better understood spectrum of the solar-type star in order to infer the metallicity of the M dwarf (Bonfils et al. 2005; Bean et al. 2006a,b). These results, together with the abundances obtained from M-dwarf high resolution spectra, are combined to calibrate M-dwarf metallicities using photometry or molecular indices (Bonfils et al. 2005; Woolf et al. 2009; Casagrande et al. 2008). Metal poor stars are rare in the solar neighborhood and the current sample of local subdwarfs is very limited. High resolution spectra of M dwarfs were shown by Tinney & Reid (1998) over the full optical range but such observations are not available for the M subdwarfs over the whole temperature sequence.

In this chapter we present the first high resolution optical atlas of stars covering the whole sdM, esdM and usdM sequence. It consists of 21 sdM, esdM, and usdM at high resolution. Using the most recent PHOENIX BT-Settl stellar model atmosphere we have performed a detailed comparison with our observed spectra using a χ^2 minimization technique. In this study we compare the model spectra with the high resolution spectra of M subdwarf at subsolar metallicities and we assign effective temperatures to M subdwarfs. We derive metallicities based on the best fit of synthetic spectra to the observed spectra and perform a detailed comparison of lines profile of individual elements such as Fe I, Ca II, Ti I, Na.

6.2 A high resolution spectral atlas of M subdwarfs

High resolution spectra are a very important tool to understand the physics of stars. The identification of atomic and molecular absorptions features in the spectra of M subdwarfs is important as they can be used to constrained the stellar parameters $T_{\rm eff}$, $\log g$, [Fe/H]. The determination of gravity and its effect on the pressure dependent wings of the saturated atomic absorption lines (predominantly of the alkali elements) is expected to be much more accurate than comparing colour ratios from low resolution spectra (Reiners et al. 2007a). We present a high resolution spectral atlas of 21 very low mass objects over the entire M subdwarf spectral range, including extreme and ultra subdwarfs. The name, spectral type, and near-infared photometry of these objects are given in Table 6.1. The photometry comes from the Two Micron All Sky Survey (2MASS, Skrutskie et al. 2006). The spectral indices are found in the literature.

6.2.1 Observation and data reduction

The observation were carried out in visitor mode during April and September 2011 with the optical spectrometer UVES (Dekker et al. 2000) on the Very Large Telescope (VLT) at the European Southern Observatory (ESO) in Paranal, Chile. In total 21 targets were observed during period 87. UVES was operated in dichroic mode using red arm with non-standard setting centered at 830 nm. This setting covers the wavelength range 6400 Å-9000 Å, which contains various atomic lines like Fe I, Ti I, K II, Na I and Ca II and is very useful for the spectral synthesis analysis. Between the two CCDs of the red arm, the spectra have a gap from 8200Å to 8370Å. The Na doublet at 8190Å lies just blueward of the gap. The spectra were taken at a slit width of 1.0" yielding a resolving power of R = $\lambda/\Delta\lambda$ = 40 000. The signal to noise ratio (SNR) varies over the wavelength region according to the object's spectral energy distribution and detector efficiency. It reaches 30 in most of the spectral region so that the dense molecular and atomic absorption features are well discernible from noise. Data were reduced using the ESO based pipeline called REFLEX for UVES data.

The spectra are shown in Fig. 6.1 for the sdM sequence, and in Fig. 6.2 for the esdM and usdM targets. The spectra shown have not been corrected for terrestrial absorption by O_3 and H_2O. The O_3 features are quite regular and straightforward to disentangle from features in the stars themselves. This is not true for H_2O absorption, which is complex and irregular. We therefore show in the upper panels the spectrum of the reference star EG 21 where telluric absorptions appear. The main molecular and atomic features expected in the M subdwarfs are labelled in Fig.6.1 and Fig. 6.2

6.2.2 Molecular features

The optical spectra are dominated by molecular absorption bands from metal oxide species such as titanium oxide (TiO), vanadium oxide (VO), hydrides like CaH and H_2O. They are the most important opacity sources. However, due to the low metallicity of subdwarfs, they are TiO depleted. The primary effects are the strengthening of hydride bands and collision induced absorption (CIA) by H_2, and the broadening of atomic lines. Unlike TiO, which produces distinctive band heads degraded on the red, VO produces more diffuse absorption. CaH hydride bands are important opacity source but decrease in relative strength and become saturated with decreasing temperature.

6.2.3 Atomic lines

All the observed M subdwarfs show strong alkali lines in the observed wavelength range. They are massively pressure broadened. Atomic features such as Ca II, K I, Rb I, Na I, Ti I, Mg I are visible throughout M subdwarfs spectral sequence. Na I, K I, Ca II, Ti I, and Mg I lines

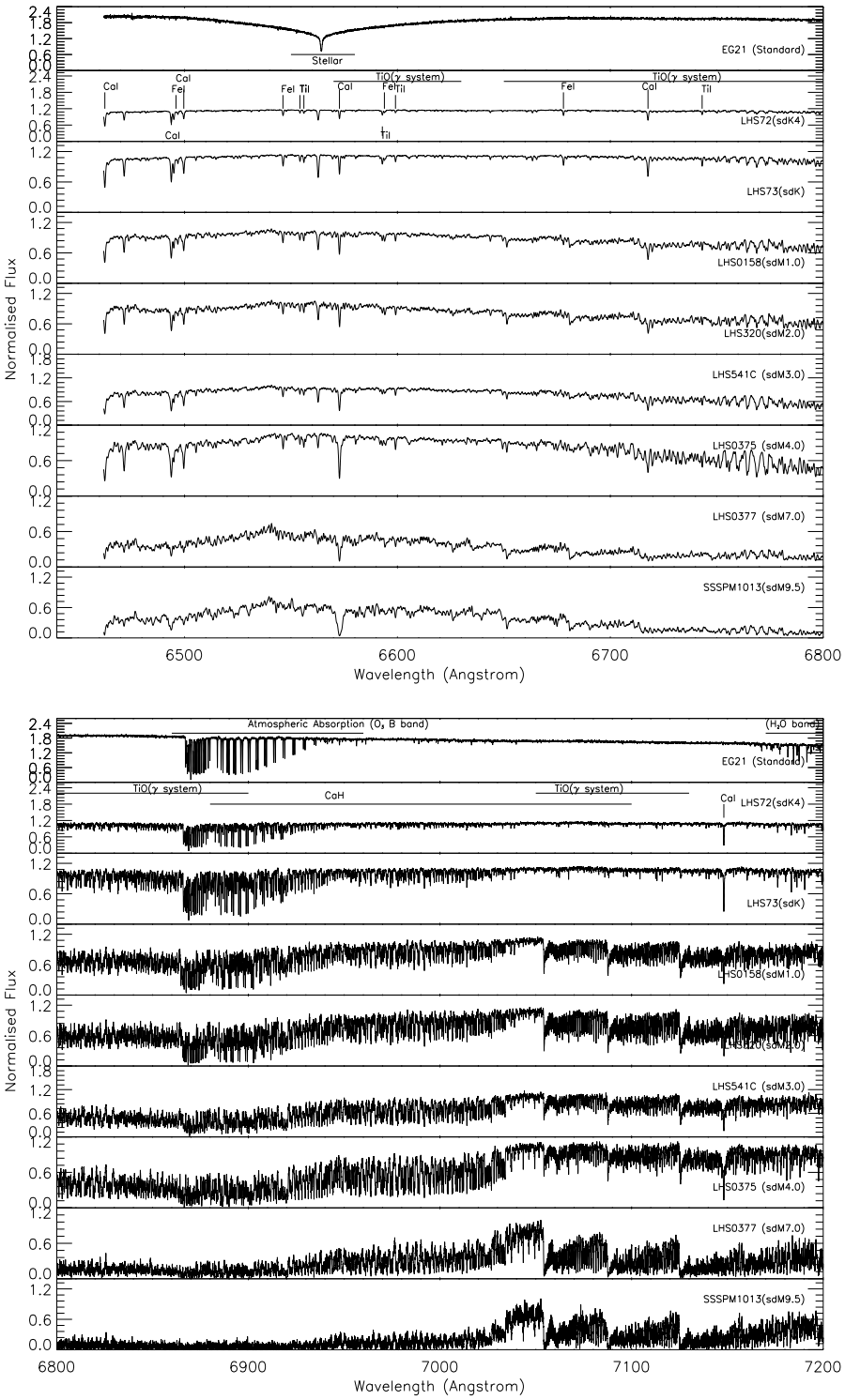

Figure 6.1 – UVES spectra over the sdM spectral sequence.The spectra are scaled to normalize the average flux to unity. The spectrum of the standard star EG 21 shows the location of telluric atmospheric features.

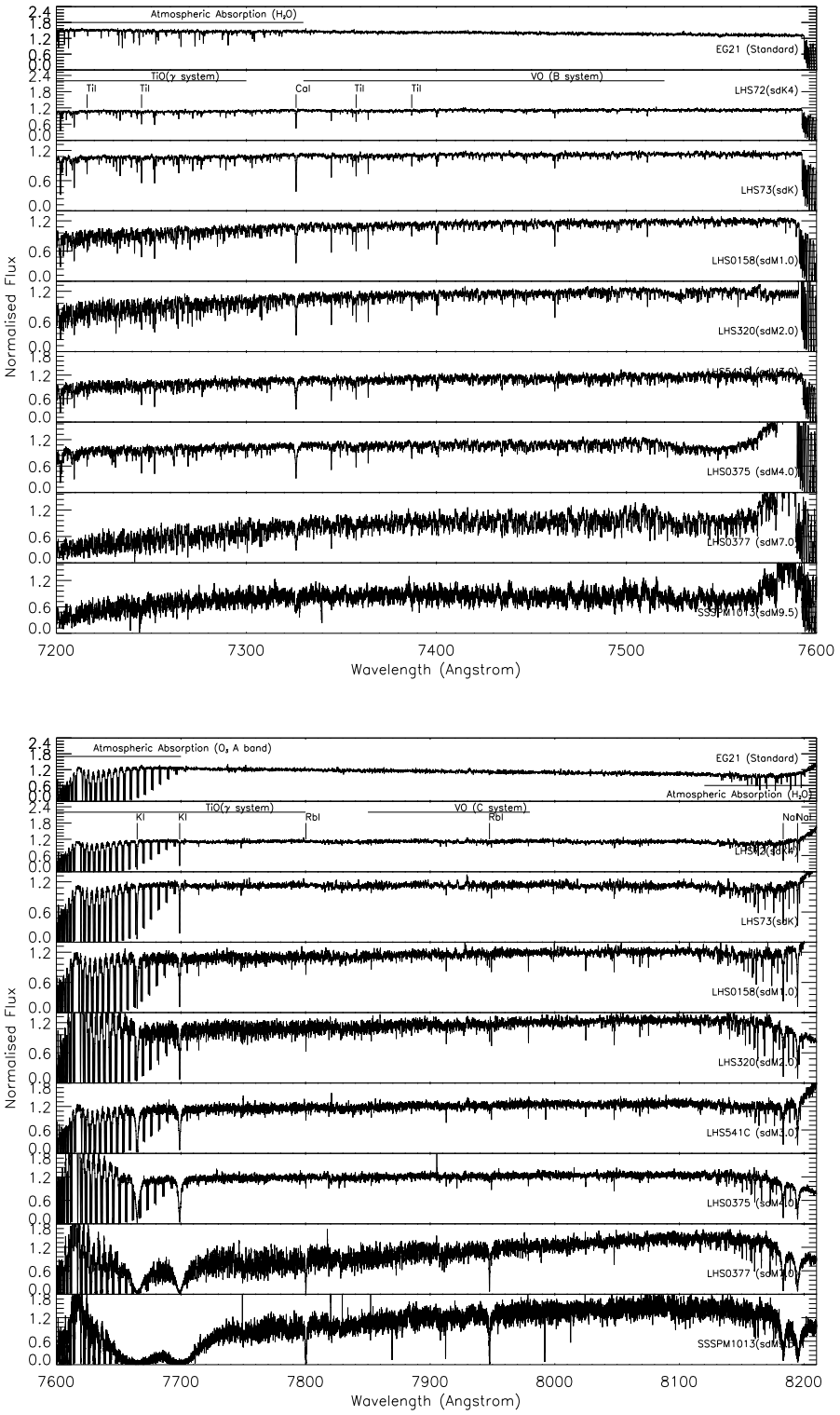

Figure 6.1 – Continued.

are prominent in almost all of the spectra; however their measurement is made difficult by the presence of atmospheric absorptions.

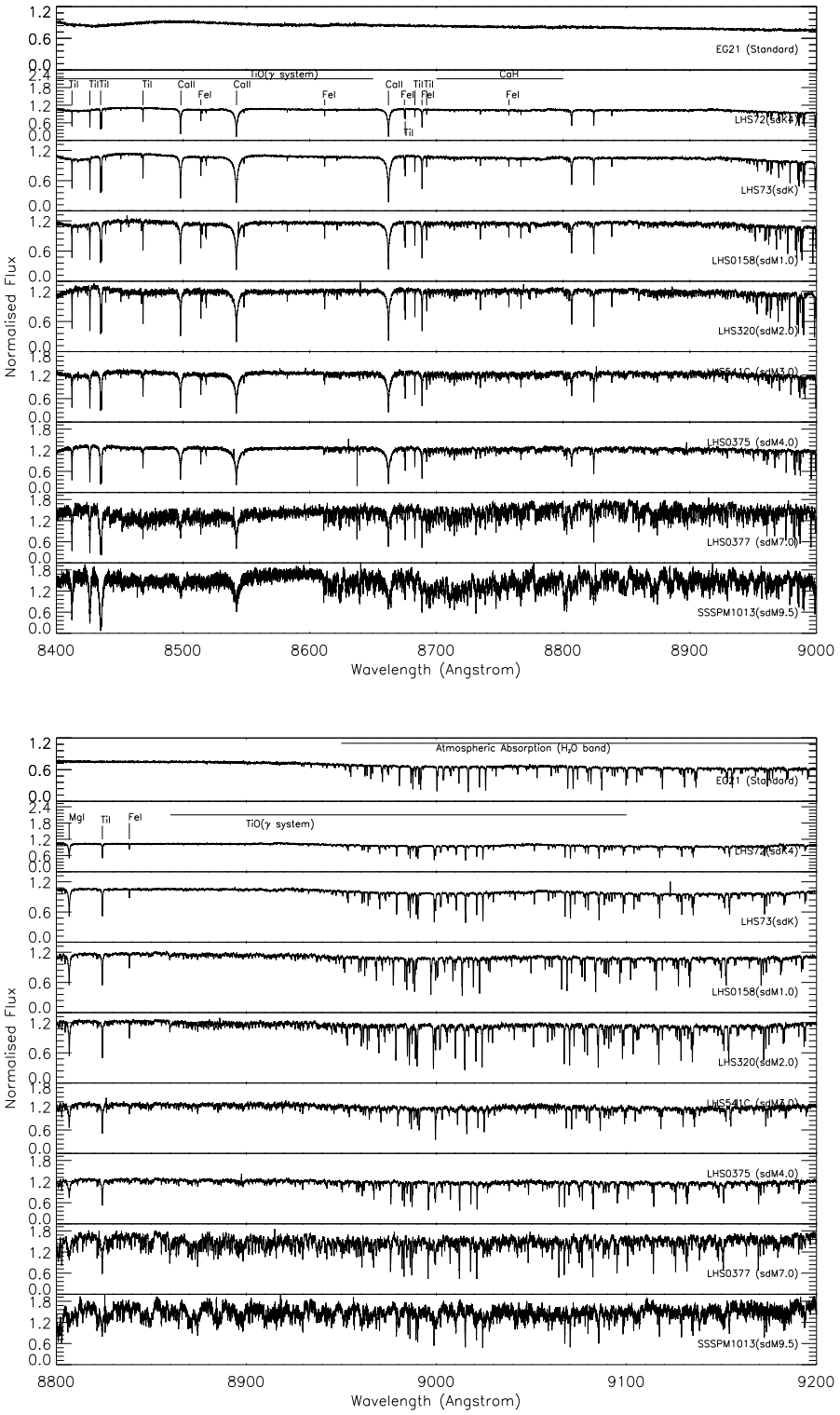

Figure 6.1 – Continued.

The Na I lines at 8183 Å and 8194Å are clearly visible in all the observed spectra and become broadened as one goes from hotter to cooler M subdwarfs. In our setting they appear

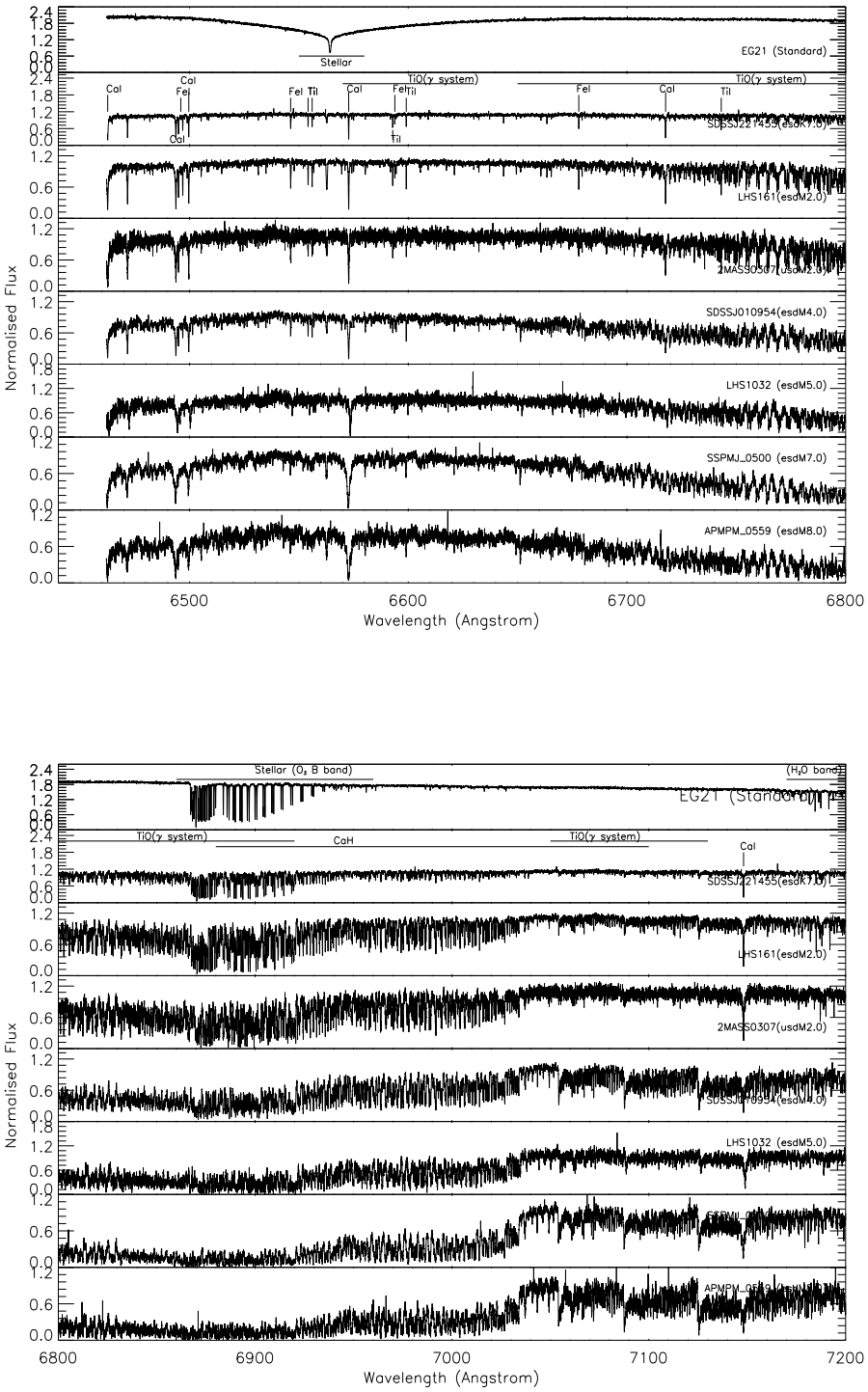

Figure 6.2 – Same as Fig. 6.1 for esdM and usdM stars.

just at the red end of the lower chip of the blue arm. The K I line are very narrow for early type but become very wide and smooth in late type subdwarfs. The K I resonance lines at 7665Å

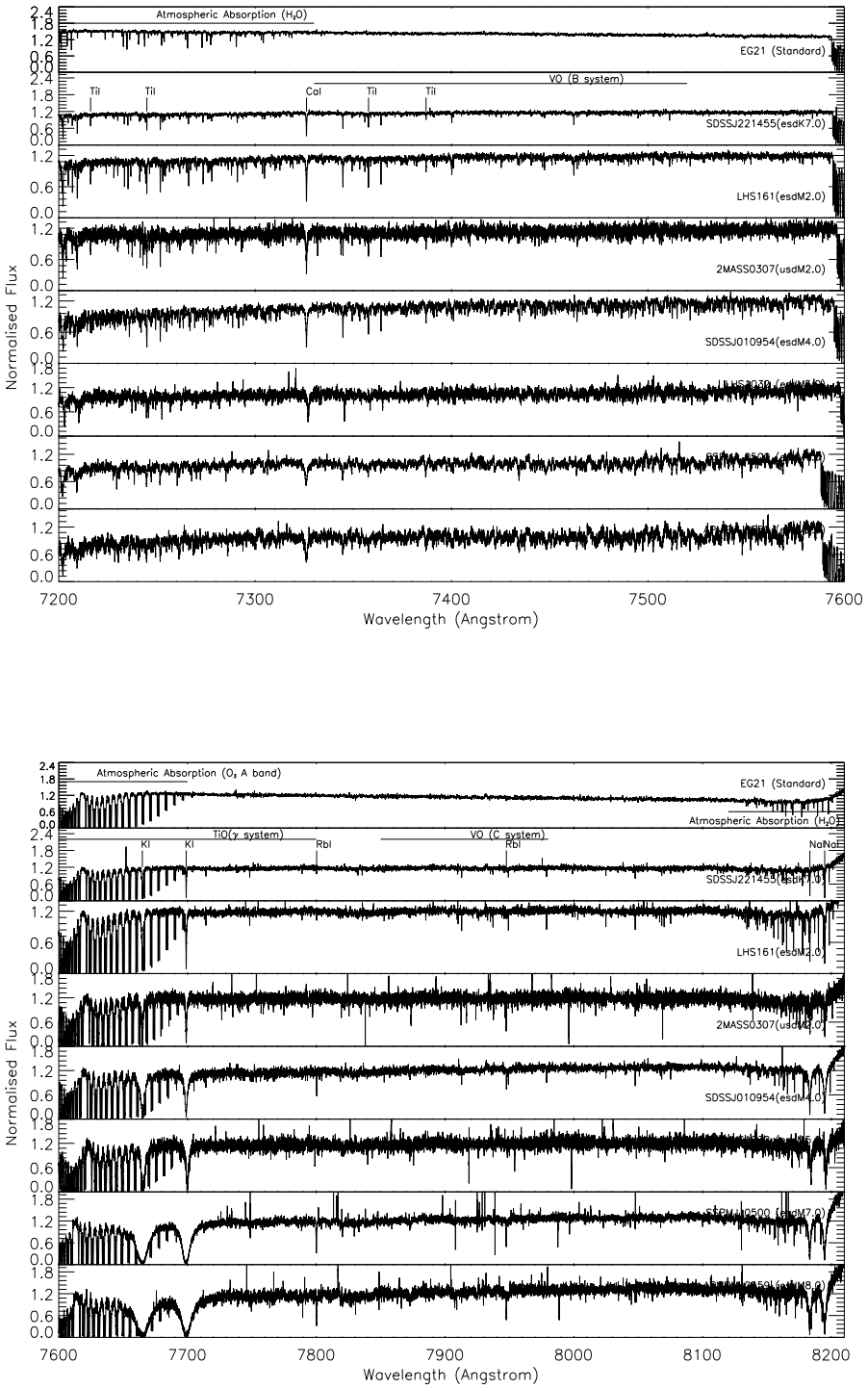

Figure 6.2 – Continued.

and 7698 Å governs the spectral shape of cool subdwarfs spectra. The equivalent width of these K I lines are of several hundred angstroms. The ionized Ca II triplet lines at 8498 Å, 8542 Å,

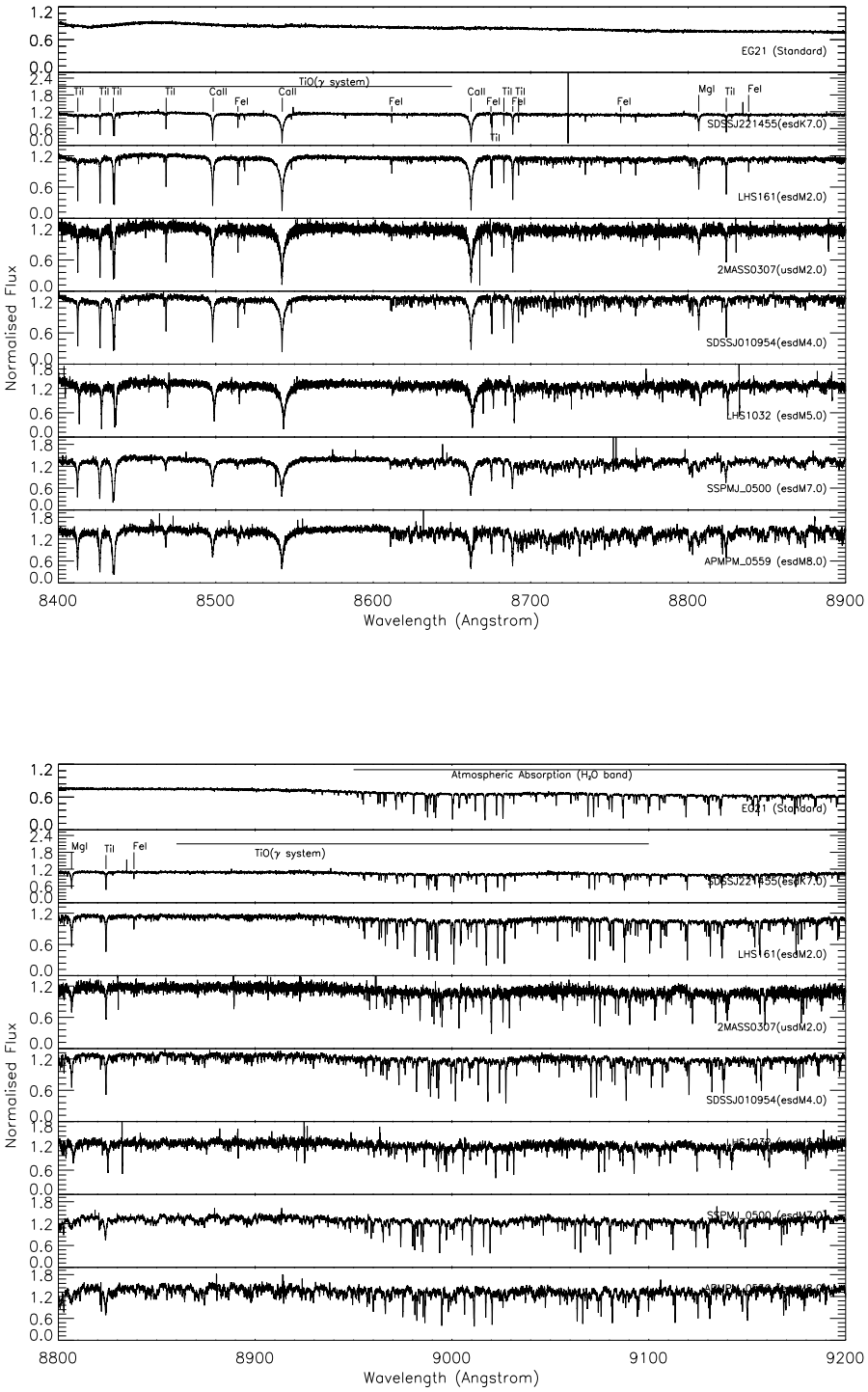

Figure 6.2 – Continued.

8662 Å are very strong in all the observed spectra. Their detailed study by Mallik (1997) shows that their strengths depend on stellar parameters like luminosity, temperature and metallicity.

They are ideal candidates to study their sensitivity to various stellar parameters in cool stars. Although the Ca II triplet lines have lower levels populated radiatively and are not collisions controlled, they have been identified as very good luminosity probes Mallik (1997). They are relatively free from blends and are not contaminated much by telluric lines. On the contrary, the Na I lines at 8183 Å, 8195 Å, which have also been used as luminosity probes in cool stars, have several atmospheric absorption lines in their vicinity (Alloin & Bica 1989; Zhou 1991).

6.3 Model atmospheres

In this study, we use the most recent BT-Settl models partially published in a review by Allard et al. (2012a). These model atmospheres are computed with the PHOENIX multi-purpose atmosphere code version 15.5 (Hauschildt et al. 1997; Allard et al. 2001) solving the radiative transfer in 1D spherical symmetry, with the classical assumptions: hydrostatic equilibrium, convection using the mixing length theory, chemical equilibrium, and a sampling treatment of the opacities. The models use a mixing length as derived by the radiation hydrodynamic hereafter RHD) simulations of (Ludwig et al. 2002, 2006) and (Freytag et al. 2012) and a radius as determined by the (Baraffe et al. 1998a) interior models as a function of the atmospheric parameters ($T_{\rm eff}$, $\log g$, [Fe/H]).

Relative to previous models by Allard et al. (2001), the current version of the BT-Settl model atmosphere is using the BT2 water vapor line list computed by Barber et al. (2006), TiO, VO, CaH line lists by Plez (1998), MgH by (Weck et al. 2003, Story et al. 2003), FeH and CrH by (Dulick et al. 2003, Chowdhury et al. 2006), NH_3 by Yurchenko et al. (2011), CO_2 (Tashkun et al. 2004), and H_2 CIA by Borysow et al. (2001) and Abel et al. (2011), to mention the most important. We use the CO line list by Goorvitch & Chackerian (1994b,d). Detailed profiles for the alkali lines are also used (Allard et al. 2007b). The reference solar elemental abundances used in this version of the BT-Settl models are those defined by Caffau et al. (2011).

In general, the Unsold (1968) approximation is used for the atomic damping constants with a correction factor to the widths of 2.5 for the non-hydrogenic atoms (Valenti & Piskunov 1996). More accurate broadening data for neutral hydrogen collisions by Barklem et al. (2000) have been included for several important atomic transitions such as the alkali, Ca I and Ca II resonance lines. For molecular lines, we have adopted average values (e. g. $\langle \gamma_6^{HIT}(T_0, P_0{}^1)\rangle_{H_2O} = 0.08\ P_{\rm gas}\ [{\rm cm}^{-1}{\rm atm}^{-1}]$ for water vapor lines) from the HITRAN database (Rothman et al. 2009), which are scaled to the local gas pressure and temperature

$$\gamma_6(T) = \langle \gamma_6^{HIT}(T_0, P_0)\rangle \left(\frac{296\,K}{T}\right)^{0.5} \left(\frac{P}{1\ {\rm atm}}\right) \ , \tag{6.1}$$

with a single temperature exponent of 0.5, to be compared to values ranging mainly from 0.3 to 0.6 for water transitions studied by Gamache et al. (1996). The HITRAN database gives widths

[1] Standard temperature 296 K and pressure 1 atm

for broadening in air, but Bailey & Kedziora-Chudczer (2012) find that these agree in general within 10 – 20% with those for broadening by a solar composition hydrogen-helium mixture.

The BT-Settl grid extends from $T_{\rm eff}$ = 300 to 7000 K at a stem of 100 K, log g = 2.5 to 5.5 at a step of 0.5 dex and [M/H]= -2.5 to 0.0 at a step of 0.5 dex accounting for alpha enhancement of 0.2 dex below [M/H]= -0.5 and 0.4 dex below [M/H] = -1.0. We interpolated the grid at every 0.1 dex in log g and metallicity. For more detail of BT-Sett model atmosphere see (Allard et al. 2012a; Rajpurohit et al. 2012b). The synthetic colours and spectra are distributed with a spectral resolution of around R=100000 via the `PHOENIX` web simulator[2].

Fig. 6.3 shows BT-Settl synthetic spectra varying $T_{\rm eff}$ and [Fe/H]. It shows that the oxide bands that dominate in M dwarfs spectra are weaker in the subdwarfs where the hydrides bands dominate(Jao et al. 2008). They have complex and extensive band structures leaving no window for the true continuum and creating pseudo continuum that only let through the strongest, often resonance atomic lines (Allard 1990a; Allard & Hauschildt 1995a). However because of the lower metallicity of subdwarfs, the TiO bands are less strong, and the pseudo-continuum is brighter. This increases the contrast to the other opacities such as hydride bands and atomic lines which feel the higher pressures of the deeper layers where they emerge from. We see therefore these molecular bands with more details and under more extreme gas pressure conditions than for M dwarfs.

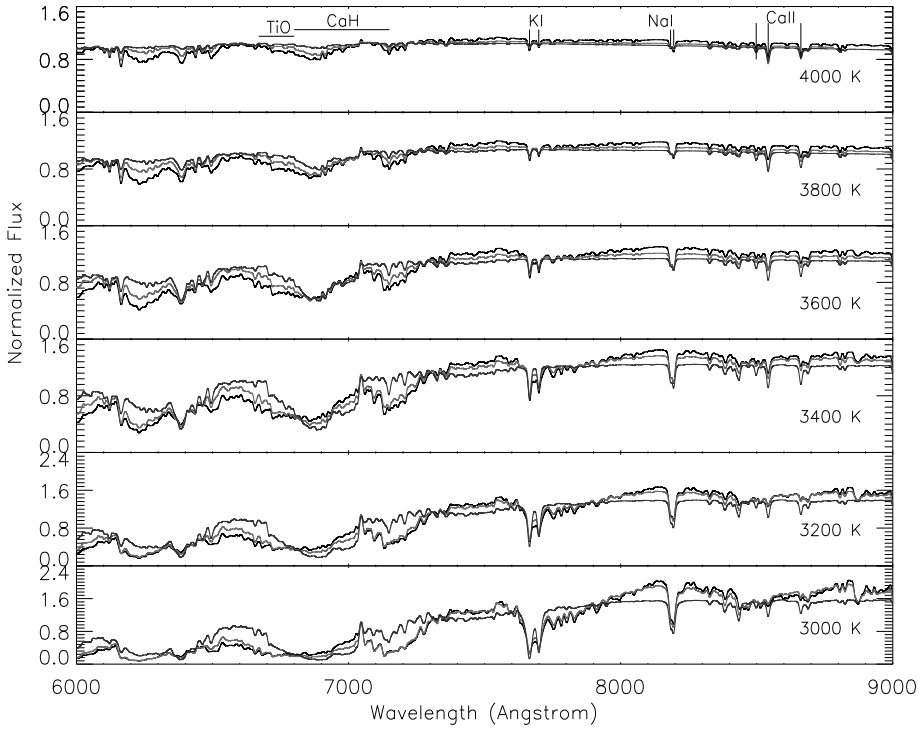

Figure 6.3 – BT-Settl synthetic spectra from 4000 K to 3000 K. The black, red, and blue lines represent [Fe/H] = 0.0, -1.0, and -2.0, respectively.

[2]http://phoenix.ens-lyon.fr/simulator

6.4 Comparison with model atmospheres

We perform a comparison between observed and synthetic spectra computed from the BT Settl model to derive the physical parameters of our sample. Furthermore, the comparison with observed spectra is very crucial to reveal the inaccuracy or incompleteness of the opacities used in the model. Fig. 6.4 and 6.5 shows the comparison of the best fit model for sdM1 and esdM3.5 stars.

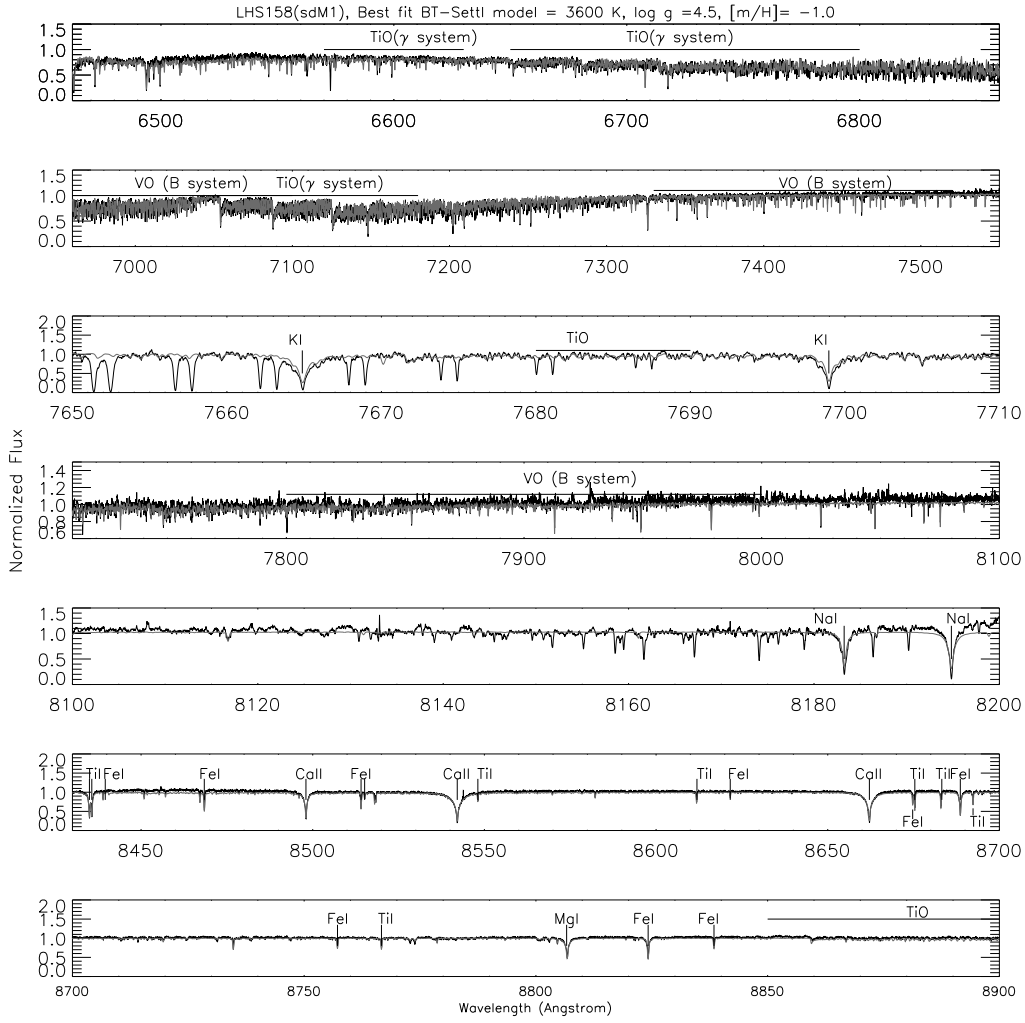

Figure 6.4 – UVES spectra of the sdM1 star LHS 158 (black) compared to the best fit BT-Settl synthetic spectra (red).

6.4.1 Molecular bands

The spectra are in good general agreement, and able to reproduce the specific strengths of the TiO band heads at 6600 Å, 6700 Å, 7050 Å, 7680 Å, 8859 Å, and VO bands at 7000 Å, 7430 Å,

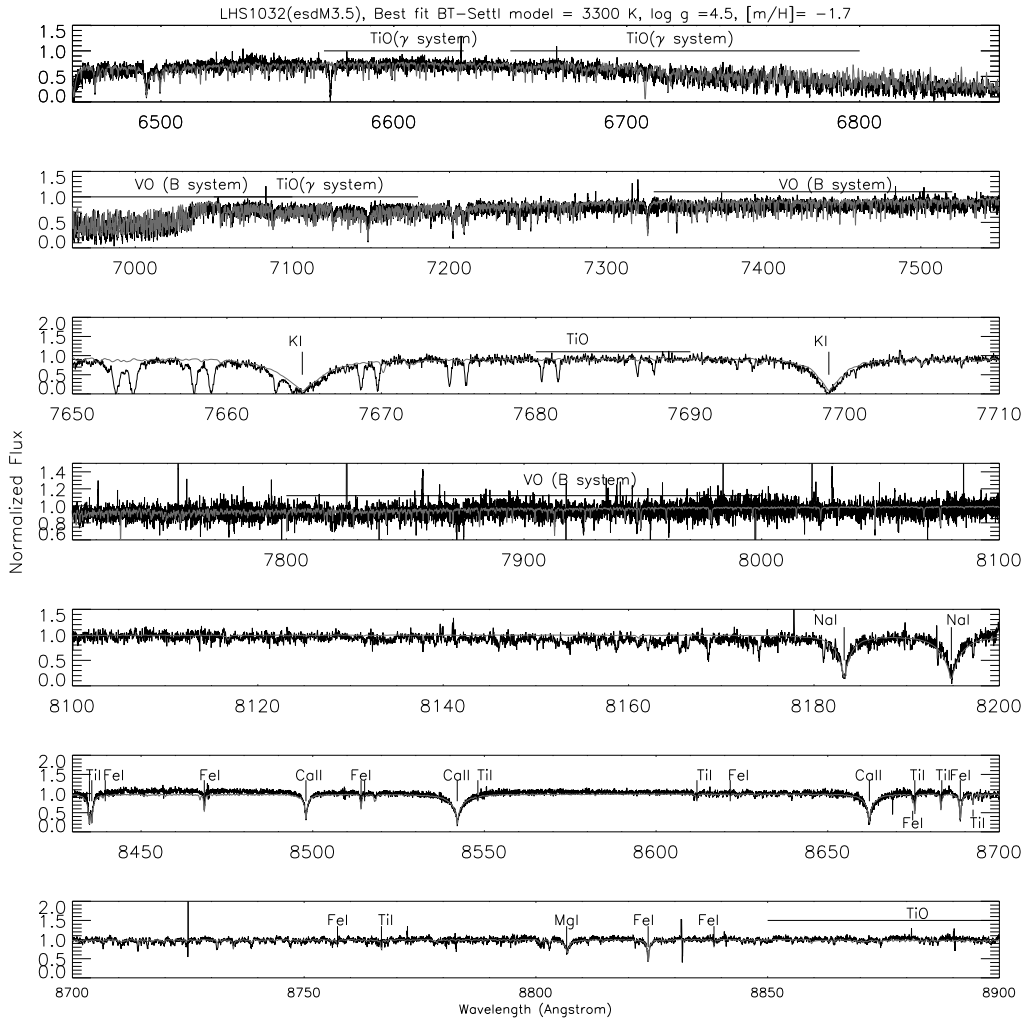

Figure 6.5 – Same as Fig. 6.4 for the esdM3.5 star LHS 1032.

7852 Å. The excellent match between model and observation over entire subdwarfs sequence shows that the high frequency patterns visible at this spectral resolution is the structure of the absorption band and not noise.

6.4.2 Atomic lines

The models predict rather well the shape of the Na I doublet at 8194 Å and 8183 Å but their strength is not very well fitted. In the sdM3.0 and later and in esdM, the observed lines are broader and shallower than those predicted by the models. The qualitative behaviour of the K I doublet at 7665 Å and 7698 Å is well reproduced by the models, especially the strong pressure broadening wings in the early sdM and esdM. In the sdM0, the cores of the observed K lines are still visible as relatively narrow absorption minima embedded in wings extending a few tens to hundred Å. This broader absorption component becomes saturated in sdM7 spectrum. The

models also show this effect but are not able to reproduce it perfectly. This could be an indication (i) that the models do not yet produce correct densities of the neutral alkali metals in the uppermost part of the atmosphere, since the central parts of the lines form in the highest layers of the atmosphere, especially in the early sdM and esdM where alkali metals are not depleted strongly (Johnas et al. 2007), or (ii) that the depth of atomic lines can only be reproduced when accounting for a magnetic field and Zeeman broadening (C. Deen, private communication). The models reproduce the strength and wings of Ca II triplet lines at 8498 Å, 8542 Å, 8662 Å very well. We also have a good fit to the Ti I lines. They are located between 8400 Å to 9700 Å and belong to low energy transition that appears to be visible in such cool atmospheres (see also Reiners & Basri 2006b). Absorption lines of Rb appear in spectra later then sdM7.0. They become stronger and wider towards lower temperature. Given the fact that they are embedded in pseudo-continua that are not always a good fit to the data, the behavior of the two Rb lines at 7800 Å and 7948 Å is very well reproduced by the models.

6.4.3 Stellar parameters determination

The analysis using synthetic spectra requires the specification of several inputs parameters: effective temperature, surface gravity and the overall metallicity [Fe/H] compared to Sun. As opposed to previous studies in which the best fit was found by trial and error, in this paper we derive the effective temperature by performing a χ^2 minimization technique. For this purpose, our approach was to first convolve the synthetic spectrum with a Gaussian kernel using equation 7.1 at the observed resolution and then interpolate the outcome with the observation. For each of the observed spectra we then calculated the χ^2 by comparing the observed spectra with the grid of synthetic spectra in the wavelength range 6400Å to 9000Å using equation 7.3 as explained in Apendix. The sum were calculated over the entire spectral range excluding the spectral region between 6860 to 6960 Å, 7550 to 7650 Å, and 8200 to 8430 Å, due to presence of atmospheric absorption. In the first step, we let all the stellar parameters ($T_{\rm eff}$, [Fe/H], $\log g$) go free. In order to determine $T_{\rm eff}$ we compare the observed high-resolution line profiles of various temperature sensitive species to synthetic spectra. Specifically, we examine the the highly temperature-sensitive triple-headed band of titanium oxide (TiO) at 6600Å, 6700Å and 7100Å. This TiO system is highly sensitive to $T_{\rm eff}$ (increasing in strength with decreasing $T_{\rm eff}$) and rather insensitive to variations in gravity. At a given $T_{\rm eff}$, the band strengths change only slightly even for a large, 1 dex change in gravity (in the $\log g$ 4.5-5.5 range expected for low-mass). At a given gravity, however, they vary significantly over only 100 K changes in $T_{\rm eff}$ (specifically, the band heads at 6600Å, 6700Å and 7100Å). This TiO system is thus an excellent temperature indicator.

In second step, a χ^2 map has been obtained for each of the observed spectra as function of temperature and metallicity (Rice et al. 2010). The error bar are derived from standard deviation by taking 5 % from the minimum χ^2 value. The acceptable parameters were finally inspected by comparing it with the observed spectra. The same procedure has been used for all the observed spectra. We found generally good agreement with BT-settl model and conclude that model fitting procedure can be used to estimate the $T_{\rm eff}$ with an uncertainty better than ~100 K. We

tested the sensitivity of the TiO lines to surface gravity and did not find any significant effect in the parameter space and wavelength range relevant to this study. The surface gravity can be determined by analyzing the width of gravity sensitive atomic lines such as K I and Na I doublets (see Fig. 6.6) as well as relative strength of metal hydride bands such as CaH. The K I doublet at 7665 Å, 7699 Å and Na I lines at 8183 Å and 8194Å is a particular useful gravity discriminant for M dwarfs and subdwarfs. The overall line strength (central depth and equivalent width) increases with gravity as the decreasing ionization ratio due to higher electron pressure leaves more neutral alkali lines in the deeper atmosphere. The width of the damping wings in addition increases due to the stronger pressure broadening, mainly by H_2, He and H I collision.

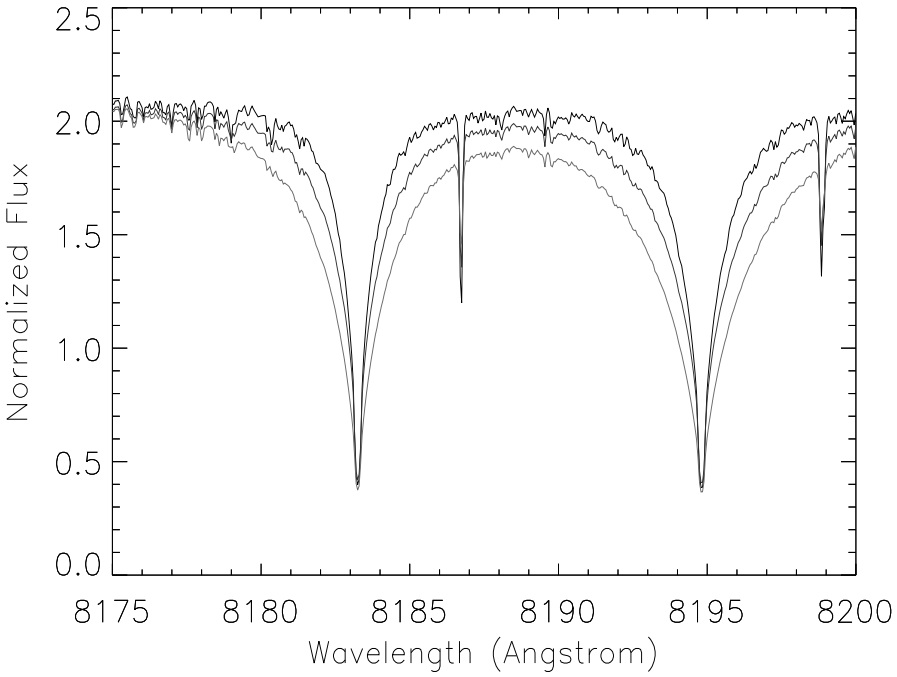

Figure 6.6 – BT-Settl synthetic spectra with $T_{\rm eff}$ of 3500 K and varying $\log g$ =4.5 (black), 5.0 (blue), 5.5 (red). The effect of gravity and pressure broadening on the sodium doublet is clearly visible.

For the metallicity determination we fit the synthetic spectra using the same procedure explained above but on restricted regions where molecular absorptions are less and atomic lines appear clearly. Our first criterion is that the lines must have fractionally small amount of TiO line blending. This necessitate the use of fairly strong lines. The second criterion is that they must also be strong enough in a solar spectrum for the purpose of determining astrophysical values of $\log gf$. Most of the lines we select occupy a short spectral interval from 8440 Å to 8900 Å. In our analysis we also include the new lines of elemental species such as Ca II triplet and Ti lines. In addition to the atomic lines we have also used TiO bandhead around 7088 Å in the analysis of the metallicity determination. The line list used for the metallicity determination are given in Table 6.2.

The best fit parameters ($T_{\rm eff}$, $\log g$, [Fe/H]) are given in Table 6.3. Fig. 6.7 shows the comparison of the best fit model with the observed spectra of the sdM1 star LHS 158. The spectral region used to determine metallicity is shown only.

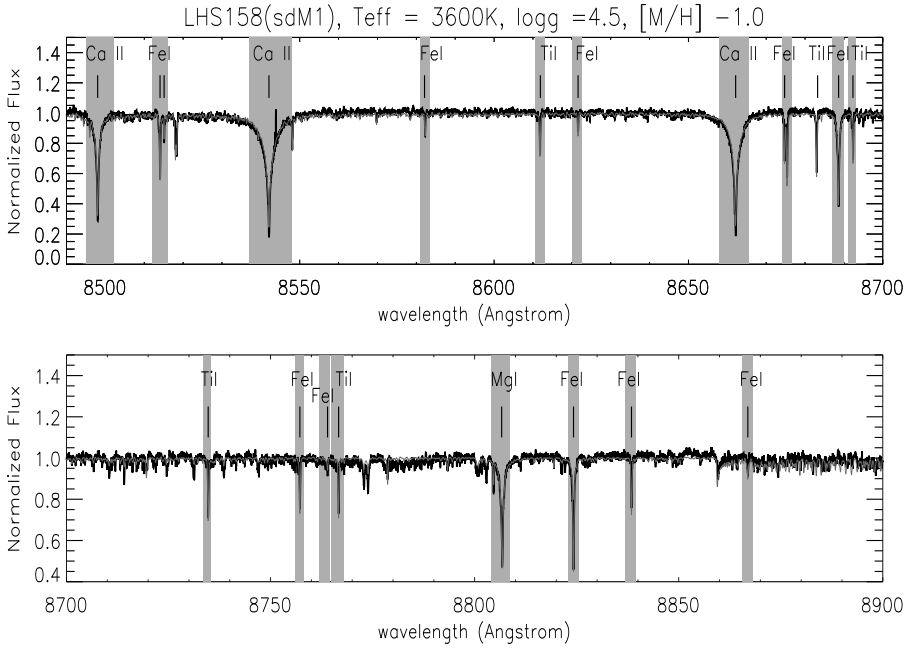

Figure 6.7 – UVES spectrum of the sdM1 star LHS 158 (black) and the best fit BT Settl synthetic spectrum (red). The spectral region used to determine metallicity is shown only. The atomic features used are highlighted.

6.5 Discussion

The effective temperature versus near-infrared colours are shown in Fig. 6.8. The expected relations from evolution models (Baraffe et al. 1998a) assuming an age of 10 Gyrs, and varying metallicities, are also superimposed. The colours stand for different metallicities. The plot shows discrepancies between the models and our observations. It shows that the metallicities determined from the high resolution spectral features are inconsistent with those we would infer from near-infrared colours. This inconsistency may be due to uncertainties in the CIA opacities or due to outdated model interiors. It shows that braodband colours are not sufficient to determine the parameters of M subdwarfs.

The effective temperature versus spectral type relation is shown in Fig. 6.9. The relation determined using UVES sample is compared to the $T_{\rm eff}$ scale of M dwarfs determined by Rajpurohit et al. (2013). $T_{\rm eff}$ of subdwarfs dwarfs is 200-300 K higher than $T_{\rm eff}$ of M dwarfs for the same spectra type except for hot temperature.

This is expected since the TiO bands are depleted with decreasing metallicity, and as a result the pseudo-continuum is brighter and the flux is emitted from the hot deeper layer. A comparison to the earlier work from Gizis (1997) is also shown. Gizis (1997) determined the temperature by comparing the low resolution optical spectra of a sample of sdM and esdM with the NextGen model atmosphere grid by Allard et al. (1997). The $T_{\rm eff}$ scales are in agreement within 100 K. This difference is due to the incompleteness of the TiO and water vapor line lists used in the NextGen model atmospheres compared to the new BT-Settl models. Furthermore this work allows us to extend the relation to the coolest M subdwarfs.

We compile from the literature the spectral indices TiO5, CaH2, and CaH3, computed from TiO and CaH band strengths on low resolution spectra (see table 6.1). Fig 6.10 shows the CaH2+CaH3 versus TiO5 . Lépine et al. (2003b) showed that such a diagram is useful to discriminate between the different object classes, sdM, esdM, and usdM. Our metallicity determinations are labelled in the diagram. It shows that the metallicity is, as expected, getting lower from sdM to usdM stars.

We also derive the ζ parameter as defined by Lépine et al. (2007). This ζ parameter is a combination of the TiO_5, CaH_2 and CaH_3 spectral indices. Woolf et al. (2009) used a sample of M dwarfs and subdwarfs with known metallicity to derive a correlation between ζ and the metallicity, and showed that it can be used as a metallicity indicator. Lépine et al. (2013) also gave a correlation on a sample of M dwarfs having metallicity determinations from Neves et al. (2012); Rojas-Ayala et al. (2012). We plot the metallicity of our stars versus ζ (Fig. 6.11) and superimposed these correlations. We also defined a similar correlation using our sample

$$[Fe/H] = 1.19\zeta - 1.75$$

Contrarily to our correlation computed only on a M subdwarfs sample, Woolf et al. (2009) sample contains many M dwarfs which deviate the relation towards the higher metallicity. Therefore, this work can contribute to refine the relation for subdwarfs.

6.6 Conclusion

We present a high resolution optical spectral atlas for a sample of 21 M subdwarfs. We describe various atomic and molecular features that appear in the spectra and their evolution with decreasing effective temperature and metallicity. We use the most recent BT-Settl model atmospheres, with revised solar abundances, to determine the scaled solar abundances of the subdwarfs. We compare the synthetic spectra produced by the BT-Settl the model atmosphere with observed spectra of subdwarf and derive their fundamental stellar parameter. The accuracy

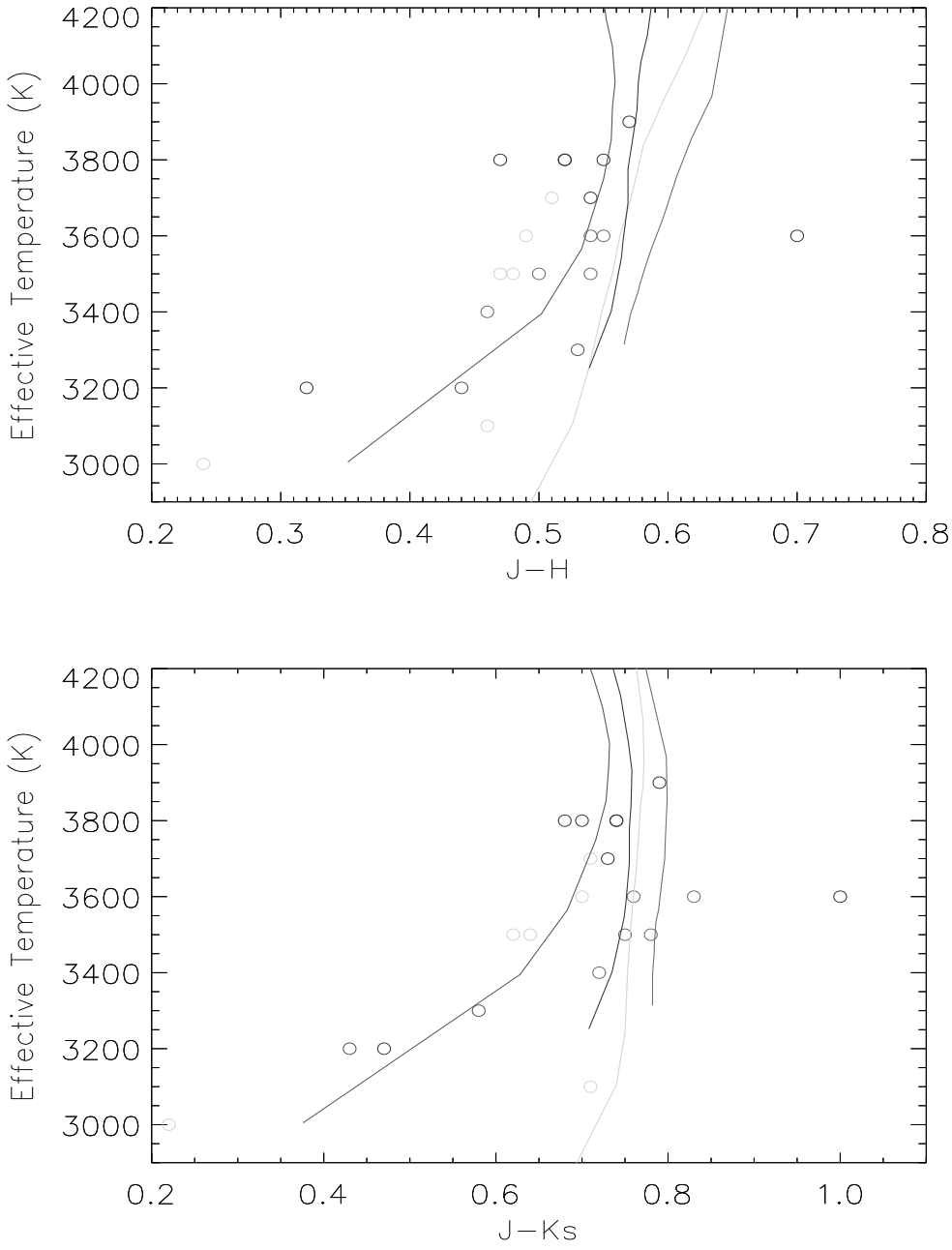

Figure 6.8 – Effective temperature versus near infrared colours of our sample of subdwarfs. The different colours stand for different metallicities: [Fe/H] = −0.5 to −0.7 dex (red), [Fe/H] = −1.0 to −1.2 dex (green), [Fe/H] = −1.3 to −1.6 dex (blue), [Fe/H] = −1.7 dex (brown). The lines are from evolution models from (Baraffe et al. 1998a) at different metallicities (red: −0.5 dex, green: −1.0 dex, blue: −1.5 dex, brown: −2.0 dex) assuming an age of 10 Gyrs.

of the atmospheric models involved in the metallicity determination can be inferred by looking at the fit to the individual atomic and molecular lines. Working with these high resolution

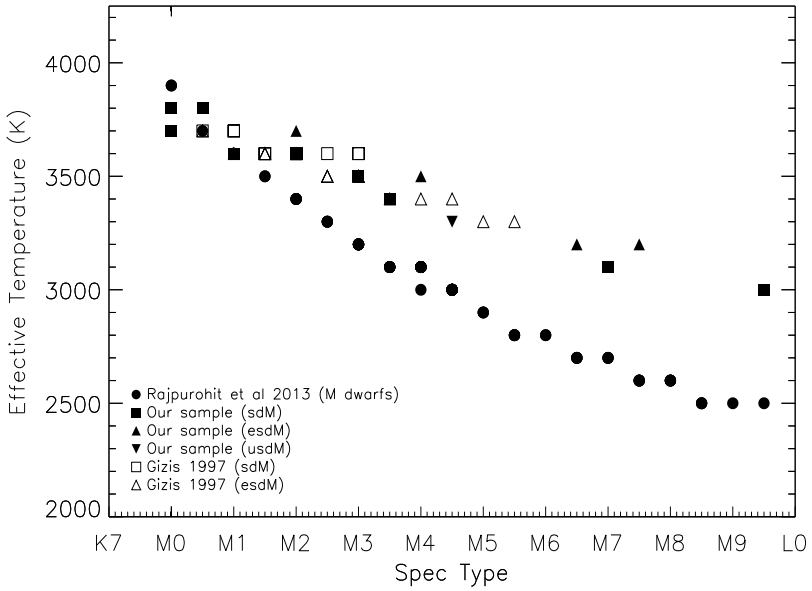

Figure 6.9 – Effective temperature of subdwarfs versus spectral type relation from our sample (filled symbols) compared to the one from Gizis (1997) (open symbols) and to the M dwarfs $T_{\rm eff}$ scale from Rajpurohit et al. (2013) (filled circles).

spectra allowed us to disentangle the atmospheric parameters (effective temperature, gravity, metallicity), which is not possible when using braodband photometry.

We determine an effective temperature versus spectral type relation of M-subdwarfs and compare it to the previous study from Gizis (1997). Our relation is in agreement within 100 K, and extend to the cooler spectral sequence. This work will also contribute to calibrate the relation between metallicity and photometric colours and molecular band strengths. With such a calibration, it will be possible to estimate the metallicity of large sample of subdwarfs, allowing meaningful statistical analysis to be performed.

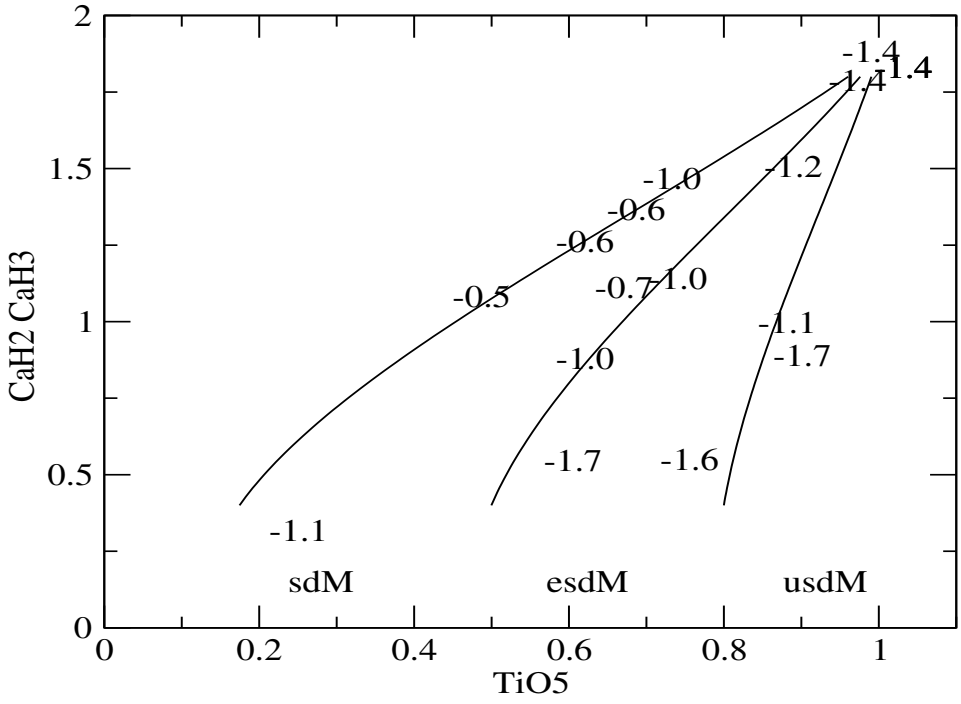

Figure 6.10 – CaH2+CaH3 versus TiO5 diagram for our sample. The labels indicate our metallicity determination. The lines are defined by Lépine et al. (2007). They show the different regions in the diagram where sdM, esdM, and usdM stars are expected.

Table 6.1 – Spectral types, near-infrared photometry, and spectral indices of our sample. The reference for spectral indices measurement are given.

Name	α	δ	SpT	J	H	K	TiO5	CaH2	CaH3	Ref.
LHS 72	23 43 13	−24 09 52	sdK4	9.61	9.04	8.82	–	–	–	–
LHS 73	23 43 15	−24 10 47	sdK7	10.11	9.59	9.37	0.972	0.862	0.927	*a*
G 18-37	22 14 55	+05 42 35	esdK7	12.72	12.20	12.02	–	–	–	–
APMPM J2126-4454	21 26 23	−44 53 40	sdM0	12.65	12.11	11.92	–	–	–	–
LHS 300	11 11 13	−41 05 32	sdM0	10.48	10.01	9.80	1.031	0.886	0.943	*a*
LHS 401	15 39 39	−55 09 10	sdM0.5	10.15	9.60	9.41	0.997	0.911	0.958	*a*
LHS 158	02 42 02	−44 30 58	sdM1	10.43	9.94	9.73	0.732	0.639	0.829	*a*
LHS 320	12 02 33	+08 25 38	sdM2	10.29	9.75	9.46	0.620	0.512	0.751	*b*
LHS 406	15 43 18	−20 15 33	sdM2	9.78	9.23	9.02	0.686	0.576	0.789	*a*
LHS 161	02 52 46	+01 55 44	esdM2	11.71	11.20	11.00	0.889	0.689	0.817	*a*
LP 771-87	03 07 34	−17 36 41	usdM2	15.99	15.29	14.99	–	–	–	–
LHS 541	23 17 05	−13 51 06	sdM3	13.03	12.56	12.41	0.795	0.538	0.701	*c*
LHS 272	09 43 46	−17 47 06	sdM3	9.62	9.12	8.87	0.862	0.527	0.736	*c*
LP 707-15	01 09 54	−10 12 12	esdM3	12.94	12.40	12.16	–	–	–	–
LSR 1755+1648	17 55 33	+16 48 53	sdM3.5	11.35	10.89	10.63	0.486	0.419	0.664	*d*
LHS 375	14 31 38	−25 25 33	esdM4	12.15	11.67	11.51	0.879	0.414	0.583	*a*
LHS 1032	00 11 09	+04 20 18	usdM4.5	14.34	13.81	13.76	0.900	0.350	0.540	*c*
SSSPM J0500-5406	05 00 16	−54 06 39	esdM6.5	14.44	14.12	13.97	0.755	0.220	0.331	*c*
LHS 377	14 39 00	+18 39 38	sdM7	13.19	12.73	12.48	0.620	0.340	0.540	*d*
APMPM J0559-2903	05 58 58	−29 03 26	esdM7	14.89	14.45	14.46	0.604	0.217	0.331	*c*
SSSPM J1013-1356	10 13 07	−13 56 20	sdM9.5	14.62	14.38	14.40	0.248	0.114	0.204	*e*

(*a*) Jao et al. (2008) – (*b*) Gizis (1997) – (*c*) Lépine et al. (2007) – – (*d*) Lépine et al. (2003b) – (*e*) Scholz et al. (2004)

Table 6.2 – Atomic line data.

Wavelength Å
Ca II
8498.02
8542.09
8662.14
Fe I
8514.07
8515.10
8582.10
8621.60
8668.62
8674.74
8757.18
8763.96
8824.22
8838.42
8866.93
Ti
8611.91
8684.23
8692.32
8734.71
8766.68

Table 6.3 – Stellar Parameters of the observed targets.

Target	Spectral Type	$T_{\rm eff}$	$\log g$	[Fe/H]
LHS 72	sdK4	3900 ±23	4.5±0.13	-1.4± 0.27
LHS 73	sdK7	3800 ±39	4.5±0.13	-1.4±0.19
G 18-37	esdK7	3800 ±78	4.5±0.15	-1.3±0.44
APMPM J2126-4454	sdM0	3700 ±49	4.5 ±0.19	-1.3±0.23
LHS 300	sdM0	3800 ±39	4.5±0.17	-1.4±0.24
LHS 401	sdM0.5	3800 ±26	4.5±0.17	-1.4±0.28
LHS 158	sdM1	3600 ±48	4.5±0.17	-1.0±0.3
LHS 320	sdM2	3600 ±59	4.6±0.23	-0.6±0.31
LHS 406	sdM2	3600 ±40	4.7±0.24	-0.6±0.24
LHS 161	esdM2	3700 ±77	4.8±0.30	-1.2±0.36
LP 771-87	usdM2	3600 ±95	4.8±0.31	-1.4±0.52
LHS 541	sdM3	3500 ±76	5.1±0.31	-1.0±0.39
LHS 272	sdM3	3500 ±66	5.2±0.30	-0.7±0.37
LP 707-15	esdM3	3500 ±68	5.5±0.29	-0.5±0.36
LSR J1755+1648	sdM3.5	3400 ±52	5.1±0.31	-0.5±0.33
LHS 375	sdM4	3500 ±79	5.5±0.32	-1.1±0.31
LHS 1032	esdM4.5	3300 ±63	4.5±0.32	-1.7±0.25
SSSPM J0500-5406	esdM6.5	3200±51	5.4±0.31	-1.6±0.16
LHS 377	sdM7	3100 ±32	5.3±0.25	-1.0±0.16
APMPM 0559-2903	esdM7	3200 ±68	5.4±0.34	-1.7±0.25
SSPM J1013-1356	sdM9.5	3000 ±0	5.5±0.05	-1.1±0.16

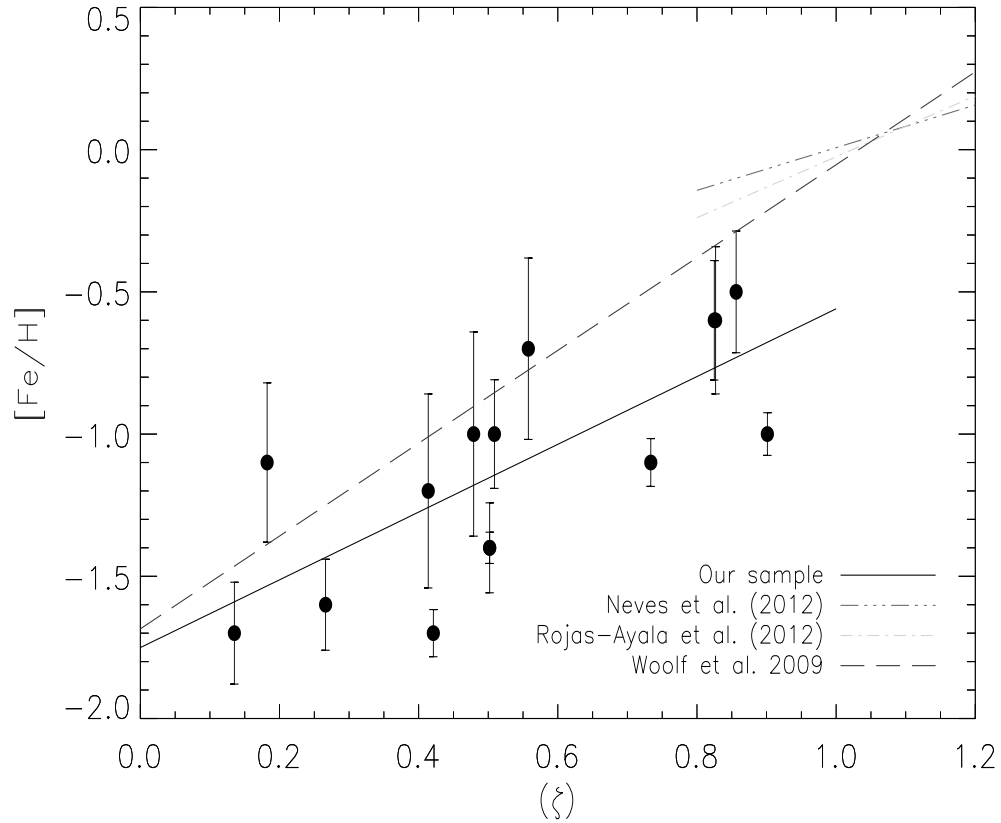

Figure 6.11 – ζ parameter defined by Lépine et al. (2007) vs metallicity diagram. The dots show are sample and the solid black line is the linear-square regression. Other relations from Woolf et al. (2009); Neves et al. (2012); Rojas-Ayala et al. (2012) are superimposed.

Chapter 7

Conclusion and future perspectives

The research contained in this dissertation is primarily focused on the determination of fundamental stellar parameter for M dwarf and subdwarfs based on an analysis of both high and low resolution spectroscopy, and it also set out to test different model atmospheres. I first described the spectral analysis of the LHS1070 triple system by comparing the observed spectra with those predicted by different model atmosphere (BT-Dusty, BT-Settl, DRIFT, MARCS). I have determined the physical parameters $T_{\rm eff}$, log g , metallicity and radius for all the three components of the LHS 1070. A solar metallicity is derived from all three models. The derived gravity differs by 0.5 dex depending on the model used but still agrees within the uncertainties with the values derived from dynamical mass (Seifahrt et al. 2008). We found the same value for $T_{\rm eff}$ for the component A from all models, while differences of 100 K and 200 K are found for component B and C. $T_{\rm eff}$ values found for component B and C are also 200 K higher than those found by Leinert et al. (2000). The main cause of these differences resides in the treatment of dust. Thus the comparison between M-dwarf spectra with different model atmosphere spectra will bring constraints on the physics of these cool objects, in particular on the dust treatment and cloud formation in their atmosphere.

In the second part I have compared the spectra produced by a revised version of the BT-Settl model atmospheres (Allard & Homeier 2012) with the observed NTT and SSO 2.3 m spectra and colours. This study shows that the use of revised TiO line list is very important and provides a more accurate description of the TiO bands in the M dwarfs. The systematic discrepancy between the delta and epsilon bands found by Reiners (2005), which seriously affected the effective temperature determination, is largely alleviated by using the Plez (1998) and B. Plez (private communication) TiO line list although discrepancies remain for the coolest stars. The BT-Settl models reproduce the SED and observed colours across the M dwarfs' spectral regime in unprecedented quality, as well as the colours. The V band is also well reproduced by the models. Discrepancies remain in the strength of some molecular absorption bands while other absorption bands are missing, in particular in the blue spectral region.

We compared our temperature-colour relation to relations using multi-wavelength photom-

etry with the predictions from BT-Settl isochrones, assuming an age of 5 Gyrs. In general, the BT-Settl isochrones are in good agreement with the observed colours, even at temperatures below 2800 K affected by dust treatment in the BT-Settl models. We found that the Casagrande et al. (2008) $T_{\rm eff}$ scale is systematically cooler than the BT-Settl isochrones due, among other things, to the use of the Grevesse et al. (1993) solar elemental abundances adopted in the GAIA-Cond model atmosphere grid used for that work. In contrast the Luhman et al. (2003) $T_{\rm eff}$ scale is progressively too hot towards the bottom of the main sequence. We provide and compare temperature versus colour relations in the optical and infrared, which match well the BT-Settl isochrones and can be further used for large photometric datasets. We determined the effective temperature scale for the M dwarfs in our samples; it extended down to the latest type of M dwarfs, where the dust cloud begins to form in their atmosphere.

In the last part of this thesis I described the effect of metallicity on the spectra of metal-poor M-subdwarfs. We have determine the [Fe/H] abundance for the first time over an entire M-subdwarf spectral sequence based on a careful spectroscopic analysis of 21 high resolution UVES spectra. We have determined an effective temperature versus spectral type relation for M-subdwarfs and have compared it to the previous study of Gizis (1997). The $T_{\rm eff}$ scale are in agreement within 100 K. This work will also contribute to knowledge of the relation between metallicity and photometric colours and molecular band strengths. With such a calibration, it will be possible to estimate the metallicity of a large sample of subdwarfs, allowing meaningful statistical analyses to be performed.

The future perspective of this is study is to determine atmospheric parameters in a precise way. The optical and NIR data is very important simultaneously so that the variability does not include further uncertainty in the estimations of stellar parameter of M dwarfs. This is only possible with the instrument like XSHOOTER that offers this capability. Furthermore, such work will provide an unprecedented atlas over the whole SED of the M-subdwarf sequence. We will use synthetic narrow and intermediate band filters to better determine the pseudo-continuum which is necessary for line-by-line analysis. A detailed comparison of the equivalent widths of the atomic lines in the optical, in the J-band flux peak , and in the CO bands at 2.3 μm between models and observations will be performed to study the effect of metallicity using these features. Besides the overall spectral shape, metallicity sensitive lines such as Fe I, Na I and gravity sensitive lines like Ca I, K I and H-band water bands will be studied and compared. In order to get self-consistent parameters from synthetic spectra one need the combined optical and infrared. Do models predict the same stellar parameters in the Optical and Infrared? How do the models fit the full SED? Do the iron abundances agree when studying different spectral regimes? These important questions can be only addressed by studying in detail large spectral coverages at medium resolution over entire SED.

Publications/Conference Proceedings

- C. Reylé, P. Delorme, E. Artigau, X. Delfosse, L. Albert, T. Forveille, **A. S. Rajpurohit**, F. Allard, D. Homeier, A. C. Robin, A M/T dwarf wide binary from the Canada France Brown Dwarf Survey: a new benchmark brown dwarf at the L/T transition, accepted for publication in Astronomy & Astrophysics, eprint 2013arXiv:1309.1250.

- R. Deshpande, C. H. Blake, C. F. Bender, S. Mahadevan, R. C. Terrien, J. Calberg, G. Zasowski, J. Crepp, **A. S. Rajpurohit**, C. Reylé, D. L. Nidever, C. Allende Prieto, D. Bizyaev, G. Ebelke, S. W. Fleming, J. Ge, F. Hearty, E. Malanushenko, V. Malanushenko, S. R. Majewski, D. Oravetz, K. Pan, R. P. Schiavon, M. Shetrone, A. Simmons, K.G. Stassun, The SDSS-III APOGEE radial velocity survey of M dwarfs I: Description of survey and science goals, Astronomical Journal, eprint 2013arXIV:1307.8121.

- **A. S. Rajpurohit**, C. Reylé, M. Schultheis, F. Allard, , High-resolution spectroscopy of M subdwarf, SF2A-2013, Proceedings of the Annual meeting of the French Society of Astronomy and Astrophysics (submitted).

- **A. S. Rajpurohit**, C. Reylé, M. Schultheis, F. Allard, R. Scholz , D. Homeier, High-resolution spectroscopy of M subdwarf, In Brown Dwarf Come of Age, proceedings of the conference held in Fuerteventura, 20-24 May 2013, 2013 (submitted).

- **Rajpurohit, A. S.**, Reylé, C., Allard, F., Homeier, D., Schultheis, M., Bessell, M. S., Robin, A. C., The effective temperature scale of M dwarfs, 2013A&A...556A..15R.

- Allard, F., Homeier, D., Freytag, B., Schaffenberger, W., **Rajpurohit, A. S.**, Progress in modelling very low mass stars, brown dwarfs, and planetary mass objects, 2013MSAIS..24..128A.

- **Rajpurohit, A. S.**, Reylé, C., Schultheis, M., Allard, F., Scholz, R., Homeier, D., Stellar parameters of M dwarfs from low and high-resolution spectra together with new model atmospheres, SF2A-2012: Proceedings of the Annual meeting of the French Society of Astronomy and Astrophysics. Eds.: S. Boissier, P. de Laverny, N. Nardetto, R. Samadi, D. Valls-Gabaud and H. Wozniak, pp.383-388, 2012sf2a.conf..383R.

- **Rajpurohit, A. S.**; Reylé, C., Schultheis, M., Leinert, Ch., Allard, F., Homeier, D., Ratzka, T., Abraham, P., Moster, B., Witte, S., Ryde, N., The very low mass multiple system LHS 1070. A testbed for model atmospheres for the lower end of the main sequence, 2012A&A...545A..85R

- **Rajpurohit, A. S.**, Reylé, C., Schultheis, M., Leinert, C., Allard, F., The physical parameters of the low-mass multiple system LHS1070 from Spectral synthesis analysis, 2011sf2a.conf..339R.

- Reylé, C., **Rajpurohit, A. S.**, Schultheis, M., Allard, F., 16th Cambridge Workshop on Cool Stars, Stellar Systems, and the Sun. ASP Conference Series, Vol. 448, proceedings of a conference held August 28- September 2, 2010 at the University of Washington, Seattle, Washington. Edited by Christopher M. Johns-Krull, Matthew K. Browning, and Andrew A. West. San Francisco: Astronomical Society of the Pacific, 2012., p.929, 2011ASPC..448..929R.

- **Rajpurohit, A. S.**, Reylé, C., Schultheis, M., Allard, F., Validation of M-dwarf atmosphere models and effective temperature scale of M dwarfs, 2010sf2a.conf..275R.

Apendix

Method and steps of Analysis: In first step, for a given observed spectrum, the model spectra were smoothed to the appropriate resolution using the Gaussian function kernel (equation 7.1) and resampled on the same wavelength grid as the observational data and the spectra were normalized to unit area for scaling.

$$G = \frac{1}{\sqrt{(2\pi\sigma_1)}} e^{-\frac{x^2}{2\sigma_1^2}} \tag{7.1}$$

where σ_1 factor that determines how many points to use for the gaussian kernel. The exact number of points used depends on the value of σ_2 and the range of "x" values as well, but it will be roughly equal to $2(\sigma_1)(\sigma_2)$. Here σ_2 is width of gaussian, in same units as "x".

A well-fitting χ^2 methods results in predicted values close to the observed data values. In second step, the comparison of atmosphere model to the observed spectra were performed using the χ^2 statistics. For each observed spectrum, we extracted the model spectra with minimum value of χ^2 using the procedure describe below. The χ^2 statistics describes the goodness-of-fit of the data to the model. If the observed number in each of the k bins are F(λ_i), and the expected values from the model are M(λ_i), then this statistics is given by the following equations:

$$\chi^2 = \sum_{i=1}^{k} \left(\frac{F(\lambda_i) - M_{[p]}(\lambda_i)}{\sigma_i} \right)^2 \tag{7.2}$$

$$\chi^2 = \sum_{i=1}^{k} \frac{(F(\lambda_i) - M_{[p]}(\lambda_i))^2}{M_{[p]}(\lambda_i)} \tag{7.3}$$

Here, F(λ_i) are the flux of observed spectrum and M(λ_i) is the flux of model spectrum for a model parameter P = [$T_{\rm eff}$, radius, [Fe/H], log g] for equation 7.2 where as for equation 7.3 M(λ_i) is the flux of model spectrum for a model parameter P = [$T_{\rm eff}$ [Fe/H], log g]. The uncertainty σ are the error in the flux as a function of wavelength in observations. This both form was chosen because equation 7.2 put much emphasis on the highest signal-to-noise continuum region while the equation 7.3 places much emphasis on the strongest absorptions. To avoid

problems with low signal-to-noise ratios and/or poor telluric correction, only spectral regions outside the worse telluric absorption windows were used for all the steps described above.

In the third step a χ^2 map has been obtained for each of the individual stars to ensure that we end up in a global minimum when converging to a solution for the best fit. This is similar procedure as adopted by Rice et al. (2010). The "best"' values is always the minimum χ^2 chosen which is then cross checked by visual inspection. The error bar are derived from standard deviation by taking 5 % from the minimum χ^2 value. The acceptable parameters were finally inspected by comparing it with the observed spectra.

Bibliography

Abel, M., Frommhold, L., Li, X., & Hunt, K. L. C. 2011, in 66th International Symposium On Molecular Spectroscopy

Allard, F. 1990a, PhD thesis, PhD thesis. Ruprecht Karls Univ. Heidelberg, (1990)

Allard, F. 1990b, PhD thesis, Ruprecht Karls Univ. Heidelberg

Allard, F., Alexander, D. R., & Hauschildt, P. H. 1998, in Astronomical Society of the Pacific Conference Series, Vol. 154, Cool Stars, Stellar Systems, and the Sun, ed. R. A. Donahue & J. A. Bookbinder, 63–+

Allard, F., Allard, N. F., Homeier, D., et al. 2007a, A&A, 474, L21

Allard, F. & Hauschildt, P. H. 1995a, ApJ, 445, 433

Allard, F. & Hauschildt, P. H. 1995b, ApJ, 445, 433

Allard, F., Hauschildt, P. H., Alexander, D. R., & Starrfield, S. 1997, ARA&A, 35, 137

Allard, F., Hauschildt, P. H., Alexander, D. R., Tamanai, A., & Schweitzer, A. 2001, ApJ, 556, 357

Allard, F., Hauschildt, P. H., Baraffe, I., & Chabrier, G. 1996, ApJ, 465, L123+

Allard, F., Hauschildt, P. H., Miller, S., & Tennyson, J. 1994a, ApJ, 426, L39

Allard, F., Hauschildt, P. H., Miller, S., & Tennyson, J. 1994b, ApJ, 426, L39

Allard, F., Hauschildt, P. H., & Schwenke, D. 2000, ApJ, 540, 1005

Allard, F. & Homeier, D. 2012, ArXiv e-prints

Allard, F., Homeier, D., & Freytag, B. 2010, ArXiv e-prints

Allard, F., Homeier, D., & Freytag, B. 2011, in Astronomical Society of the Pacific Conference Series, Vol. 448, Astronomical Society of the Pacific Conference Series, ed. C. Johns-Krull, M. K. Browning, & A. A. West, 91

Allard, F., Homeier, D., & Freytag, B. 2012a, Royal Society of London Philosophical Transactions Series A, 370, 2765

Allard, F., Homeier, D., Freytag, B., et al. 2013, Memorie della Societa Astronomica Italiana Supplementi, 24, 128

Allard, F., Homeier, D., Freytag, B., & Sharp, C. M. 2012b, in EAS Publications Series, Vol. 57, EAS Publications Series, ed. C. Reylé, C. Charbonnel, & M. Schultheis, 3–43

Allard, N. F., Kielkopf, J. F., & Allard, F. 2007b, European Physical Journal D, 44, 507

Alloin, D. & Bica, E. 1989, A&A, 217, 57

Asplund, M., Grevesse, N., Sauval, A. J., & Scott, P. 2009, ARA&A, 47, 481

Asplund, M., Ludwig, H.-G., Nordlund, Å., & Stein, R. F. 2000, A&A, 359, 669

Asplund, M., Nordlund, Å., Trampedach, R., & Stein, R. F. 1999, A&A, 346, L17

Auman, Jr., J. R. 1969, ApJ, 157, 799

Bailey, J. & Kedziora-Chudczer, L. 2012, MNRAS, 419, 1913

Baraffe, I., Chabrier, G., Allard, F., & Hauschildt, P. H. 1997, A&A, 327, 1054

Baraffe, I., Chabrier, G., Allard, F., & Hauschildt, P. H. 1998a, A&A, 337, 403

Baraffe, I., Chabrier, G., Allard, F., & Hauschildt, P. H. 1998b, A&A, 337, 403

Barber, R. J., Tennyson, J., Harris, G. J., & Tolchenov, R. N. 2006, MNRAS, 368, 1087

Barklem, P. S., Piskunov, N., & O'Mara, B. J. 2000, A&A, 363, 1091

Basri, G. & Marcy, G. W. 1995, AJ, 109, 762

Bean, J. L., Sneden, C., Hauschildt, P. H., Johns-Krull, C. M., & Benedict, G. F. 2006a, ApJ, 652, 1604

Bean, J. L., Sneden, C., Hauschildt, P. H., Johns-Krull, C. M., & Benedict, G. F. 2006b, ApJ, 652, 1604

Berger, E. 2006, ApJ, 648, 629

Berriman, G. & Reid, N. 1987, MNRAS, 227, 315

Berriman, G., Reid, N., & Leggett, S. K. 1992, ApJ, 392, L31

Bessell, M. S. 1991, AJ, 101, 662

Bessell, M. S. 1995, in The Bottom of the Main Sequence - and Beyond, ed. C. G. Tinney, 123

Birkby, J., Nefs, B., Hodgkin, S., et al. 2012, MNRAS, 426, 1507

Blackwell, D. E., Petford, A. D., & Shallis, M. J. 1980, A&A, 82, 249

Blackwell, D. E. & Shallis, M. J. 1977, MNRAS, 180, 177

Blackwell, D. E., Shallis, M. J., & Selby, M. J. 1979, MNRAS, 188, 847

Bochanski, J. J., Hawley, S. L., Covey, K. R., et al. 2007a, in Bulletin of the American Astronomical Society, Vol. 39, American Astronomical Society Meeting Abstracts, 772

Bochanski, J. J., Hawley, S. L., Covey, K. R., et al. 2010, AJ, 139, 2679

Bochanski, J. J., Hawley, S. L., Reid, I. N., et al. 2005, AJ, 130, 1871

Bochanski, J. J., Munn, J. A., Hawley, S. L., et al. 2007b, AJ, 134, 2418

Böhm-Vitense, E. 1958, ZAp, 46, 108

Bonfils, X., Forveille, T., Delfosse, X., et al. 2005, A&A, 443, L15

Bonfils, X., Gillon, M., Udry, S., et al. 2012, ArXiv e-prints

Borysow, A., Jørgensen, U. G., & Fu, Y. 2001, Journal of Quantitative Spectroscopy and Radiative Transfer, 68, 235

Boyajian, T. S., von Braun, K., van Belle, G., et al. 2012, ApJ, 757, 112

Brett, J. M. 1994, VizieR Online Data Catalog, 410, 90263

Brett, J. M. 1995a, A&A, 295, 736

Brett, J. M. 1995b, A&AS, 109, 263

Burgasser, A. J. 2002, PhD thesis, CALIFORNIA INSTITUTE OF TECHNOLOGY

Burgasser, A. J., Kirkpatrick, J. D., Burrows, A., et al. 2003, ApJ, 592, 1186

Burrows, A., Hubbard, W. B., & Lunine, J. I. 1989, ApJ, 345, 939

Burrows, A., Hubbard, W. B., Saumon, D., & Lunine, J. I. 1993, ApJ, 406, 158

Burrows, A., Marley, M., Hubbard, W. B., et al. 1997, ApJ, 491, 856

Burrows, A., Ram, R. S., Bernath, P., Sharp, C. M., & Milsom, J. A. 2002, ApJ, 577, 986

Butler, R. P., Vogt, S. S., Marcy, G. W., et al. 2004, ApJ, 617, 580

Caffau, E., Ludwig, H.-G., Steffen, M., Freytag, B., & Bonifacio, P. 2011, Sol. Phys., 268, 255

Carney, B. W., Latham, D. W., Laird, J. B., & Aguilar, L. A. 1994, AJ, 107, 2240

Casagrande, L., Flynn, C., & Bessell, M. 2008, MNRAS, 389, 585

Casagrande, L., Ramírez, I., Meléndez, J., & Asplund, M. 2012, ApJ, 761, 16

Cesarsky, C. J., Abergel, A., Agnese, P., et al. 1996, A&A, 315, L32

Chabrier, G. 2003, ApJ, 586, L133

Chabrier, G. & Baraffe, I. 1997, A&A, 327, 1039

Chabrier, G., Baraffe, I., Allard, F., & Hauschildt, P. 2000, ApJ, 542, 464

Chabrier, G., Baraffe, I., & Plez, B. 1996, ApJ, 459, L91

Chowdhury, P. K., Merer, A. J., Rixon, S. J., Bernath, P. F., & Ram, R. S. 2006, Physical Chemistry Chemical Physics (Incorporating Faraday Transactions), 8, 822

Cool, A. M., Piotto, G., & King, I. R. 1996, ApJ, 468, 655

Costa, E., Méndez, R. A., Jao, W.-C., et al. 2005, AJ, 130, 337

Coughlin, J. L., López-Morales, M., Harrison, T. E., Ule, N., & Hoffman, D. I. 2011, AJ, 141, 78

Covey, K. R., Hawley, S. L., Bochanski, J. J., et al. 2008, AJ, 136, 1778

Covey, K. R., Lada, C. J., Román-Zúñiga, C., et al. 2010, ApJ, 722, 971

Cram, L. E. & Mullan, D. J. 1985, ApJ, 294, 626

Crifo, F., Phan-Bao, N., Delfosse, X., et al. 2005, A&A, 441, 653

Cruz, K. L. & Reid, I. N. 2002, AJ, 123, 2828

Cushing, M. C., Rayner, J. T., & Vacca, W. D. 2005, ApJ, 623, 1115

Dahn, C. C., Liebert, J., & Harrington, R. S. 1986, AJ, 91, 621

Dantona, F. & Mazzitelli, I. 1985, ApJ, 296, 502

de Jager, C. & Neven, L. 1957, Spectroscopic data for 50 model photospherese, 4

Dehn, M., Helling, C., Woitke, P., & Hauschildt, P. 2007, in IAU Symposium, Vol. 239, IAU Symposium, ed. T. Kuroda, H. Sugama, R. Kanno, & M. Okamoto, 227–229

Dekker, H., D'Odorico, S., Kaufer, A., Delabre, B., & Kotzlowski, H. 2000, in Society of Photo-Optical Instrumentation Engineers (SPIE) Conference Series, Vol. 4008, Society of Photo-Optical Instrumentation Engineers (SPIE) Conference Series, ed. M. Iye & A. F. Moorwood, 534–545

Delfosse, X., Forveille, T., Ségransan, D., et al. 2000, A&A, 364, 217

Delfosse, X., Tinney, C. G., Forveille, T., et al. 1999, A&AS, 135, 41

Digby, A. P., Hambly, N. C., Cooke, J. A., Reid, I. N., & Cannon, R. D. 2003, MNRAS, 344, 583

Dulick, M., Bauschlicher, Jr., C. W., Burrows, A., et al. 2003, ApJ, 594, 651

Epchtein, N. 1997, in Astrophysics and Space Science Library, Vol. 210, The Impact of Large Scale Near-IR Sky Surveys, ed. F. Garzon, N. Epchtein, A. Omont, B. Burton, & P. Persi, 15

Epchtein, N., Deul, E., Derriere, S., et al. 1999, A&A, 349, 236

Fegley, Jr., B. & Lodders, K. 1996, ApJ, 472, L37

Freytag, B., Allard, F., Ludwig, H.-G., Homeier, D., & Steffen, M. 2010, A&A, 513, A19+

Freytag, B., Steffen, M., & Dorch, B. 2002, Astronomische Nachrichten, 323, 213

Freytag, B., Steffen, M., Ludwig, H.-G., et al. 2012, J. Comp. Phys., 231, 919

Gabriel, C., Acosta-Pulido, J., Heinrichsen, I., Morris, H., & Tai, W.-M. 1997, in Astronomical Society of the Pacific Conference Series, Vol. 125, Astronomical Data Analysis Software and Systems VI, ed. G. Hunt & H. Payne, 108

Gamache, R. R., Lynch, R., & Brown, L. R. 1996, J. Quant. Spec. Radiat. Transf., 56, 471

Giampapa, M. S., Worden, S. P., & Linsky, J. L. 1982, ApJ, 258, 740

Gizis, J. E. 1996, in Astronomical Society of the Pacific Conference Series, Vol. 109, Cool Stars, Stellar Systems, and the Sun, ed. R. Pallavicini & A. K. Dupree, 683

Gizis, J. E. 1997, AJ, 113, 806

Gizis, J. E., Reid, I. N., & Hawley, S. L. 2002, AJ, 123, 3356

Golimowski, D. A., Leggett, S. K., Marley, M. S., et al. 2004, AJ, 127, 3516

Goorvitch, D. & Chackerian, Jr., C. 1994a, ApJS, 91, 483

Goorvitch, D. & Chackerian, Jr., C. 1994b, ApJS, 91, 483

Goorvitch, D. & Chackerian, Jr., C. 1994c, ApJS, 92, 311

Goorvitch, D. & Chackerian, Jr., C. 1994d, ApJS, 92, 311

Gould, A., Bahcall, J. N., & Flynn, C. 1996, ApJ, 465, 759

Green, P. J. & Margon, B. 1994, ApJ, 423, 723

Grevesse, N., Asplund, M., & Sauval, A. J. 2007, Space Sci. Rev., 130, 105

Grevesse, N., Noels, A., & Sauval, A. J. 1993, A&A, 271, 587

Gustafsson, B. 1989, ARA&A, 27, 701

Gustafsson, B., Bell, R. A., Eriksson, K., & Nordlund, A. 1975, A&A, 42, 407

Gustafsson, B., Edvardsson, B., Eriksson, K., et al. 2008, A&A, 486, 951

Gustafsson, B. & Jorgensen, U. G. 1994, A&A Rev., 6, 19

Hammersley, P. L., Jourdain de Muizon, M., Kessler, M. F., et al. 1998, A&AS, 128, 207

Harrison, T. E., Coughlin, J. L., Ule, N. M., & López-Morales, M. 2012, AJ, 143, 4

Hauschildt, P. H., Allard, F., & Baron, E. 1999, ApJ, 512, 377

Hauschildt, P. H., Baron, E., & Allard, F. 1997, ApJ, 483, 390

Hawley, S. L., Covey, K. R., Knapp, G. R., et al. 2002, AJ, 123, 3409

Hawley, S. L., Gizis, J. E., & Reid, I. N. 1996, AJ, 112, 2799

Helling, C., Ackerman, A., Allard, F., et al. 2008a, MNRAS, 391, 1854

Helling, C., Dehn, M., Woitke, P., & Hauschildt, P. H. 2008b, ApJ, 675, L105

Henry, T. J. 1998, in Astronomical Society of the Pacific Conference Series, Vol. 134, Brown Dwarfs and Extrasolar Planets, ed. R. Rebolo, E. L. Martin, & M. R. Zapatero Osorio, 28–+

Henry, T. J., Franz, O. G., Wasserman, L. H., et al. 1999, ApJ, 512, 864

Henry, T. J., Kirkpatrick, J. D., & Simons, D. A. 1994, AJ, 108, 1437

Henyey, L., Vardya, M. S., & Bodenheimer, P. 1965, ApJ, 142, 841

Irwin, J. M., Quinn, S. N., Berta, Z. K., et al. 2011, ApJ, 742, 123

Jao, W.-C., Henry, T. J., Beaulieu, T. D., & Subasavage, J. P. 2008, AJ, 136, 840

Johnas, C. M. S., Hauschildt, P. H., Schweitzer, A., et al. 2007, A&A, 475, 1039

Johnson, J. A. & Apps, K. 2009, ApJ, 699, 933

Johnson, J. A., Clanton, C., Howard, A. W., et al. 2011, ApJS, 197, 26

Jones, H. R. A., Longmore, A. J., Jameson, R. F., & Mountain, C. M. 1994, MNRAS, 267, 413

Jorgensen, U. G. 1994a, A&A, 284, 179

Jorgensen, U. G. 1994b, A&A, 284, 179

Kandel, R. 1967a, Annales d'Astrophysique, 30, 999

Kandel, R. 1967b, Annales d'Astrophysique, 30, 439

Keenan, P. C. & Schroeder, L. W. 1952, ApJ, 115, 82

Kerber, L. O., Javiel, S. C., & Santiago, B. X. 2001, A&A, 365, 424

Kirkpatrick, J. D., Henry, T. J., & Liebert, J. 1993a, ApJ, 406, 701

Kirkpatrick, J. D., Henry, T. J., & McCarthy, Jr., D. W. 1991, ApJS, 77, 417

Kirkpatrick, J. D., Henry, T. J., & Simons, D. A. 1995, AJ, 109, 797

Kirkpatrick, J. D., Kelly, D. M., Rieke, G. H., et al. 1993b, ApJ, 402, 643

Kirkpatrick, J. D., Reid, I. N., Liebert, J., et al. 1999, ApJ, 519, 802

Koen, C. & Eyer, L. 2002, MNRAS, 331, 45

Koen, C., Kilkenny, D., van Wyk, F., & Marang, F. 2010, MNRAS, 403, 1949

Köhler, R., Ratzka, T., & Leinert, C. 2012, A&A, 541, A29

Kraus, A. L., Tucker, R. A., Thompson, M. I., Craine, E. R., & Hillenbrand, L. A. 2011, ApJ, 728, 48

Kui, R. 1991, PhD thesis, PhD. thesis. Natl. Univ. Aust. , (1991)

Kupka, F. & Ryabchikova, T. A. 1999, Publications de l'Observatoire Astronomique de Beograd, 65, 223

Kurucz, R. L. 1970, SAO Special Report, 309

Kurucz, R. L. 1973, PhD thesis, HARVARD UNIVERSITY.

Laughlin, G., Bodenheimer, P., & Adams, F. C. 1997, ApJ, 482, 420

Leggett, S. K., Allard, F., Berriman, G., Dahn, C. C., & Hauschildt, P. H. 1996, ApJS, 104, 117

Leggett, S. K., Allard, F., Dahn, C., et al. 2000, ApJ, 535, 965

Leggett, S. K., Allard, F., & Hauschildt, P. H. 1998, ApJ, 509, 836

Leggett, S. K., Harris, H. C., & Dahn, C. C. 1994, AJ, 108, 944

Leggett, S. K. & Hawkins, M. R. S. 1988, MNRAS, 234, 1065

Leinert, C., Allard, F., Richichi, A., & Hauschildt, P. H. 2000, A&A, 353, 691

Leinert, C., Jahreiß, H., Woitas, J., et al. 2001, A&A, 367, 183

Leinert, C., Weitzel, N., Richichi, A., Eckart, A., & Tacconi-Garman, L. E. 1994, A&A, 291, L47

Leinert, C., Woitas, J., Allard, F., Richichi, A., & Jahreiss, H. 1998, in Astronomical Society of the Pacific Conference Series, Vol. 134, Brown Dwarfs and Extrasolar Planets, ed. R. Rebolo, E. L. Martin, & M. R. Zapatero Osorio, 203

Lemke, D., Klaas, U., Abolins, J., et al. 1996, A&A, 315, L64

Lenzen, R., Hartung, M., Brandner, W., et al. 2003, in Society of Photo-Optical Instrumentation Engineers (SPIE) Conference Series, Vol. 4841, Society of Photo-Optical Instrumentation Engineers (SPIE) Conference Series, ed. M. Iye & A. F. M. Moorwood, 944–952

Lépine, S. 2009, in American Institute of Physics Conference Series, Vol. 1094, 15th Cambridge Workshop on Cool Stars, Stellar Systems, and the Sun, ed. E. Stempels, 545–548

Lépine, S., Hilton, E. J., Mann, A. W., et al. 2013, AJ, 145, 102

Lépine, S., Rich, R. M., & Shara, M. M. 2003a, AJ, 125, 1598

Lépine, S., Rich, R. M., & Shara, M. M. 2007, ApJ, 669, 1235

Lépine, S., Shara, M. M., & Rich, R. M. 2003b, AJ, 126, 921

Lodders, K. & Fegley, Jr., B. 2006, Chemistry of Low Mass Substellar Objects, ed. Mason, J. W. (Springer Verlag), 1–+

Lodieu, N., Scholz, R.-D., McCaughrean, M. J., et al. 2005, A&A, 440, 1061

Ludwig, B. C. 1971, , 459, 1057

Ludwig, H.-G., Allard, F., & Hauschildt, P. H. 2002, A&A, 395, 99

Ludwig, H.-G., Allard, F., & Hauschildt, P. H. 2006, A&A, 459, 599

Ludwig, H.-G., Freytag, B., & Steffen, M. 1999, A&A, 346, 111

Luhman, K. L. 1999, ApJ, 525, 466

Luhman, K. L., Briceño, C., Stauffer, J. R., et al. 2003, ApJ, 590, 348

Luhman, K. L., Liebert, J., & Rieke, G. H. 1997, ApJ, 489, L165

Luhman, K. L., Rieke, G. H., Briceno, C., Liebert, J., & Hartmann, L. 1998, in Astronomical Society of the Pacific Conference Series, Vol. 154, Cool Stars, Stellar Systems, and the Sun, ed. R. A. Donahue & J. A. Bookbinder, 1887

Luyten, W. J. 1968, MNRAS, 139, 221

Maiolino, R., Rieke, G. H., & Rieke, M. J. 1996, AJ, 111, 537

Mallik, S. V. 1997, A&AS, 124, 359

Marcy, G. W. & Chen, G. H. 1992, ApJ, 390, 550

Marilli, E., Catalano, S., & Trigilio, C. 1986, A&A, 167, 297

Marley, M. S., Saumon, D., Guillot, T., et al. 1996, Science, 272, 1919

Martín, E. L., Delfosse, X., Basri, G., et al. 1999, AJ, 118, 2466

Martín, E. L., Phan-Bao, N., Bessell, M., et al. 2010, A&A, 517, A53

Martin, E. L., Rebolo, R., & Zapatero-Osorio, M. R. 1996, ApJ, 469, 706

Mera, D., Chabrier, G., & Baraffe, I. 1996, ApJ, 459, L87+

Mould, J. R. 1975, A&A, 38, 283

Mould, J. R. 1976a, A&A, 48, 443

Mould, J. R. 1976b, ApJ, 207, 535

Mould, J. R. 1978, ApJ, 226, 923

Mould, J. R. & Hyland, A. R. 1976, ApJ, 208, 399

Neuhäuser, R., Schmidt, T. O. B., Seifahrt, A., et al. 2009, in American Institute of Physics Conference Series, Vol. 1094, 15th Cambridge Workshop on Cool Stars, Stellar Systems, and the Sun, ed. E. Stempels, 844–847

Neves, V., Bonfils, X., Santos, N. C., et al. 2012, A&A, 538, A25

Noyes, R. W., Hartmann, L. W., Baliunas, S. L., Duncan, D. K., & Vaughan, A. H. 1984, ApJ, 279, 763

Önehag, A., Heiter, U., Gustafsson, B., et al. 2012, A&A, 542, A33

Pettersen, B. R. 1980, A&A, 82, 53

Phan-Bao, N., Martín, E. L., Reylé, C., Forveille, T., & Lim, J. 2005, A&A, 439, L19

Plez, B. 1992, A&AS, 94, 527

Plez, B. 1998, A&A, 337, 495

Rajpurohit, A. S., Reylé, C., Allard, F., et al. 2013, A&A, 556, A15

Rajpurohit, A. S., Reylé, C., Schultheis, M., et al. 2012a, in SF2A-2012: Proceedings of the Annual meeting of the French Society of Astronomy and Astrophysics, ed. S. Boissier, P. de Laverny, N. Nardetto, R. Samadi, D. Valls-Gabaud, & H. Wozniak, 383–388

Rajpurohit, A. S., Reylé, C., Schultheis, M., et al. 2012b, A&A, 545, A85

Reid, I. N., Cruz, K. L., Allen, P., et al. 2004, AJ, 128, 463

Reid, I. N., Cruz, K. L., & Allen, P. R. 2007, AJ, 133, 2825

Reid, I. N. & Gizis, J. E. 1997, AJ, 114, 1992

Reid, I. N. & Gizis, J. E. 2005, PASP, 117, 676

Reid, I. N., Hawley, S. L., & Gizis, J. E. 1995, AJ, 110, 1838

Reid, N. 1993, MNRAS, 265, 785

Reid, N. & Gilmore, G. 1984, MNRAS, 206, 19

Reiners, A. 2005, Astronomische Nachrichten, 326, 930

Reiners, A., Homeier, D., Hauschildt, P. H., & Allard, F. 2007a, A&A, 473, 245

Reiners, A., Seifahrt, A., Käufl, H. U., Siebenmorgen, R., & Smette, A. 2007b, A&A, 471, L5

Renzini, A., Bragaglia, A., Ferraro, F. R., et al. 1996, ApJ, 465, L23+

Reylé, C. & Robin, A. C. 2004, A&A, 421, 643

Reylé, C., Robin, A. C., Scholz, R.-D., & Irwin, M. 2002, A&A, 390, 491

Reylé, C., Scholz, R.-D., Schultheis, M., Robin, A. C., & Irwin, M. 2006, MNRAS, 373, 705

Rice, E. L., Barman, T., Mclean, I. S., Prato, L., & Kirkpatrick, J. D. 2010, ApJS, 186, 63

Robberto, M. & Herbst, T. M. 1998, in Society of Photo-Optical Instrumentation Engineers (SPIE) Conference Series, Vol. 3354, Society of Photo-Optical Instrumentation Engineers (SPIE) Conference Series, ed. A. M. Fowler, 711–719

Rojas-Ayala, B., Covey, K. R., Muirhead, P. S., & Lloyd, J. P. 2010, ApJ, 720, L113

Rojas-Ayala, B., Covey, K. R., Muirhead, P. S., & Lloyd, J. P. 2012, ApJ, 748, 93

Rossow, W. B. 1978, , 36, 1

Rothman, L. S., Gordon, I. E., Barbe, A., et al. 2009, J. Quant. Spec. Radiat. Transf., 110, 533

Rousset, G., Lacombe, F., Puget, P., et al. 2003, in Society of Photo-Optical Instrumentation Engineers (SPIE) Conference Series, Vol. 4839, Society of Photo-Optical Instrumentation Engineers (SPIE) Conference Series, ed. P. L. Wizinowich & D. Bonaccini, 140–149

Ruiz, J. 1997, Earth Moon and Planets, 77, 99

Russell, H. N. 1934, ApJ, 79, 317

Schlaufman, K. C. & Laughlin, G. 2010, A&A, 519, A105

Schmidt, T. O. B., Neuhäuser, R., Seifahrt, A., et al. 2008, A&A, 491, 311

Scholz, R.-D., Irwin, M., Ibata, R., Jahreiß, H., & Malkov, O. Y. 2000, A&A, 353, 958

Scholz, R.-D., Lehmann, I., Matute, I., & Zinnecker, H. 2004, A&A, 425, 519

Seelmann, A. M., Hauschildt, P. H., & Baron, E. 2010, A&A, 522, A102

Seifahrt, A., Röll, T., Neuhäuser, R., et al. 2008, A&A, 484, 429

Sharp, C. M. & Huebner, W. F. 1990, ApJS, 72, 417

Shkolnik, E., Liu, M. C., & Reid, I. N. 2009, ApJ, 699, 649

Siess, L. & Livio, M. 1997, ApJ, 490, 785

Skory, S., Weck, P. F., Stancil, P. C., & Kirby, K. 2003a, ApJS, 148, 599

Skory, S., Weck, P. F., Stancil, P. C., & Kirby, K. 2003b, ApJS, 148, 599

Skrutskie, M. F., Cutri, R. M., Stiening, R., et al. 2006, AJ, 131, 1163

Skumanich, A. 1972, ApJ, 171, 565

Stassun, K. G., Mathieu, R. D., & Valenti, J. A. 2006, Nature, 440, 311

Tashkun, S. A., Perevalov, V. I., Teffo, J.-L., et al. 2004, Proc. SPIE, 5311, 102

Testi, L. 2009, A&A, 503, 639

Tinney, C. G., Mould, J. R., & Reid, I. N. 1993, AJ, 105, 1045

Tinney, C. G. & Reid, I. N. 1998, MNRAS, 301, 1031

Tokunaga, A. T. & Kobayashi, N. 1999, AJ, 117, 1010

Tsuji, T. 1965, PASJ, 17, 152

Tsuji, T. 1966, PASJ, 18, 127

Tsuji, T. 1973, A&A, 23, 411

Tsuji, T. 1995, in Astronomical Society of the Pacific Conference Series, Vol. 81, Laboratory and Astronomical High Resolution Spectra, ed. A. J. Sauval, R. Blomme, & N. Grevesse, 566

Tsuji, T. 2002, ApJ, 575, 264

Tsuji, T., Ohnaka, K., & Aoki, W. 1996a, A&A, 305, L1+

Tsuji, T., Ohnaka, K., & Aoki, W. 1999, ApJ, 520, L119

Tsuji, T., Ohnaka, K., Aoki, W., & Nakajima, T. 1996b, A&A, 308, L29

Unsold, A. 1968, Physik der Sternatmospharen, MIT besonder Berucksichtigung der Sonne

Valenti, J. A. & Piskunov, N. 1996, A&AS, 118, 595

Vardya, M. S. 1966, MNRAS, 134, 347

Veeder, G. J. 1974, AJ, 79, 1056

Viti, S. & Jones, H. R. A. 1999, A&A, 351, 1028

Vrba, F. J., Henden, A. A., Luginbuhl, C. B., et al. 2004, AJ, 127, 2948

Weck, P. F., Schweitzer, A., Stancil, P. C., Hauschildt, P. H., & Kirby, K. 2003, ApJ, 584, 459

Wehrse, R. 1972, A&A, 19, 453

West, A. A., Bochanski, J. J., Hawley, S. L., et al. 2006, AJ, 132, 2507

West, A. A., Hawley, S. L., Walkowicz, L. M., et al. 2004, AJ, 128, 426

West, A. A., Morgan, D. P., Bochanski, J. J., et al. 2011, AJ, 141, 97

Wing, R. F. & Rinsland, C. P. 1979, AJ, 84, 1235

Witte, S., Helling, C., Barman, T., Heidrich, N., & Hauschildt, P. H. 2011, A&A, 529, A44

Witte, S., Helling, C., & Hauschildt, P. H. 2009, A&A, 506, 1367

Woitke, P. & Helling, C. 2004, A&A, 414, 335

Woolf, V. M., Lépine, S., & Wallerstein, G. 2009, PASP, 121, 117

Woolf, V. M. & Wallerstein, G. 2005, MNRAS, 356, 963

Woolf, V. M. & Wallerstein, G. 2006, PASP, 118, 218

Woolf, V. M. & West, A. A. 2012, MNRAS, 422, 1489

York, D. G., Adelman, J., Anderson, Jr., J. E., et al. 2000, AJ, 120, 1579

Yurchenko, S. N., Barber, R. J., & Tennyson, J. 2011, MNRAS, 413, 1828

Zacharias, N., Monet, D. G., Levine, S. E., et al. 2005, VizieR Online Data Catalog, 1297, 0

Zhou, X. 1991, A&A, 248, 367